



Escola de Camins
Escola Tècnica Superior d'Enginyeria de Camins, Canals i Ports
UPC BARCELONATECH

Assessing the performance of additive manufacturing components

Treball realitzat per:

Mao Ye

Dirigit per:

Narges Dialami

Michele.Chiumenti

Màster en:

Numerical Methods in Engineering

LLeida, 05 May 2021

Department of Civil and Environmental Engineering

TREBALL FINAL DE MÀSTER

Abstract

Additive Manufacturing (AM), also called as 3D printing, is a process that creates a 3D object from a digital design and is fabricated by adding material layer upon layer. Several major AM techniques were developed since 1980s with wide range of materials. The main advantage of AM is that it can fabricate the object with complicated geometry comparing with traditional manufacturing. Due to its adaptability, AM have a wide range of applications in aerospace, automotive, biomedical, energy and other industries. However, there is not enough standards to support this new technique so far. This work will assess the performance of the additive manufacturing demonstrators. The present work focused on one of the first AM techniques, Fused Filament Fabrication (FFF). Of all the AM techniques available today, FFF is the best known and the most widely used due to its versatility and suitability for operating with a wide range of material. In this work, the material properties of the components additively manufactured by FFF are evaluated in order to analyze their mechanical performance. To accurately identify the anisotropy induced in the material properties by the manufacturing process, the objects are partitioned according to their printing pattern into three zones: the contour, the cover and the inner structure. Thus, their respective mechanical properties are determined separately. Experimentally, uniaxial tensile tests on various PC-ABS 3D dog-bone samples are performed to represent the material of the contour and the cover. However, performing such experimental tests may be challenging. A geometrical relationship between the material properties at different orientation and the raw material is found. In the computational characterization, a homogenization technique using a Representative Volume Element (RVE) is adopted for the inner structure. After identifying the material properties of the contour, the cover and the inner structure, the computational model is validated. Experimental tests on PC-ABS 3D square cross-section demonstrators under pure bending loadings are realized. Moreover, the mechanical performance of the objects in the four demonstrators are obtained based on numerical simulation applying the above. The impact of the layer deposition pattern of differently oriented pieces and process parameters on the material conduct is studied. It is shown that the material performance of different parts of the component depends on the printing orientation and parameters. The most significant parameters besides the printing orientation are the layer thickness and the pattern designs. These parameters are selected prior to printing and affect the mechanical performance of the components [47]. Therefore, performance analysis of FFF built components is an exigency from the AM users.

Furthermore, using the proposed geometrical relationship, exhaustive experimental tests can be avoided for the material characterization of the contour and the cover. The model proposed may be used as a design-for-manufacture (DFM) approach to create functional components.

Keywords

Additive Manufacturing, Fused Filament Fabrication, Representative Volume Element, Finite Element Method, Simulation

Contents

1.	Introduction.....	1
1.1.	Motivation	1
1.2.	Objectives	6
1.3.	Structure of this thesis	6
2.	State of the art.....	8
2.1.	Common Additive Manufacturing techniques	8
2.1.1.	Selective Laser Sintering (SLS)	10
2.1.2.	Multi Jet Fusion (MJF™)	12
2.2.	Fused Filament Fabrication (FFF)	13
2.2.1.	Common printing parameters	15
2.2.2.	FFF printing parameters	16
2.3.	Inner structures	18
2.3.1.	In-fill structures	19
2.3.2.	Lattice structures	21
2.4.	Mechanical behavior of parts made by FFF	21
3.	Mechanical analysis of FFF pieces.....	27
3.1.	Structure of FFF components	27
3.2.	Mechanical problem	28
3.3.	Constitutive laws	30
3.3.1.	Orthotropy	32
3.3.2.	Transverse isotropy	33
3.3.3.	Isotropy	34
3.4.	Homogenization-Representative Volume Element	35
3.4.1.	First-order homogenization	35
4.	Performance analysis of demonstrators.....	42
4.1.	Case1 Beam	42
4.1.1.	Introduction	42
4.1.2.	Methodology	44
4.1.3.	Result	45
4.1.4.	Conclusion	66
4.2.	Case2 Electric box	67
4.2.1.	Introduction	67
4.2.2.	Methodology	67
4.2.3.	Result	68
4.3.	Case3 Armrest	81
4.3.1.	Introduction	81
4.3.2.	Methodology	82
4.3.3.	Result	82
4.4.	Case4 Handle	99
4.4.1.	Introduction	99
4.4.2.	Methodology	99

4.4.3. Result	100
5. Conclusions and future work.....	115
5.1. Conclusions	115
5.2. Future work	116
5.2.1. Large deformations formulation	116
5.2.2. Orthotropic failure criteria	118
5.2.3. Selecting the best printing orientation	119
Reference.....	121

LIST OF FIGURES

Figure 1.1 FDM 3D printer [5].....	1
Figure 1.2 Part of engine with lattice structure [6] and AM application in biomedical [9]	4
Figure 1.3 The AM part used by NASA [10].....	4
Figure 2.1 Generic process of CAD to part, showing all 8 stages [14].....	10
Figure 2.2 A typical SLS machine layout [15].....	11
Figure 2.3 A typical DMLS machine layout [16]	12
Figure 2.4 MJF process [17].....	13
Figure 2.5 MJF vs FFF [19]	13
Figure 2.6 Overview of the FFF process [20].....	15
Figure 2.7 Different support material in different printing orientation [21]	17
Figure 2.8 Parameter's scheme of the contour and raster trajectories [20]	18
Figure 2.9 In-fill structure and Auxetic in-fill structure	19
Figure 2.10 Lattice structure [19].....	19
Figure 2.11 Example of In-fill patterns [23].....	20
Figure 2.12 Layers disposition depending on the printing orientation [22]	22
Figure 2.13 Formation process between two filaments [26]	23
Figure 2.14 Scheme of the compression force influence on the layer direction [22].	23
Figure 2.15 Tensile strength of specimens with various raster angel [29]	24
Figure 2.16 Compressive strength of specimens with alternate raster angles, 45°-45°, and different printing directions. [29]	25
Figure 2.17 Stress-strain curves for specimen's fill density influence comparison [30]	25
Figure 3.1 Typical three structures in FFF.....	28
Figure 3.2 The coordinate system showing axes X_1 , X_2 and X_3 . The normal stresses are σ_1 , σ_2 and σ_3 . The shear stresses are σ_{12} , σ_{23} and σ_{31} . [31].....	31
Figure 3.3 First-order computational homogenization [34].....	36
Figure 3.4 Effective Young's modulus, E_x , as function of relative density for the hexagonal cell. Results obtained with the DBC and NBC bound those calculated with the PBC [35].....	41
Figure 4.1 Different zones of a FFF component in this case.....	42
Figure 4.2 Different building orientations of a test specimen manufactured by FFF .	44
Figure 4.3 The strategy for the material characterization	46
Figure 4.4 Dog-bone specimen dimension	47
Figure 4.5 Tensile test plot (dog-bone specimens).....	48
Figure 4.6 Orientations of the dog-bone specimens	49
Figure 4.7 Obtaining Young's Modulus Parallel to the deposition of the contour material	55
Figure 4.8 Scheme of load application to obtain the Poisson's ratio of the isotropy plane for the contour material.....	55
Figure 4.9 Obtaining Young's modulus in the construction direction for the cover	

material	56
Figure 4.10 Obtaining isotropic Young's Modulus for the cover material	57
Figure 4.11 Diagram for obtaining the parameters from the tests (contour material)	57
Figure 4.12 Diagram for obtaining the parameters from the tests (cover material)	58
Figure 4.13 Geometry of square cross-section demonstrator (dimensions in mm)	60
Figure 4.14 Samples with square cross-section printed at different orientations: H and V	61
Figure 4.15 Cross-section of the V sample with 10%, 20% and 50% in-fill density (left to right)	61
Figure 4.16 Experimental setting and the load position (square cross-section demonstrator)	62
Figure 4.17 Flexural test plot (square cross-section samples)	62
Figure 4.18 Simulated deformation of the square cross-section sample	63
Figure 4.19 Homogenization strategy and PBC on the boundary of RVE	63
Figure 4.20 Force [N] vs. displacement [mm] curves comparing the simulation results with the experimental measurements	66
Figure 4.21 The 50% fabricated electric box with PC-ABS	67
Figure 4.22 Properties of PC-ABS distribution	72
Figure 4.23 Full geometry	73
Figure 4.24 Cover geometry	73
Figure 4.25 Box body geometry	74
Figure 4.26 Loads on Cases	75
Figure 4.27 Constrains	76
Figure 4.28 Full Mesh	76
Figure 4.29 Von-mises stress in 6 cases from No.1-6	78
Figure 4.30 Displacement in 6 cases from No.1-6	80
Figure 4.31 Armrest in 3D image	82
Figure 4.32 Armrest printed by FFF	82
Figure 4.33 Full geometry	86
Figure 4.34 Octet RVE geometry	87
Figure 4.35 Loading on the three points	87
Figure 4.36 Loads on Octet RVE geometry	88
Figure 4.37 Constrains	89
Figure 4.38 Full Mesh	89
Figure 4.39 Mesh on critical part	90
Figure 4.40 Octet RVE Mesh	90
Figure 4.41 Von-mises stresses in the 5 cases in order with the material of ABS	92
Figure 4.42 Displacements in the 5 cases in order with the material of ABS	94
Figure 4.43 Von-mises stresses in the 5 cases in order with the material of ULTEM TM 9085	96
Figure 4.44 Displacements in the 5 cases in order with the material of ULTEM TM 9085	98
Figure 4.45 Seat handle in Dubai Metro	99
Figure 4.46 Original geometry	101

Figure 4.47 Loads on the original geometry, case1 (1st), case2 (2nd)	102
Figure 4.48 Constrains on the original geometry.....	103
Figure 4.49 Mesh on the original model.....	103
Figure 4.50 Von-mises stress in original model, case1 (1st), case2 (2nd).....	104
Figure 4.51 MaxVon-mises stress in original model, case1 (1st), case2 (2nd)	105
Figure 4.52 Displacement in X direction in original model, case1 (1st), case2 (2nd)	105
Figure 4.53 The parts to be optimized	107
Figure 4.54 Optimized geometry.....	108
Figure 4.55 Loads on the optimized geometry, case1 (1st), case2(2nd).....	109
Figure 4.56 Constrains on the optimized geometry.....	110
Figure 4.57 Mesh on the optimized model	111
Figure 4.58 Von-mises stress in optimized model, case1 (1st), case2 (2nd)	112
Figure 4.59 Max Von-mises stress in optimized model, case1 (1st), case2 (2nd) ...	113
Figure 4.60 Displacement in X direction in optimized model, case1 (1st), case2(2nd)	114
Figure 5.1 Micro element deformation scheme	118

LIST OF TABLES

Table 1.1 Working principle of AM processes, table 1 of [6]	2
Table 1.2 Glossary of table 1.1 [6]	2
Table 2.1 Parameters configuration of the contour and raster trajectories	17
Table 4.1 Specimen Dimensions for Thickness, T, mm (in.) ^A	48
Table 4.2 P samples (contour).....	50
Table 4.3 I samples (contour)	52
Table 4.4 Material properties of contour and cover of PC-ABS 3D in the model	58
Table 4.5 In-fill material properties (square cross-section sample).....	64
Table 4.6 Mechanical response of the square cross-section sample and the relative error according to each orientation and printing parameters.....	65
Table 4.7 Properties of Top and Bottom, Printing direction in Z	68
Table 4.8 Properties of Irregular contour.....	70
Table 4.9 Properties of wall in YZ plane, filament direction in Y	70
Table 4.10 Properties of wall in XZ plane, filament direction in X.....	71
Table 4.11 Loads direction on the six cases	74
Table 4.12 Summary of results.....	81
Table 4.13 Properties of ABS in the model	83
Table 4.14 Basic Properties of ULTEM9085 in the model	83
Table 4.15 Properties of Octet RVE lattice with the material ABS.....	83
Table 4.16 Properties of Octet RVE lattice with the material ULTEM TM 9085.....	83
Table 4.17 Properties of Contour with material ABS	85
Table 4.18 Properties of Contour with material ULTEM TM 9085	85
Table 4.19 Loads combination on the five cases.....	88
Table 4.20 Summary of maximum stresses in the places that are not singular and	

<i>maximum displacements</i>	99
<i>Table 4.21 Aluminum Property</i>	100
<i>Table 4.22 Loading cases in the original model</i>	102
<i>Table 4.23 Summary of Maximum stress in original model</i>	106
<i>Table 4.24 Loading cases in optimized model</i>	109
<i>Table 4.25 Summary of Maximum stress in optimized model</i>	114

1. Introduction

1.1. Motivation

Additive manufacturing (AM), also mentioned as 3D printing, fabricates a three-dimensional object from a computer aided design (CAD) model or a digital 3D model [1]. It could refer to a variety of process in which material is deposited, joined or solidified. Computer controlling is used to create a three-dimensional object [2], with material being added together and layer by layer. AM technology began in the 1950s. The general concept of 3D printing was first described by Raymond F. Jones. Early additive manufacturing equipment and materials were developed in the 1980s [3]. In the 1990s, the automated techniques that added metal were beginning to challenge the non-additive assumption. Later, people call it as additive manufacturing. When the patent of Fused Deposition Modeling (FDM) printing process expired in 2009, prices for FDM printers dropped from over \$10,000 to less than \$1,000, and a new crop of consumer-friendly 3D printer manufacturers, like MakerBot and Ultimaker, paved the way for accessible 3D printing [4]. Nowadays, AM technology is applied in different industrial area and study field. The huge advantage comparing with traditional manufacturing is the large number of possibilities and variety for complicated structure or geometry.



Figure 1.1 FDM 3D printer [5]

As 70 years goes, AM processes have been developed. These processes mainly classified in four types: liquid, filament/paste, powder and solid sheet. The working principle of AM process with the different states of material are summarized in Table 1.1 [6].

State of starting material	Process	Material preparation	Layer creation technique	Phase change	Typical materials	Applications
Liquid	SLA	Liquid resin in a vat	Laser scanning/light projection	Photopolymerization	UV curable resin, ceramic suspension	Prototypes, casting patterns, soft tooling
	MJM	Liquid polymer in jet	Ink-jet printing	Cooling & photopolymerization	UV curable acrylic plastic, wax	Prototypes, casting patterns
	RFP	Liquid droplet in nozzle	On-demand droplet deposition	Solidification by freezing	Water	Prototypes, casting patterns
Filament/Paste	FDM	Filament melted in nozzle	Continuous extrusion and deposition	Solidification by cooling	Thermoplastics, waxes	Prototypes, casting patterns
	Robocasting	Paste in nozzle	Continuous extrusion	–	Ceramic paste	Functional parts
	FEF	Paste in nozzle	Continuous extrusion	Solidification by freezing	Ceramic paste	Functional parts
Powder	SLS	Powder in bed	Laser scanning	Partial melting	Thermoplastics, waxes, metal powder, ceramic powder	Prototypes, casting patterns, metal and ceramic preforms (to be sintered and infiltrated)
	SLM	Powder in bed	Laser scanning	Full melting	Metal	Tooling, functional parts
	EBM	Powder in bed	Electron beam scanning	Full melting	Metal	Tooling, functional parts
	LMD	Powder injection through nozzle	On-demand powder injection and melted by laser	Full melting	Metal	Tooling, metal part repair, functional parts
	3DP	Powder in bed	Drop-on-demand binder printing	–	Polymer, Metal, ceramic, other powders	Prototypes, casting shells, tooling
Solid sheet	LOM	Laser cutting	Feeding and binding of sheets with adhesives	–	Paper, plastic, metal	Prototypes, casting models

Table 1.1 Working principle of AM processes, table 1 of [6]

SLA	Stereolithography
UV	Ultraviolet
MJM	Multi-Jet Modeling (
RFP	Rapid Freeze Prototyping
FDM	Fused Deposition Modeling
FEF	Freeze-form Extrusion Fabrication
SLS	Selective Laser Sintering
SLM	Selective Laser Melting
EBM	Electron Beam Melting
LMD	Laser Metal Deposition
3DP	Three-Dimensional Printing
LOM	Laminated Object Manufacturing

Table 1.2 Glossary of table 1.1 [6]

The AM techniques use large range of materials. Materials in the forms of filaments, wire, powder, paste, sheets and inks can be used for 3D printing. Polymers play the initial role of the material of 3D printing. Particularly, thermoplastic polymers such as acrylonitrile-butadiene-styrene (ABS), polyamide (PA), polycarbonate (PC) and polylactic acid (PLA), and thermosetting powders such as polystyrene, polyamides and photopolymer resins are the most common types of polymers in 3D printing field [7].

AM processes present great advantages in comparison with traditional techniques. Five key benefits of AM over traditional manufacturing are Cost, Speed, Quality, Innovation/Transformation, and Impact [8].

Automotive and aerospace industry use AM technologies to create lightweight parts with complex geometries. In the Figure 1.2, Engine part with lattice structure fabricated by EBM using Ti6A14V to reduce engine weight while enhance stiffness. In biomedical field, AM technologies bring good news to patients, such as: surgical guides, models of the surgery area or implants and prostheses for patients. Recently, NASA is using selective laser melting to enable faster and cheaper component development. [10].

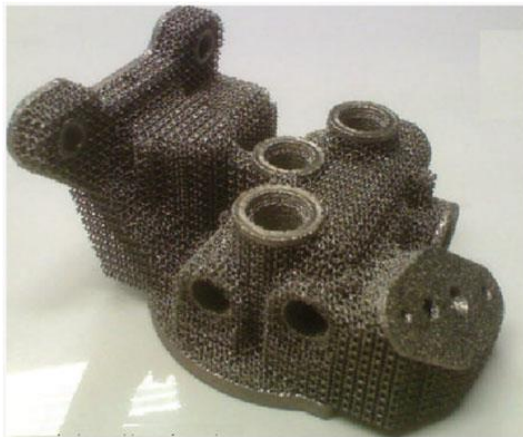


Figure 1.2 Part of engine with lattice structure [6] and AM application in biomedical [9]

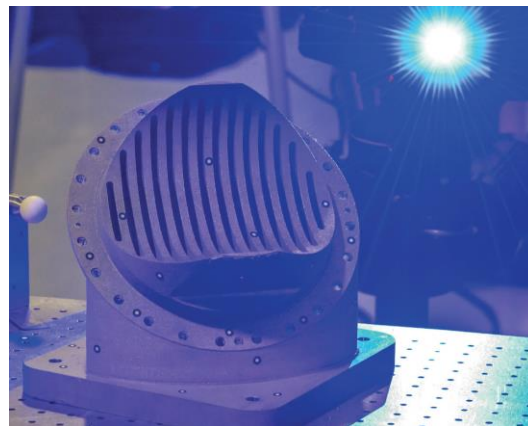


Figure 1.3 The AM part used by NASA [10]

Although the AM technologies develop fast present, there are several limitations for the development. First, there are not enough standards for the AM technologies. This problem is mainly attribute to that this cutting-edge technology is still in the stage of exploration and research. Comparing with traditional technology, AM faces some mandatory standard or specification limit in industrial. Second, not all the common material used in traditional manufacturing can be handled with AM [11]. Last but not the least, the influence of the fabrication parameters over the mechanical properties and the surface finish quality is still unknown. These limitations imply serious difficulties for using AM.

Nowadays, the mechanical behavior of AM, especially the anisotropic behavior needs to be characterized [12,13]. As the best-known AM techniques, FFF perform anisotropic behavior too. It is the results of layer-to-layer and filament-to-filament adhesions in addition to the printing patterns [49].

FFF is based on the extrusion of the printing material through a nozzle to reproduce a 3D CAD model. The deposition process is carried out by melting the filaments of a certain thermoplastic material. The extruded material is deposited layer by layer on a printing table. Simultaneous movements of the nozzle and the printing table allow the deposition in 3D, thus enabling the system to manufacture complicated 3D geometries. Considering the printing pattern, a FFF structure is characterized by three zones: the contour, that is made of aligned filaments, the inner structure, that is in-fill or lattice type, and the top and bottom covers, that are made of filaments with full density (100%) crossed pattern and 45 ° raster angle. In the inner part, the in-fill is the standard structure with density defined through the raster to raster air gap, while the lattice structure is characterized by periodically repeated unit cells. These types of inner structures are for reducing the amount of material, cost and time of production which make the FFF technique advantageous over the rest of AM technologies [50].

Even though various experimental investigations revealed the effect of the printing patterns on the properties of the printed parts, there are only a few works dealing with the analytical and computational assessment of the mechanical performance of FFF components. The existing works use a single solid model for the characterization of the material. However, the structural response of contour, cover and inner structures is different according to the manufacturing pattern and the in-fill density. The contour is stiffer along the axis of the printing plane parallel to the filaments. The cover behaves isotropically on the printing plane due to the symmetry of the pattern.

In this work, a novel methodology for the analysis of the mechanical performance of FFF built components that takes into account the different mechanical properties of the contour, the cover and the inner structure is developed. Material properties of each part is identified experimentally and computationally

1.2. Objectives

The main objective of this thesis is to access the mechanical performance of additive manufacturing components. All these components are made with FFF. According to tensile tests performed of AM specimens, a linear relationship between stress and strain is found, particularly in the small strain region. Therefore, the goal is to build a constitutive model capable to predict the response of AM components. The main objective can be divided in several specific objectives:

- Determine the mechanical properties from the experimental data to build a suitable constitutive model.
- Define a mechanical constitutive model to deal with the in-fill or lattice structures of AM pieces to simplify the computational simulations.
- Define a mechanical constitutive model to characterize the mechanical performance of components made with FFF.
- Validate the computational models comparing with experimental test data
- Analyze the mechanical performance of the real AM components.
- Analyze the mechanical performance of the components and optimize the printing procedure according to the result obtained.

1.3. Structure of this thesis

This thesis is structured as following.

Section 1: Introduction

This section describes the main concept of Additive Manufacturing.

Section 2: State of the art

This section describes the methodology for analysis of FFF components.

Section 3: Mechanical analysis of AM components

In this section, the strategy of modelling a FFF component is explained. Then, the anisotropic constitutive model and the computational homogenization technique are described.

Section 4: Performance analysis of demonstrators

This section analyzes the real case demonstrators with the methodology developed in the thesis.

Section 5: Conclusions and future work

In this section, the conclusions of this thesis and proposals for future investigations are given.

2. State of the art

This chapter mainly describes the cutting edge of AM techniques and what others have done.

2.1. Common Additive Manufacturing techniques

Additive Manufacturing is a process that creates 3D objects from a model layer by layer. Generally, AM technologies create an object following the same steps as the following [14].

1) Step 1: CAD

All AM parts must start from a software model that fully describe the external geometry. This work is finished by Computed Aided Design (CAD).

2) Step 2: Conversion to STL

Nearly every AM machine accepts the stereolithography (STL) file format. An STL file describes a raw, unstructured triangulated surface by the unit normal and vertices (ordered by the right-hand rule) of the triangles using a three-dimensional Cartesian coordinate system. Meanwhile, nearly every CAD system can output such a file format. This file describes the external closed surfaces of the original CAD model and forms the basis for calculation of the slices.

3) Step 3: Transfer to AM Machine and STL File Operation

The STL file describing the part must be transferred to the AM machine. Here, there are some operations of the file to correct the size, position and orientation for building.

4) Step 5: Machine Setup

The AM machine must be properly set up prior to the build process. These settings mainly relate to the build parameters like the material constraints, energy source, layer thickness and timings.

5) Step 5: Build

The AM object is manufactured automatically by machine. What people focus are keeping the machine running normally.

6) Step 6: Removal

To remove the finished object from AM machine, safety inter lock must be considered. Otherwise, the high temperature of the finished AM object may cause security issues.

7) Step 7: Postprocessing

Once removed from the machine, parts require a postprocessing to clean and remove the support feature.

8) Step 8: Application

After some treatments like surface texture, surface finish, painting and assembly, the object can be ready for using.

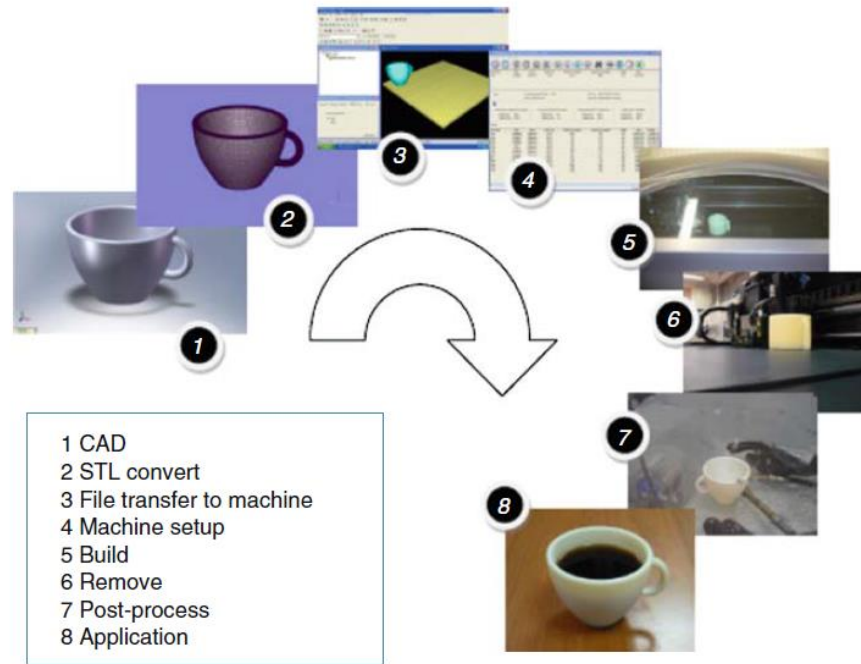


Figure 2.1 Generic process of CAD to part, showing all 8 stages [14]

2.1.1. Selective Laser Sintering (SLS)

Selective Laser Sintering (SLS) is a powder based AM process. The laser of SLS printer selectively fuses powdered material by scanning cross-section on the surface of a powder bed. The powder bed is heated to its melting point before the laser work. Cross-section are generated from the CAD file. When one layer cross-section is scanned, the build platform descends one layer thickness. Then a new layer of powder is distributed on the top of the finished layer. Finally, the object could be printed layer by layer according this process.

Usually, the SLS printer consists of a laser, a mirror scanner, a build platform, a feed container where the powder is hold and a roll that distribute the new layer of powder [15].

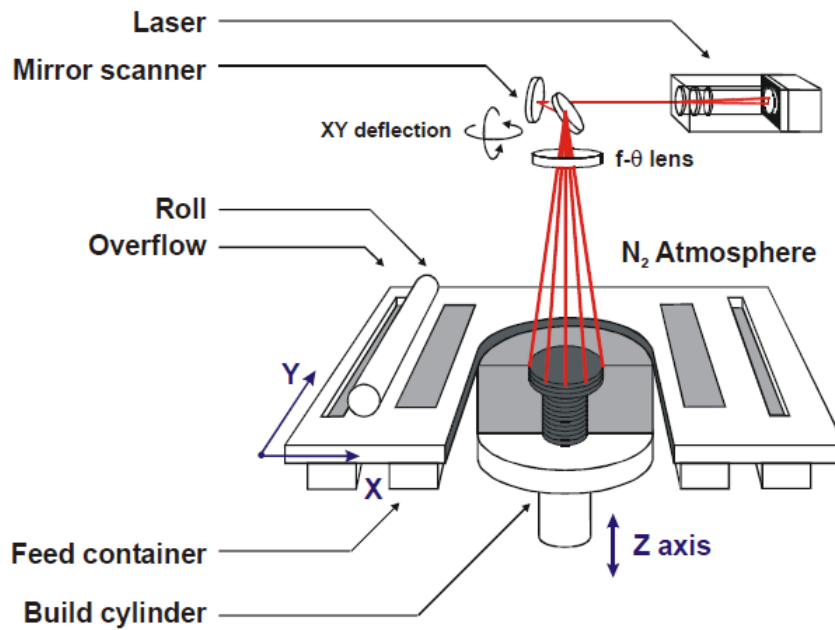


Figure 2.2 A typical SLS machine layout [15]

Polymers are the major materials used in SLS, such as polyamides, polystyrenes and polycarbonates. Meanwhile, ceramics, glass and metals are able to be processed with SLS as well. However, metal printing is more often used the Selective Laser Melting (SLM) or Direct Metal Laser Sintering (DMLS) nowadays. Generally, SLM and DMLS are quite similar. Specially, SLM offers the capability of melting the metal powder completely. That means SLM can creates homogeneous parts.

Selective laser techniques (SLS, SLM, and DMLS) present several advantages. The 1st one is that material support is not necessary. The 2nd but not the least is that the unused powder in the post-process can be reused. In addition, complicated geometries can be printed without trapping powder inside the object. On the other hand, they have some deflections. The object printed have porous surfaces that requires to be sealed in the post-process. The expensive cost limited these techniques' application, specially DMLS. Therefore, they are more often used in the field of aerospace and biomedical.

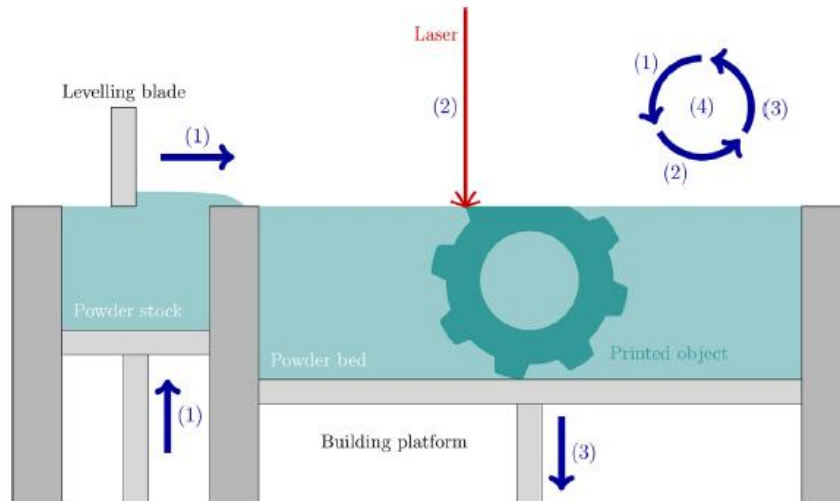


Figure 2.3 A typical DMLS machine layout [16]

2.1.2. Multi Jet Fusion (MJF™)

Multi Jet Fusion (MJF) is a special powder based AM technology developed by the company Hewlett-Packard (HP), whose process are different from other powder based techniques introduced before in section 2.1.1.

- a) The build material is recoated on the surface layer as shown in Fig.2.4 (a)
- b) The printing process applies a fusing agent selectively to the place where 3D project to be. Fig.2.4 (b)
- c) The printing process applies a detailing agent where the fusing action need to be controlled. Fig.2.4 (c)
- d) Radiation energy is applied on the entire surface as shown in Fig.2.4. (d).
- e) Last, the area for 3D object is fused as shown in Fig.2.4 (e).

The process is repeated layer by layer until the full 3D object is printed. The remains of powder are retired for future printings. Most common materials used in MJF are polymer, specifically polyamides.

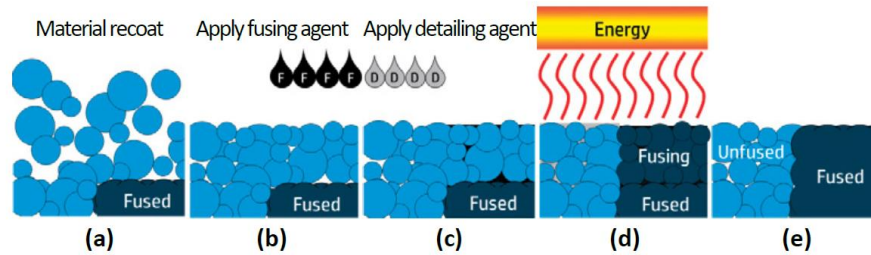


Figure 2.4 MJF process [17]

Obviously, the AM technique developed by HP company presents advantages compared to other AM technologies. Printing time is much lower than FFF. Furthermore, the pieces made by MJF have great strength and present better isotropic behavior than the one produced by FFF. Therefore, the structural behavior does not depend on the building orientation, while the flexural strength is different in different building orientation [18]. The visual difference of the printing quality can be seen in Fig.2.4. Finally, MJF samples have a better surface finish and smooth layers that could be colored or impregnated.

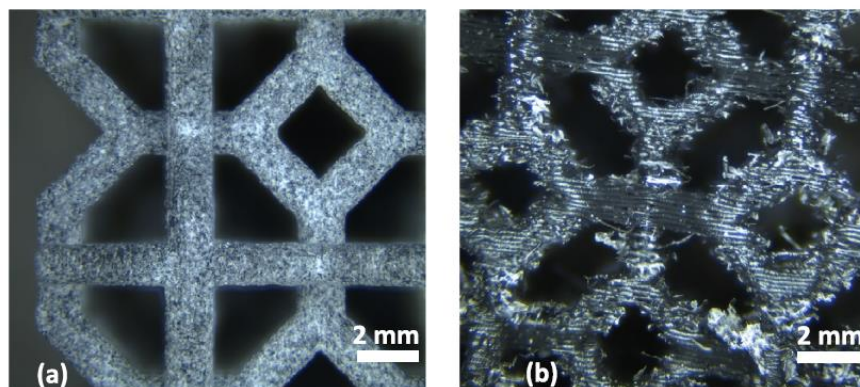


Figure 2.5 MJF vs FFF [19]

2.2. Fused Filament Fabrication (FFF)

Fused Filament Fabrication (FFF) is also known as Fused Deposition Modelling™ (FDM), which is a trademark of Stratasys company. This thesis and TFM are mainly based on the object made by FFF.

FFF printer consists in two types nozzles, one foundation sheet and the build platform. One nozzle is for building material. It moves in XY plane and deposits the material on the fabrication platform. Another nozzle working for supporting material. This support is used to support the object during the fabrication and prevent from collapse. The support material is removed manually in the post-processing. When the geometries to be produced are more complicated, water-soluble support material usually be used. The following figure shows an overview of a FFF printer.

Plastic is the most common material used in FFF technique for 3D printing. The usual thermoplastic polymers are: Acrylonitrile Butadiene Styrene (ABS), Polycarbonate (PC), Polycarbonate-Acrylonitrile-Butadiene-Styrene (PC-ABS), Polylactic Acid (PLA) and High-density polyethylene (HDPE). The polymers are coiled in spools for FFF printing. The polymer filament in the nozzle comes from the spool and is melted and extruded over the building platform. When a layer is finished, the platform descends or the nozzles ascend. Then, a new layer is printed. This process is repeated until the object is completed.

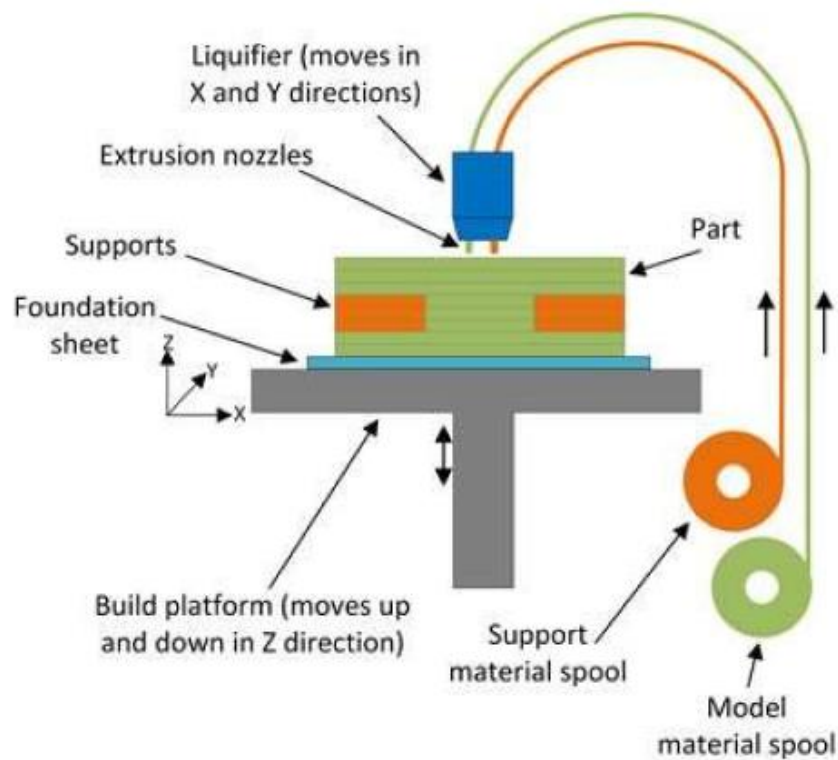


Figure 2.6 Overview of the FFF process [20]

2.2.1. Common printing parameters

The main common parameters to characterize components fabricated by AM techniques are: the printing orientation, the thickness of layer and the deposition (scanning) sequence. The most important printing parameter is the building orientation, sometimes it is called as printing orientation or printing direction, etc. in other authors' thesis. The printing orientation of an AM piece affects its mechanical behavior directly [21]. In chapter 4 of this paper, this concept will explain in detail.

The thickness of layer is another important printing parameter. It would affect the mechanical behavior, surfaces finish quality and the cost.

- In SLS, the thickness is determined by the laser power and the size of the powder. Usually, it oscillates between 0.020 mm and 0.150 mm while 0.05mm is the common value used.

- In MJF, the thickness is similar as the one in SLS. It often oscillates between 0.07mm and 0.1mm.
- In FFF, the thickness is a little different than the previous ones. Usually, it depends on the diameter of nozzle and the filament size. The value oscillates between 0.15mm and 1.0mm.

Another representative common parameter among AM technologies is the deposition sequence which is called as scanning sequence as well. This parameter determines the path that the laser or the nozzle follows to create each layer. This allows for selecting the pattern and grade of the in-fill. Any type of configuration has consequences in terms of structural behavior for the object, surface finish, weight and cost.

2.2.2. FFF printing parameters

Some printing parameters of FFF are different from the ones in SLS or MJF techniques. First, the support of the FFF is different than the one in SLS and MJF which is supported by loose powder. FFF need support material for printing complicated geometries. Due to this character, selecting the most suitable printing orientation becomes vital in FFF. Different orientation depends a different amount of supporting material to be used. (Fig. 2.7). Besides, the building orientation is one of the main causes of anisotropy in the mechanical behavior of the 3D object [22].



Figure 2.7 Different support material in different printing orientation [21]

Second, the trajectory of the nozzles is also critical in FFF since it determines how to print and build every layer. Two types of trajectories can be distinguished for each layer: the contour and the raster. The contour is the trajectory that defines the exterior surface of the 3D object while the raster is the trajectory which fill the inner section and delimit by the contour. The following table (Table 2.1) expound the different parameters configuration of the two trajectories.

Configuration	Contour	Raster
Width	The diameter of the extruded filament.	The diameter of the extruded filament.
Number	The number of contours that defines the exterior surfaces.	
Angle		The angle of the trajectory measured from the printer's X axis.
Air gap	Distance between two filament contours.	Distance between two filament rasters, or raster to contour distance

Table 2.1 Parameters configuration of the contour and raster trajectories

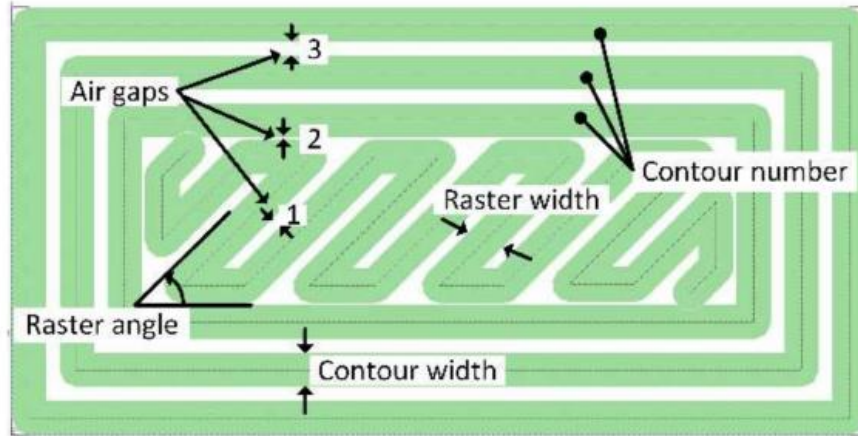


Figure 2.8 Parameter's scheme of the contour and raster trajectories [20]

Another parameter to be accounted for is the diameter of the nozzle. This parameter defines the height of the layer besides the width of the contour and the raster. The layer height used to be half of the diameter of the nozzle. In addition, the nozzle speed also controls the layer height, that is around 23.5 mm/s usually.

Last but not the least, the in-fill percentage play an important role in the structure behavior. It can vary from 0% to 100%. A 0% in-fill means there is no raster in the object which is only built by contours. On the other hand, a 100% in-fill means there is no gaps in the inner of contour. All the inner material are filled with raster. Obviously, the density of the in-fill depends on the gaps between two rasters.

2.3. Inner structures

Comparing with the traditional manufacturing processes, the AM technologies can print complicated geometries. This advantage can make lighter objects by the intricate in-fill and lattice and save material. There are two types of inner structures that be defined: the infill structure in Figure 2.9 and the lattice structure in Figure 2.10.

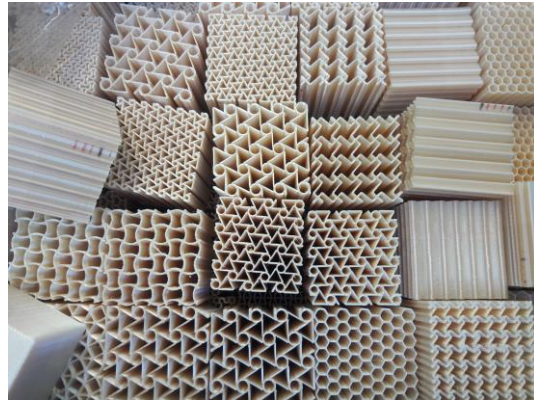


Figure 2.9 In-fill structure and Auxetic in-fill structure

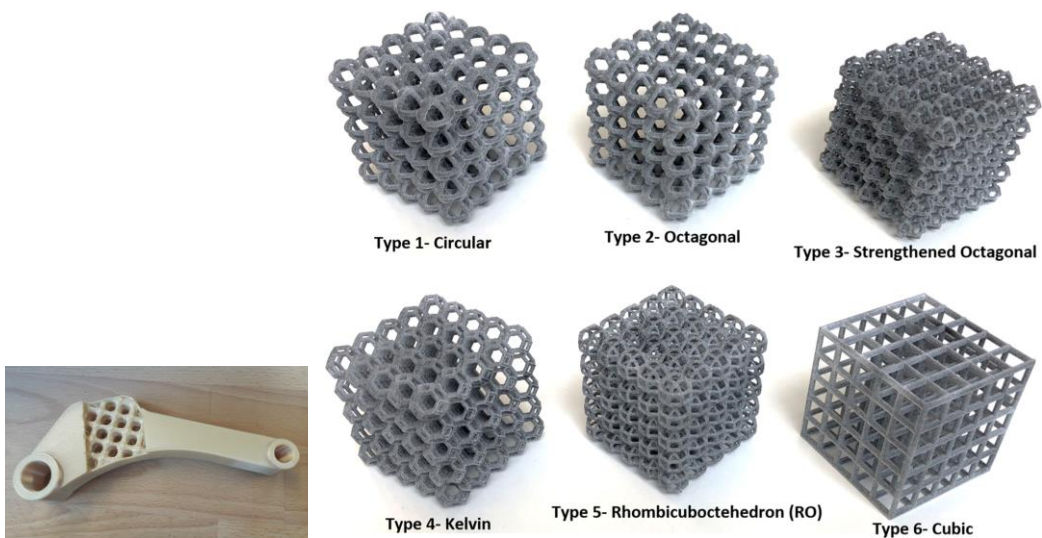


Figure 2.10 Lattice structure [19]

2.3.1. In-fill structures

The in-fill structure is the standard filling provided by FFF technology. When the percentage of in-fill is determined, the printer draws an in-fill pattern automatically according to the input density. There are different types of patterns to be configured. Some common patterns are shown in Figure 2.11.

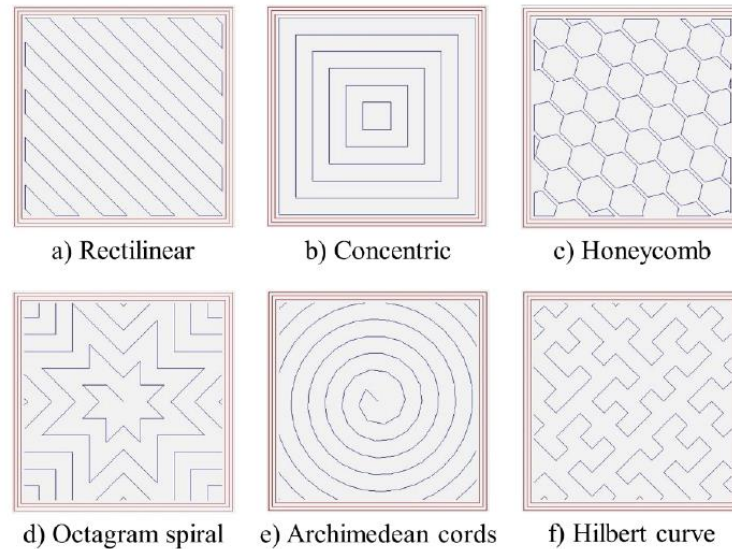


Figure 2.11 Example of In-fill patterns [23]

One of the main advantages of the in-fill structure is that it can be defined automatically by the 3D printing software. That means the pattern and the in-fill percentage can be worked in the CAD procedure automatically. On the other hand, an important limitation is that the in-fill can only be built in the printing direction. The pattern is always print in the XY plane which usually is the in the platform plane. Then, it grows vertically in the Z direction which usually is the perpendicular direction of platform plane. This limitation implies that the same geometry printed in different orientation has the same inner structures but different mechanical behavior.

In addition, there is an interesting structure can be achieved easily by AM technologies. It is auxetic in-fill structure (see right figure of Figure 2.9). The auxetic behavior means that the structure or the material have a negative Poisson's ration. When the structure is stretched, the material in the normal direction of the applied force would become thicker but thinner. This type of structure is wide used in various industries due to its mechanical response. Auxetic structures present higher resilience and shear resistance. Therefore, they can be used for textile fibers, shock absorbs, helmets, car bumpers, etc. [24]. Nowadays,

3D printing allows almost infinite possibilities for auxetic structure's designs and applications.

2.3.2. Lattice structures

Lattice structure is a type of structure that has an order pattern repeated in the space. It is defined by its unit cell. A unit cell is the base of repeatability and the smallest unit showing the same constitutive behavior than the entire lattice. Figure 2.10 shows some examples of lattice structures made by AM techniques.

Comparing the in-fill structures which is default, the main advantage of the lattice structure is that it is independent of the printing orientation. Therefore, better isotropic behavior which is independent of the printing orientation is expected. Nonetheless, lattice structure is designed by CAD manually at the beginning of the printing process.

An important limitation is taken into account. Depending on the shape and outline of the lattice geometry, supporting structure guarantee the printing stability during the printing process. When the external surface of the object is closed, it is impossible to remove the supporting material during the post-process. In the powder based techniques, there is a hole with a minimum diameter of 3.5mm through the external surface to extract the remaining powder which is not sintered. In the FFF technology, removing the supporting material is more complicated. The entire surface of the object requires to be sanded. Although the hydro-soluble support material has reduced the impact in the contour object, an opening to let the material flow out is still required. Furthermore, the modification in the post-processing can affect the mechanical behavior more or less.

2.4. Mechanical behavior of parts made by FFF

FFF is a complicated process. First, the contour of section is printed with the melted filament over the fabrication surface for each layer. Then, the inner space

of the contours is filled with extruded filament following zigzagging trajectories. Usually, the layers division, the in-fill patterns and the supporting structures are automatized by the software. Nevertheless, the effect of these parameters and their influence on the mechanical behavior remains in the reach phase. The printing direction in parts made by FFF affects the mechanical properties directly due to the anisotropy of the layered structures.

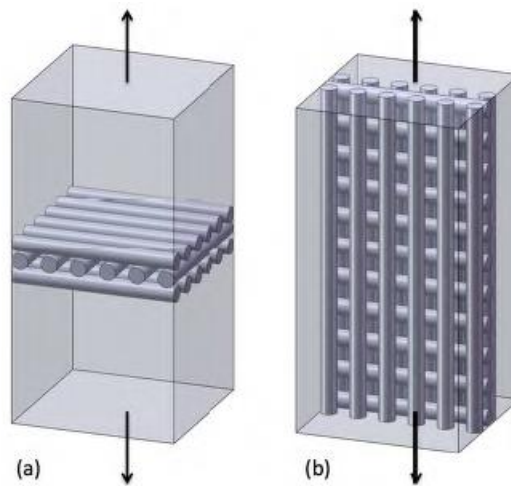


Figure 2.12 Layers disposition depending on the printing orientation [22]

(a) Printing orientation parallel to the force

(b) Printing orientation perpendicular to the force

The printing direction determines how the layers are stacked, and how the filaments are bonded. Figure 2.12 show same geometry printed with the same parameters in different printing direction. Mechanical behavior of parts made by FFF is influenced by the strength of the filament adhesion. The inter-layer unions adhesion performs weaker than the intra-layer unions adhesion [25]. Inter-layer unions used to describe the adjacent layers. While, intra-layer unions used to describe the coplanar filaments.

The joining among filaments depends on the temperature of the extruded material and the strength of the union depends on the neck growth and molecular diffusion on the joint (see Figure 2.13). The bonding process is the same for filaments between inter-layer and intra-layer. Temperatures difference between the extruded

filament and the previous layer create lower adhesion, lower molecular diffusion for the inter-layer unions.

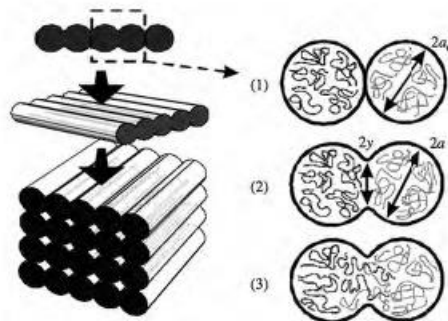


Figure 2.13 Formation process between two filaments [26]

(1) surface contacting (2) neck growth (3) molecular diffusion at interface and randomization

The mechanical behavior is also affected by the direction of the filament disposition in each layer. When the loading is aligned with the filament direction (Figure 2.12 b), the part shows higher ultimate strength than the one when the loading is aligned with the printing direction. (Figure 2.12 a). Therefore, the filaments aligned with the external loads act as a fiber reinforce improving the mechanical resistance [27]. When the compression force is perpendicular to the fabrication direction like Figure 2.14 (left), buckling occurs. The direction become less resistant. On the other hand, when the compression force is parallel to the building direction, the layers' part breaks by shear stress (see Figure 2.14 (right)). Nevertheless, the resistance is higher in this case.



Figure 2.14 Scheme of the compression force influence on the layer direction [22]

Both of layer thickness and filament diameter have the influence on the mechanical behavior as well. The layer thickness mainly affects the heat flow between the following layer printed and the previous layers manufactured. The thinner the layer is, the more temperature diffusion occurs [28]. Meanwhile, Larger diameters improve the fiber performance of the filament, but it also causes stress accumulations [27].

At the same time, raster angle and air gap also affect the mechanical behavior [27-29]. Following the concept in the Section 2.2.2, raster angle has the same effect as the orientation. If the trajectory of the filament is aligned with the traction force, the resistance is higher. To minimize the anisotropy due to the raster angle, an efficient method is changing the raster angle between neighbor layers (consecutive layers). This behavior can homogenize the layer strength [29]. Figure 2.15 shows the results of a tensile test for the test specimens with various raster angles. The specimens fabricated with 0° raster angle that the filaments are parallel to the force present the highest strength. The lowest strength is occurred on the specimens fabricated with 90° raster angle that the filaments are perpendicular to the force. Other specimens fabricated with crossed layer, $45^\circ/-45^\circ$ and $0^\circ/90^\circ$, show similar results.

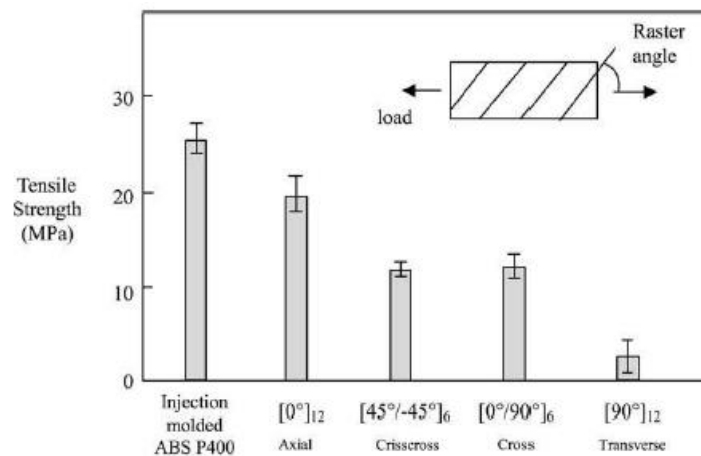


Figure 2.15 Tensile strength of specimens with various raster angle [29]

Alternating the raster angle in neighbor layers (consecutive layers) avoids the buckling issue to be exposed. The raster angle varied 90° among layers allows the filament to distribute the stress in perpendicular direction. Then, the higher compressive strength can be carried depending on the printing direction (see Figure 2.16).

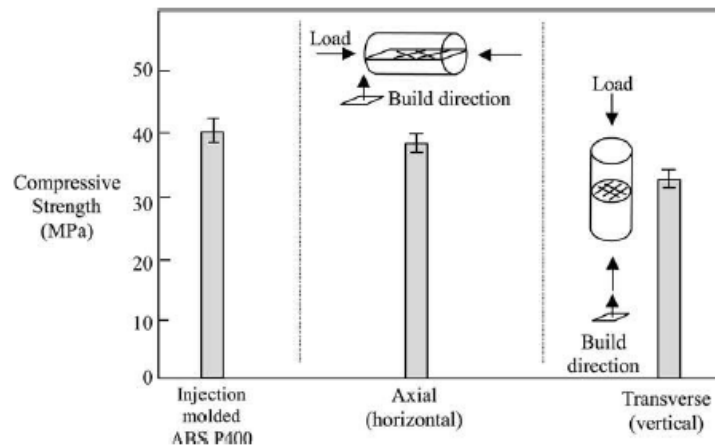


Figure 2.16 Compressive strength of specimens with alternate raster angles, 45° - 45° , and different printing directions. [29]

In-fill density influence the mechanical behavior obviously. Increasing the in-fill density reduces the deformation [30]. Figure 2.17 shows that the strength of the specimens increases with the in-fill density's increasing. However, the in-fill density is not proportional to the strength.

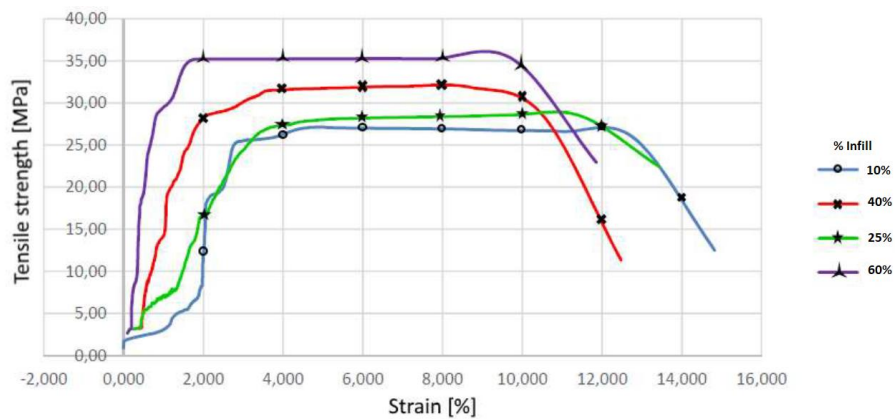


Figure 2.17 Stress-strain curves for specimen's fill density influence comparison [30]

Hence, several parameters influence the mechanical behavior of parts made by FFF. There are many combinations of these parameters. Therefore, more quantitative and qualitative information are required to determine the best choice.

3. Mechanical analysis of FFF pieces

This section describes the strategy developed in this work for the performance analysis of FFF structure. Next, the governing equation that define the mechanical problem are introduced. Then, the constitutive models of the material are described. Finally, the main ideas of the homogenization approach, representative volume element, in this work are described.

3.1. Structure of FFF components

The FFF object is divided in two parts: outer skin and inner structure. Usually, outer skin is constructed by contour and cover, while inner structure is constructed by in-fill or lattice. Different anisotropic properties lead to different mechanical behavior for these structures. According to the content discussed in Section 2.3.4, the mechanical response of FFF parts is highly dependent on the printing direction the trajectories and the filament.

- Contour: Made of aligned filament, surrounds the infill. The Contour is considered as a continuous and homogeneous solid.
- Cover: 100% density crossed pattern with 45° raster angle, covering the top and bottom surfaces.
- In-fill: Made of raster with a certain density that is the raster-to-raster space.
- Lattice: Made of a structure having an ordered pattern repeated in the space.

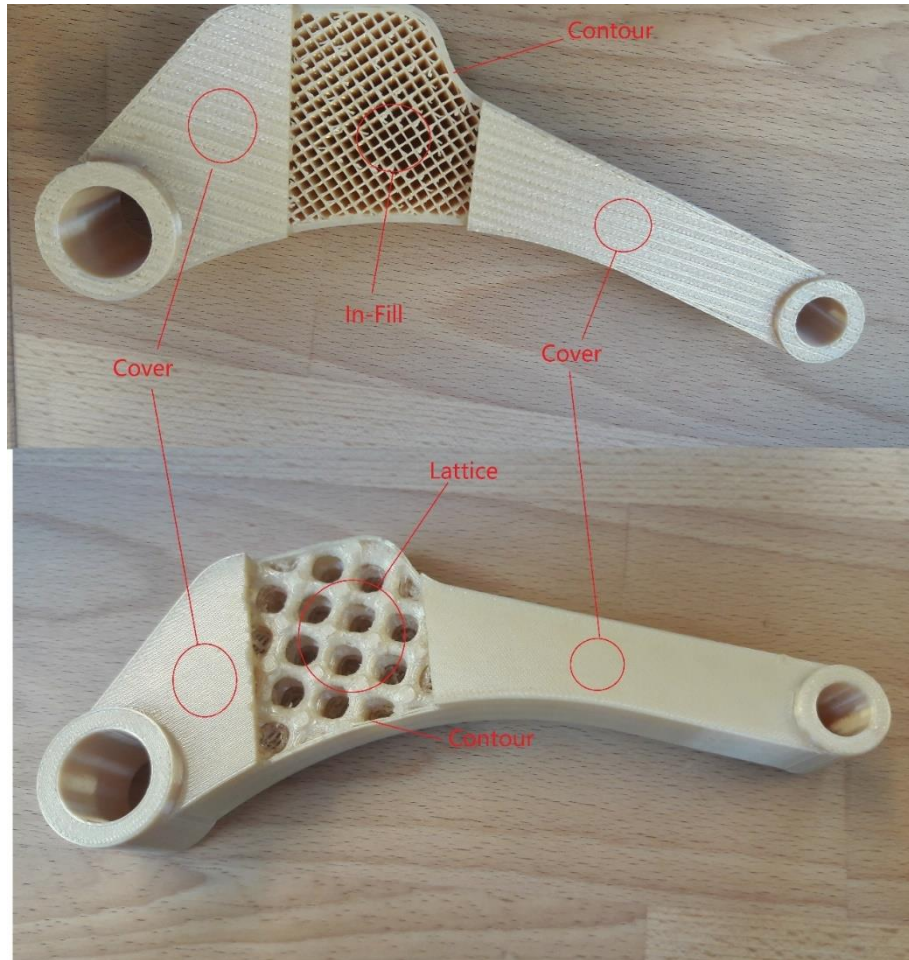


Figure 3.1 Typical three structures in FFF

3.2. Mechanical problem

Assuming that the deformations are small, the elastic potential energy is defined as following:

$$\pi_{int} = \frac{1}{2} \int_V (\boldsymbol{\sigma} : \boldsymbol{\varepsilon}) dV \quad (3.1)$$

Where $\boldsymbol{\sigma}$ is the stress field and $\boldsymbol{\varepsilon}$ is the strain field.

The potential energy of the applied loads is defined as:

$$\pi_{ext} = - \int_V (\mathbf{b} \cdot \mathbf{u}) dV - \int_S (\bar{\mathbf{t}} \cdot \mathbf{u}) dS \quad (3.2)$$

Where \mathbf{u} is the displacement field in the solid, \mathbf{b} is the body force and $\bar{\mathbf{t}}$ is the surface traction.

Therefore, the total potential energy is:

$$\pi = \pi_{int} + \pi_{ext} \quad (3.3)$$

The necessary and sufficient condition for a body to be in equilibrium is:

$$\delta\pi = \delta\pi_{ext} + \delta\pi_{ext} = 0 \quad (3.4)$$

Where,

The work of the internal forces (δW_{int})

$$\delta\pi_{int} = \int_V (\boldsymbol{\sigma} : \delta\boldsymbol{\varepsilon}) dV = \delta W_{int} \quad (3.5)$$

The work of the external forces (δW_{ext})

$$\delta\pi_{int} = - \int_V (\mathbf{b} \cdot \delta\mathbf{u}) dV - \int_S (\bar{\mathbf{t}} \cdot \delta\mathbf{u}) dS = -\delta W_{ext} \quad (3.6)$$

Hence, the minimization of the total potential energy from Eq. 3.4-3.6 leads to (Principle of the virtual works):

$$\delta W_{ext} = \delta W_{int} \quad (3.7)$$

The virtual strain is defined as:

$$\delta\boldsymbol{\varepsilon} = \nabla^s \delta\mathbf{u} \quad \text{in } V, \quad \delta\mathbf{u} = 0 \quad \text{on } S_u \quad (3.8)$$

Where $\delta\mathbf{u}$ is the virtual displacement.

The principle of virtual works corresponds to the weak form of equilibrium, in fact integrating by parts:

$$\delta W_{int} = - \int_V \delta \mathbf{u} \cdot (\nabla \cdot \boldsymbol{\sigma}) dV + \int_{S_\sigma} \delta \mathbf{u} \cdot (\boldsymbol{\sigma} \cdot \mathbf{n}) dV + \int_{S_u} \delta \mathbf{u} \cdot (\boldsymbol{\sigma} \cdot \mathbf{n}) dV \quad (3.9)$$

Where,

$$\int_{S_u} \delta \mathbf{u} \cdot (\boldsymbol{\sigma} \cdot \mathbf{n}) dV = 0 \quad (3.10)$$

Then, the weak form of the equations of equilibrium for the volume:

$$\int_V \delta \mathbf{u} \cdot (\nabla \cdot \boldsymbol{\sigma} + \mathbf{b}) dV + \int_{S_\sigma} \delta \mathbf{u} \cdot (\bar{\mathbf{t}} - \boldsymbol{\sigma} \cdot \mathbf{n}) dS = 0 \quad \forall \delta \mathbf{u} \quad (3.11)$$

And its boundary:

$$\nabla \cdot \boldsymbol{\sigma} + \mathbf{b} = \mathbf{0} \quad \text{in } V, \quad \boldsymbol{\sigma} \cdot \mathbf{n} = \bar{\mathbf{t}} \quad \text{on } S_\sigma \quad (3.12)$$

For a linear elastic material, the constitutive equation can be expressed as:

$$\boldsymbol{\sigma} = \mathbf{C} : \boldsymbol{\varepsilon} \quad (3.13)$$

Where \mathbf{C} is the constitutive tensor of the material, also called stiffness tensor.

3.3. Constitutive laws

In the section, the linear-elasticity of anisotropic cellular solids, of [31], we can see the following

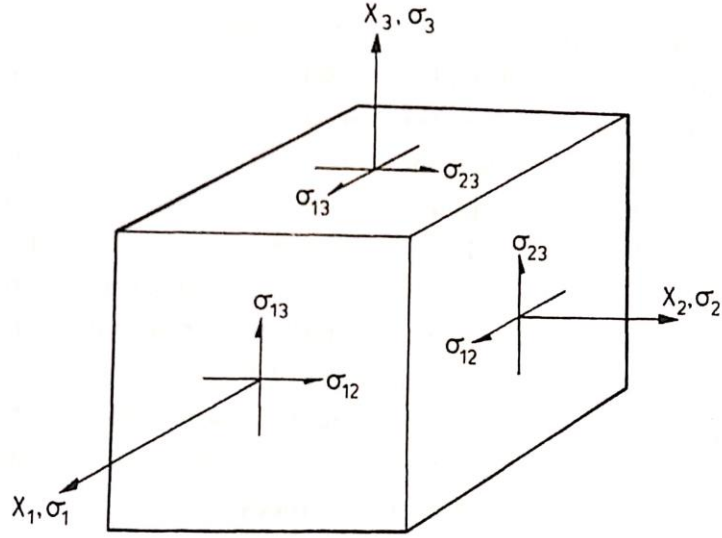


Figure 3.2 The coordinate system showing axes X_1 , X_2 and X_3 . The normal stresses are σ_1 , σ_2 and σ_3 . The shear stresses are σ_{12} , σ_{23} and σ_{31} . [31]

The strains are computed by Hook's law. The general expression takes following form:

$$\begin{pmatrix} \varepsilon_1 \\ \varepsilon_2 \\ \varepsilon_3 \\ \gamma_{12} \\ \gamma_{31} \\ \gamma_{23} \end{pmatrix} = \begin{pmatrix} S_{11} & S_{12} & S_{13} & S_{14} & S_{15} & S_{16} \\ S_{21} & S_{22} & S_{23} & S_{24} & S_{25} & S_{26} \\ S_{31} & S_{32} & S_{33} & S_{34} & S_{35} & S_{36} \\ S_{41} & S_{42} & S_{43} & S_{44} & S_{45} & S_{46} \\ S_{51} & S_{52} & S_{53} & S_{54} & S_{55} & S_{56} \\ S_{61} & S_{62} & S_{63} & S_{64} & S_{65} & S_{66} \end{pmatrix} \cdot \begin{pmatrix} \sigma_1 \\ \sigma_2 \\ \sigma_3 \\ \sigma_{12} \\ \sigma_{31} \\ \sigma_{23} \end{pmatrix} \quad (3.14)$$

The coefficients S_{ij} are the components of the compliance matrix, which is the inverse of the constitutive tensor:

$$\underline{S} = \underline{C}^{-1} \quad (3.15)$$

Then,

$$\underline{\varepsilon} = \underline{S} \cdot \underline{\sigma} \quad (3.16)$$

Due to the symmetric of the compliance matrix, the properties of anisotropic material are described by 21 parameters:

$$S = \begin{pmatrix} S_{11} & S_{12} & S_{13} & S_{14} & S_{15} & S_{16} \\ & S_{22} & S_{23} & S_{24} & S_{25} & S_{26} \\ & & S_{33} & S_{34} & S_{35} & S_{36} \\ & & & S_{44} & S_{45} & S_{46} \\ & & & & S_{55} & S_{56} \\ \text{sym} & & & & & S_{66} \end{pmatrix} \quad (3.17)$$

3.3.1. Orthotropy

Orthotropic materials are a subset of anisotropic materials. Orthotropy means that the material properties change along three mutually-orthogonal twofold axes of rotational symmetry. This symmetry reduces the number of elastic modules. Thus, the compliance matrix for an orthotropic material depends on 9 independent parameters:

$$S = \begin{pmatrix} S_{11} & S_{12} & S_{13} & 0 & 0 & 0 \\ & S_{22} & S_{23} & 0 & 0 & 0 \\ & & S_{33} & 0 & 0 & 0 \\ & & & S_{44} & 0 & 0 \\ & & & & S_{55} & 0 \\ \text{sym} & & & & & S_{66} \end{pmatrix} \quad (3.18)$$

The three Young's modulus for loading in the X_1, X_2 and X_3 directions are:

$$E_1 = \frac{1}{S_{11}} \quad E_2 = \frac{1}{S_{22}} \quad E_3 = \frac{1}{S_{33}} \quad (3.19)$$

The three shear modulus are:

$$G_{12} = \frac{1}{S_{44}} \quad G_{31} = \frac{1}{S_{55}} \quad G_{23} = \frac{1}{S_{66}} \quad (3.20)$$

Poisson's ratio ν_{ij} is defined as the negative of the strain in the j direction divided by the strain in the i direction, for normal loading in the i direction ($\nu_{ij} = -\frac{\varepsilon_j}{\varepsilon_i}$), so that:

$$\begin{aligned} v_{12} &= -\frac{S_{21}}{S_{11}} & v_{13} &= -\frac{S_{31}}{S_{11}} & v_{23} &= -\frac{S_{32}}{S_{22}} \\ v_{21} &= -\frac{S_{12}}{S_{22}} & v_{31} &= -\frac{S_{13}}{S_{33}} & v_{32} &= -\frac{S_{23}}{S_{33}} \end{aligned} \quad (3.21)$$

Where only three of them are independent. Considering the symmetry, $S_{ij} = S_{ji}$, and substitution from Eq.3.19. the following relations are obtained:

$$\frac{v_{12}}{E_1} = \frac{v_{21}}{E_2} = -S_{12} \quad \frac{v_{13}}{E_1} = \frac{v_{31}}{E_3} = -S_{13} \quad \frac{v_{23}}{E_2} = \frac{v_{32}}{E_3} = -S_{23} \quad (3.22)$$

Then, the compliance matrix becomes:

$$S = \begin{pmatrix} \frac{1}{E_1} & -\frac{v_{21}}{E_2} & -\frac{v_{31}}{E_3} & 0 & 0 & 0 \\ -\frac{v_{12}}{E_1} & \frac{1}{E_2} & -\frac{v_{32}}{E_3} & 0 & 0 & 0 \\ -\frac{v_{13}}{E_1} & -\frac{v_{23}}{E_2} & \frac{1}{E_3} & 0 & 0 & 0 \\ 0 & 0 & 0 & \frac{1}{G_{12}} & 0 & 0 \\ 0 & 0 & 0 & 0 & \frac{1}{G_{31}} & 0 \\ 0 & 0 & 0 & 0 & 0 & \frac{1}{G_{23}} \end{pmatrix} \quad (3.23)$$

3.3.2. Transverse isotropy

The transversely isotropic material is one type of orthotropic material where exists one symmetric axis normal to an isotropic plane. In other words, the properties in the isotropic plane are same. If we consider the isotropic plane is $X_1 X_2$, the properties are same both in X_1 and X_2 . Then the compliance matrix depends on 5 independent parameters:

$$S = \begin{pmatrix} S_{11} & S_{12} & S_{13} & 0 & 0 & 0 \\ & S_{11} & S_{13} & 0 & 0 & 0 \\ & & S_{33} & 0 & 0 & 0 \\ & & & 2(S_{11} - S_{12}) & 0 & 0 \\ sym & & & & S_{55} & 0 \\ & & & & & S_{55} \end{pmatrix} \quad (3.24)$$

Then, the following equalities hold:

$$\begin{aligned} E_1 = E_2 = E_{iso} \quad \nu_{31} = \nu_{32} = \nu \quad \nu_{12} = \nu_{21} = \nu_{iso} \\ G_{31} = G_{23} = G \quad G_{12} = G_{21} = G_{iso} = \frac{E_{iso}}{2(1 + \nu_{iso})} \end{aligned} \quad (3.25)$$

The compliance matrix can be written by five independent properties ($E_{iso}, E_3, \nu, \nu_{iso}, G$) as the following:

$$S = \begin{pmatrix} \frac{1}{E_{iso}} & -\frac{\nu_{iso}}{E_{iso}} & -\frac{\nu}{E_3} & 0 & 0 & 0 \\ -\frac{\nu_{iso}}{E_{iso}} & \frac{1}{E_{iso}} & -\frac{\nu}{E_3} & 0 & 0 & 0 \\ -\frac{\nu}{E_3} & -\frac{\nu}{E_3} & \frac{1}{E_3} & 0 & 0 & 0 \\ 0 & 0 & 0 & \frac{1}{G_{iso}} & 0 & 0 \\ 0 & 0 & 0 & 0 & \frac{1}{G} & 0 \\ 0 & 0 & 0 & 0 & 0 & \frac{1}{G} \end{pmatrix} \quad (3.26)$$

3.3.3. Isotropy

The isotropic material has the same response in all directions. Therefore:

$$\begin{aligned} E_1 = E_2 = E_3 = E \quad G_{12} = G_{31} = G_{23} = G \\ \nu_{12} = \nu_{21} = \nu_{13} = \nu_{31} = \nu_{23} = \nu_{32} = \nu \end{aligned} \quad (3.27)$$

Then, the compliance matrix reduces to:

$$S = \begin{pmatrix} \frac{1}{E} & -\frac{\nu}{E} & -\frac{\nu}{E} & 0 & 0 & 0 \\ -\frac{\nu}{E} & \frac{1}{E} & -\frac{\nu}{E} & 0 & 0 & 0 \\ -\frac{\nu}{E} & -\frac{\nu}{E} & \frac{1}{E} & 0 & 0 & 0 \\ 0 & 0 & 0 & \frac{1}{G} & 0 & 0 \\ 0 & 0 & 0 & 0 & \frac{1}{G} & 0 \\ 0 & 0 & 0 & 0 & 0 & \frac{1}{G} \end{pmatrix} \quad (3.28)$$

Where, the shear modulus defined as:

$$G = \frac{E}{2(1 + \nu)} \quad (3.29)$$

Finally, the compliance matrix in isotropy only depending on 2 independent parameters, the elastic modulus E and the Poisson's ratio ν .

3.4. Homogenization-Representative Volume Element

Simulating complicated geometries with in-fill or lattice is challenging. To reduce such computational cost, homogenization methods can be used. Hence, heterogeneous structure is reduced to equivalent homogeneous constitutive models. In the other words, defining an equivalent anisotropic homogeneous constitutive tensor to get the same global structural behavior.

The computational homogenization is based on the concept of Representative Volume Element (RVE). RVE represents the local geometry of unit cell which characterizes the in-fill or lattice structure. This is used to obtain the mechanical response of the global structural model. In the other words, an RVE is the smallest volume that can represent the overall macrostructure behavior. It must satisfy two conditions [31]:

- An RVE must reflect the material or geometry of the in-fill or lattice
- The response under uniform boundary conditions must be equivalent

When there is no sufficient information in an RVE, the boundary condition used will control the response obtained. Therefore, the correlation between RVE dimension and boundary condition are crucial for the homogenization method's proper using.

3.4.1. First-order homogenization

The basis of the first-order computational homogenization is introduced by Suquet [33]. The four steps are:

- 1) Definition of the representative volume element (RVE) with known constitutive behavior
- 2) Formulation of the local boundary conditions from the global structure variables and their application on the RVE (global-to-local transition).
- 3) Calculation of the output variables of the global structure from the analysis of the deformed RVE (local-to-global transition)
- 4) Obtaining the relation between the global structure input and the output variables.

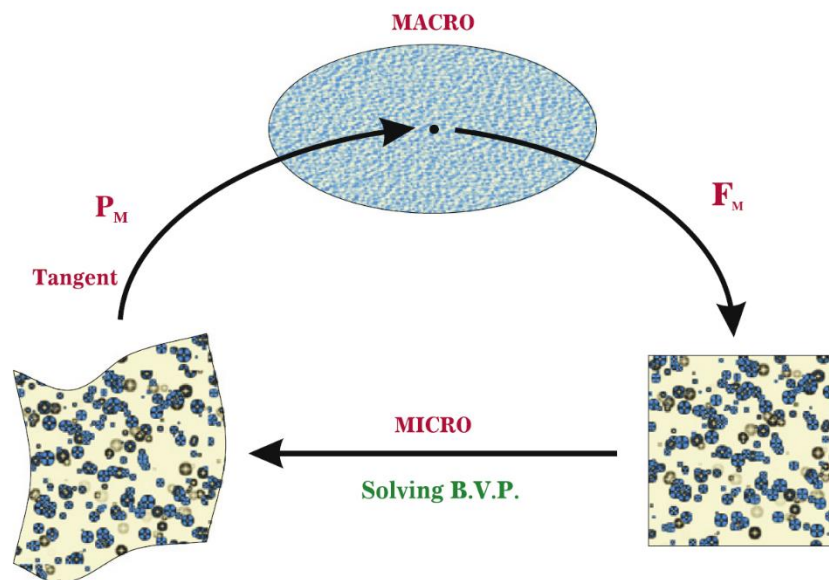


Figure 3.3 First-order computational homogenization [34]

The mechanical properties of the global structure are defined by the average values of the stresses and strains of the RVE. The homogenization is a process that applying an average deformation on the RVE with the appropriate boundary conditions which lead the corresponding average stresses. The following section will introduce the methodology of the homogenization process step by step.

3.4.1.1. Surface average approach

According to the introduce in Pasini [35], the surface average approach is exposed in the following.

The surface average approach is based on the application of which is uniform traction or prescribed displacement to the surface of the RVE. Uniform tractions generate uniform stress fields while applicated displacements generate uniform strain field.

Average stresses can be computed as:

$$\bar{\sigma} = \frac{1}{V_{RVE}} \int_{V_{RVE}} \sigma dV_{RVE} = \frac{1}{V_{RVE}} \int_{\Gamma_{RVE}} \frac{1}{2} (t_i y_j + t_j y_i) d\Gamma_{RVE} \quad (3.30)$$

Where,

$\bar{\sigma}$: The global stress tensor

σ : The local (RVE) stress tensor

t_i : The traction imposed on the RVE boundary

y_j : The local coordinates of the RVE boundary

Γ_{RVE} : The RVE boundary

The subscripts i and j follow the Einstein notation.

The relationship between the strain tensor generated in the RVE and the average strain tensor in the global scale can be written as the following by using divergence theorem:

$$\bar{\epsilon} = \frac{1}{V_{RVE}} \int_{V_{RVE}} \epsilon dV_{RVE} = \frac{1}{V_{RVE}} \int_{\Gamma_{RVE}} \frac{1}{2} (u_i n_j + u_j n_i) d\Gamma_{RVE} \quad (3.31)$$

Where,

$\bar{\epsilon}$: The strain tensor generated in the RVE

ε : The average strain tensor in the global scale

u_i : The displacement imposed on the RVE boundary

n_j : The component of the vector normal to the RVE boundary

The imposed displacements and the imposed tractions are generally uniform. Nevertheless, different boundary displacements integrated over the boundary can present identical average strain. Therefore, defining the problem is not unique.

Different boundary conditions can be applied to predict the RVE properties. The main alternatives are the Dirichlet boundary condition (DBC), the Neumann boundary condition (NBC) and the periodic boundary condition (PBC). DBC and PBC apply a unit strain on the nodes of the boundary defining the RVE, while NBC applies tractions. For these boundary conditions, the governing equations of the elastic problem can be written as:

$$\sigma(x)_{ij,j} = 0 \quad \text{and} \quad x \in \Omega \quad \begin{cases} u_i|_{\Gamma} = \bar{\varepsilon}_{ij}^{kl} x_j|_{\Gamma_{RVE}} & DBC \\ T_i|_{\Gamma} = \bar{\sigma}_{ij}^{kl} n_j|_{\Gamma_{RVE}} & NBC \\ T_i|_{\Gamma} = \bar{\sigma}_{ij}^{kl} n_j|_{\Gamma_{RVE}} & PBC \end{cases} \quad (3.32)$$

Where,

$\sigma_{i,j}$: The components of the stress tensor in the RVE domain

$(\cdot)_{,i}$: The gradient of the field quantity with respect to the global coordinate system

x_i : The nodal coordinates

$\bar{\varepsilon}_{ij}^{kl}$: The global unit strain for kl -th strains over the RVE boundaries.

$\bar{\sigma}_{ij}^{kl}$: The global unit stress for kl -th traction over the RVE boundaries.

$A +$ and $A -$: The A -th pair of two opposite parallel surfaces for the RVE boundary.

For DBC and PBC, six uniform strains states require to be applied to the RVE in 3D. The global strain $\bar{\varepsilon}_{ij}^{kl}$ can be expressed as a function of the local strain ε_{ij}^{kl} as:

$$\bar{\varepsilon}_{ij}^{kl} = \mathbf{M}\varepsilon_{ij}^{kl} \quad (3.33)$$

Where, \mathbf{M} is a local structural strain tensor.

Then, the calculation of the local strain at any point from an arbitrary average strain is the following:

$$\varepsilon = \mathbf{M}\bar{\varepsilon} \quad (3.34)$$

Using the Hook' law, yield:

$$\sigma = \mathbf{C}\varepsilon \quad (3.35)$$

Substituting Eq.3.34 and Eq.3.35 in Eq.3.30. the average stress on the RVE can be written as:

$$\bar{\sigma} = \frac{1}{V_{RVE}} \int_{V_{RVE}} \sigma dV_{RVE} = \frac{1}{V_{RVE}} \int_{V_{RVE}} \mathbf{C}\mathbf{M}dV_{RVE}\bar{\varepsilon} \quad (3.36)$$

Defining the constitutive tensor which describes the effective elastic properties of the RVE as:

$$\bar{\mathbf{C}} = \frac{1}{V_{RVE}} \int_{V_{RVE}} \mathbf{C}\mathbf{M}dV_{RVE} \quad (3.37)$$

For NBC, six uniform stress states are applied to the RVE. Similarly, as DBC and PBC cases, a local structural stress tensor \mathbf{N} is defined to relate the average stress $\bar{\sigma}^{kl}$ with the local stress σ^{kl} :

$$\bar{\sigma}^{kl} = \mathbf{N}\sigma^{kl} \quad (3.38)$$

\mathbf{N} can also obtain the local stress at any point from an arbitrary global stress.

The effective material properties are obtained by Eq.3.31, Eq.3.35 and 3.38.

$$\bar{\boldsymbol{\varepsilon}} = \frac{1}{V_{RVE}} \int_{V_{RVE}} \boldsymbol{\varepsilon} dV_{RVE} = \frac{1}{V_{RVE}} \int_{V_{RVE}} \mathbf{C}^{-1} \boldsymbol{\sigma} dV_{RVE} = \frac{1}{V_{RVE}} \int_{V_{RVE}} \mathbf{C}^{-1} \mathbf{N}^{-1} dV_{RVE} \bar{\boldsymbol{\sigma}} \quad (3.39)$$

Define the compliance tensor as:

$$\bar{\mathbf{S}} = \frac{1}{V_{RVE}} \int_{V_{RVE}} \mathbf{C}^{-1} \mathbf{N}^{-1} dV_{RVE} \quad (3.40)$$

3.4.1.2. The Periodic boundary condition of RVE used in this TFM work

In this paper, PBC would be used with RVE.

According to Pasini [34], boundary conditions are essential to any homogenization method because they influence the accuracy of the solution. DBC and NBC cannot ensure the continuity of the displacement field through the lattice and the results are highly depending on the RVE size and shape. However, PBC has no limitations on the type of RVE because it can ensure the continuity on the boundaries.

On the other hand, DBC applies a uniform displacement that constrains the RVE to maintain its plane section. Therefore, the RVE is over-constrained. This leads to the RVE properties are stiffer than expected [36]. Meanwhile, NBC has the opposite issue. Due to the RVE shape, unbalanced tractions between opposite sides are found. This leads to the under-constrained RVE with lower stiffness. Nevertheless, DBC and NBC both seems to converge with the increasing the number of cells that defines the RVE [37].

PBC guarantees the unicity of the solution. When the three boundary conditions are compared, DBC results to the upper bound solution while NBC results to the lower bound.

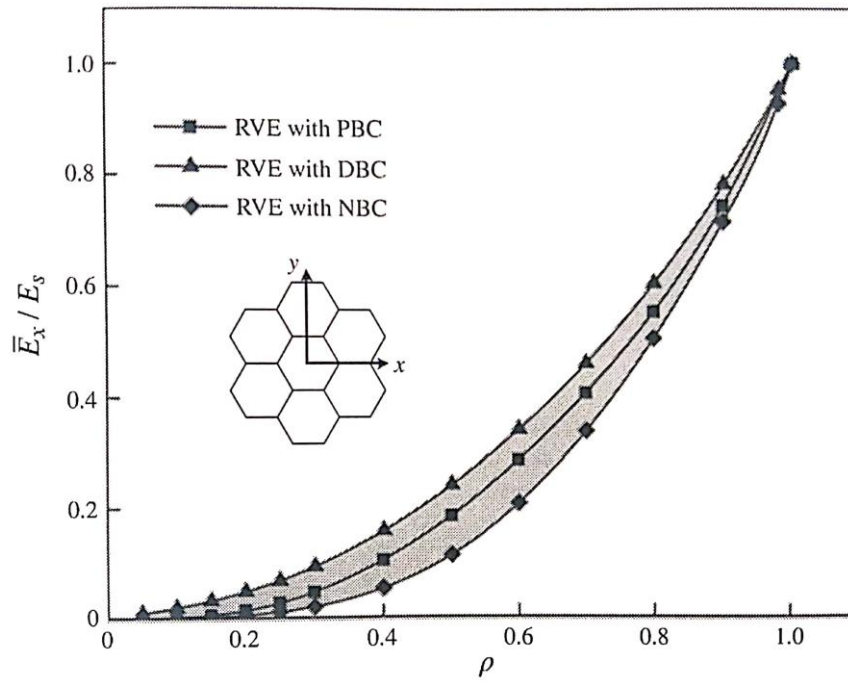


Figure 3.4 Effective Young's modulus, \bar{E}_x , as function of relative density for the hexagonal cell. Results obtained with the DBC and NBC bound those calculated with the PBC [35].

4. Performance analysis of demonstrators

This chapter presents the performance analysis of the demonstrators using the methodology developed in this work. These simulations have been done by using the finite element software COMET, KRATOS and GID which are developed by International Centre for Numerical Methods in Engineering (CIMNE). Kratos is used to characterize the in-fill structures by homogenization techniques via RVE. Comet is used for the mechanical analysis of the demonstrators. The simulation calculated by a PC with *CPU: 10700K, RAM: 128GB, SSD: 1TB*

4.1. Case1 Beam

4.1.1. Introduction

To characterize the material of contour and cover, it is performed that tensile test on dog bone sample printed with the corresponding patterns. Then the strategy developed in this work is validated (square cross section samples). PC-ABS, Polycarbonate-Acrylonitrile Butadiene Styrene, is the material which is considered in the work. PC-ABS 3D presents enhanced printing performance, low warpage, dimensional exactness and high resolution like ABS. Furthermore, this material also has the good mechanical properties, impact strength, temperature resistance and ultraviolet ray (UV) resistance like PC. A FFF made of different parts according to the printing pattern: Cover, Contour and In-fill.

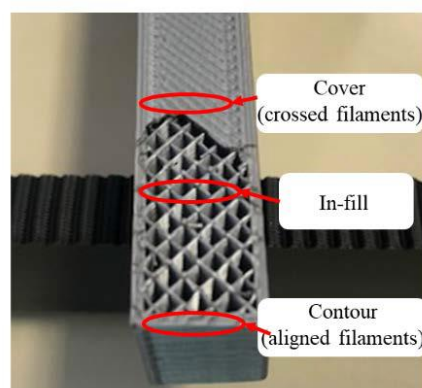


Figure 4.1 Different zones of a FFF component in this case

The printing pattern has a significant role on the material characterization and the orientation of both the isotropic plane and the weakest direction. In case of the cover and the in-fill, the printing plane is isotropic due to the symmetry of the pattern. The anisotropy develops in the build direction. In case of the contour, the stiffness in the filament direction (which is the anisotropic direction) is higher than the one of the intra-layer unions between filaments. The obtained results in [39] indicate that both the intra-layer (coplanar filaments) and the inter-layer (adjacent layer) bonds play a significant role in the behavior of the FFF samples. In this sense, the use of the thermal chamber reduces the temperature gradient between the deposited filament and the last layer built. This fact strengthens the unions, improves mechanical performance, and decreases the degree of orthotropy. Furthermore, the results obtained confirm that the stiffness on the direction of the extruded filament is higher than the one of the intra-layer unions between contiguous filaments. However, the rigidity of the inter-layer cohesion of adjacent layers is the lowest. Figure 4.2 illustrates 3 geometrically identical samples, but printed in 3 different orientations, subjected to identical stretching. Even though the global stresses are the same in all the three cases, the state of the stresses is different in the material axes of each specimen. Due to the filament orientation, the sample on the right side has the highest strength along the tensile axis.

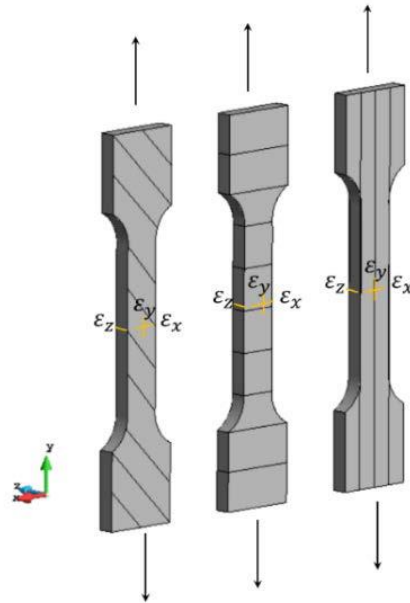


Figure 4.2 Different building orientations of a test specimen manufactured by FFF

4.1.2. Methodology

In this work, a novel methodology for the analysis of the mechanical performance of FFF built components that takes into account the different mechanical properties of the contour, the cover and the inner structure is developed. Material properties of each part is identified experimentally and computationally (section 4.1.3).

First, the geometry is divided into different volumes according to the printing patterns. Extensive experimental tests are performed to evaluate the anisotropic properties of the contour and the cover. PC-ABS 3D is intended for use in FFF in 3D printing applications. PC-ABS 3D Dog-bone samples are manufactured exclusively with aligned and crossed filaments to represent the contour and the cover, respectively. The samples are tested uniaxially at different orientations. Anisotropic linear elastic constitutive models are considered to describe the mechanical behavior of contour, cover and in-fill. A geometrical relationship is found between the material parameters at different orientation and the raw material. The constitutive matrix of the inner structure is modelled using

computational homogenization technique by Representative Volume Element (RVE).

4.1.3. Result

4.1.3.1. Experimental and computational material characterization

In this section, the developed constitutive model and the computational strategy for the performance analysis of the components built by FFF technology are presented (see Figure 4.3).

As mentioned, a component built by FFF technology includes three distinct zones according to their printing pattern and orientation revealing different mechanical behavior. These zones are the contour, the cover and the inner structure (in-fill). The contour is made of aligned filaments with the external edges of the FFF components while the cover is made of crossed filaments with rectilinear pattern. The inner structure (in-fill) is made of raster with a certain density that is the raster-to-raster space.

The mechanical properties of the printed material are different from those of the raw material. The contour, the cover and the in-fill are anisotropic while the raw material is isotropic. Moreover, according to the printing pattern, the anisotropic properties differ. The printing pattern has a significant role on the material characterization and the orientation of both the isotropic plane and the weakest direction. In case of the cover and the in-fill, the printing plane is isotropic due to the symmetry of the pattern. The anisotropy develops in the build direction. In case of the contour, the stiffness in the filament direction (which is the anisotropic direction) is higher than the one of the intra-layer unions between filaments.

Standard FE analysis of FFF components with in-fill or lattice inner structures is challenging due to the complexity of the mesh generation appropriate for such complex geometries. The inner structure is heterogeneous, thus its discretization by the standard FE mesh leads to an exaggerated element number. Therefore,

the numerical computations become unfeasible. The computational homogenization technique represents the corresponding anisotropic behavior using an equivalent homogeneous continuum profiting from its repetitive cell structure.

Even though the inner structure is characterized computationally, the input data for the homogenization technique is fed from the experimental characterization of the aligned filaments of the contour.

Overall, this work distinguishes between the mechanical behavior of the contour, the cover and the in-fill. Thus, their respective mechanical properties are determined separately. However, separate experimental tests for the characterization of the contour, the cover and the in-fill may be challenging. Alternatively, the numerical model can be calibrated by a sensitivity analysis based on the raw material properties.

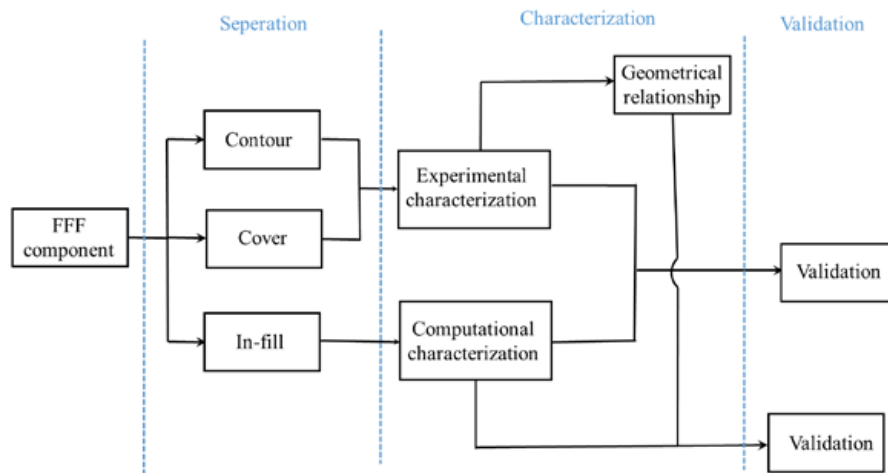


Figure 4.3 The strategy for the material characterization

4.1.3.1.1. Experimental tensile test on dog-bone samples

This section describes the experimental material characterization to determine the material constitutive tensor for the contour and the cover of FFF components.

The tensile test is performed in accordance with the ASTM D638 standard Test Method for Tensile Properties of Plastics. Sixty dog-bone samples of PC-ABS 3D material are manufactured by FFF with different printing orientations (P-Z, P-ZX, P-ZY, P-H, I-Z, I-ZX, I-ZY and I-H) following the printing patterns used for contour and cover (see section 4.3.1.1.1). Standard specimen 'TYPE I' is chosen for the performance of these tests. The dimension of each specimen is shown in Figure 4.4 and Table 4.1. From the tensile test results, Young's and shear moduli are obtained.

The isotropic elastic properties of the pre-printed material are: Young's modulus $E_{Raw} = 2.7 \text{ GPa}$ and Poisson's $\nu_{Raw} = 0.353$ from Matweb [38].

Due to economic limit, we did not take DIC equipment to get the Poisson's ratio. The sensitivity analysis shows that the Poisson's ratio affects the results very limited. The error of the simulation cases with Poisson's ratio in the range of 0.34 to 0.38 can be neglected. All the experimental results are plotted in Figure 4.5.

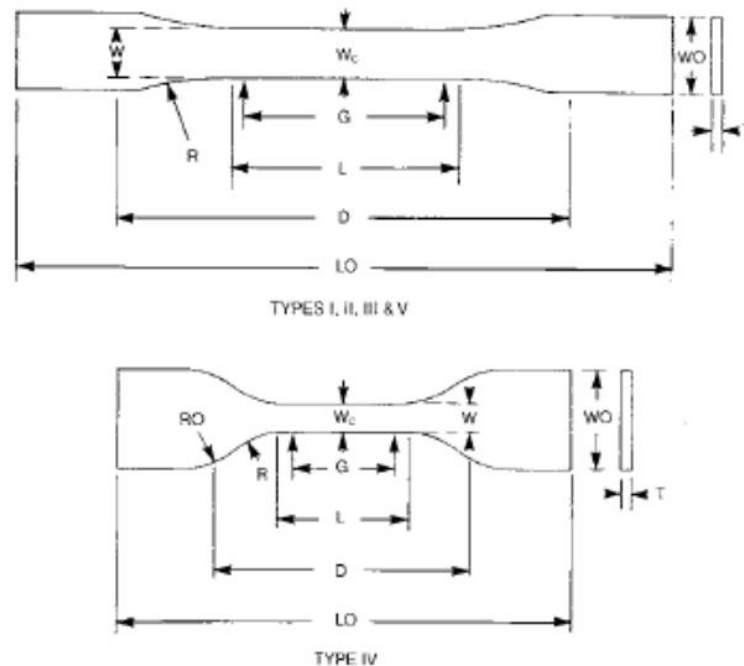


Figure 4.4 Dog-bone specimen dimension

Dimensions (see drawings)	7 (0.28) or under		Over 7 to 14 (0.28 to 0.55), incl	4 (0.16) or under		Tolerances
	Type I	Type II	Type III	Type IV ^B	Type V ^{C,D}	
W—Width of narrow section ^{E,F}	13 (0.50)	6 (0.25)	19 (0.75)	6 (0.25)	3.18 (0.125)	±0.5 (±0.02) ^{B,C}
L—Length of narrow section	57 (2.25)	57 (2.25)	57 (2.25)	33 (1.30)	9.53 (0.375)	±0.5 (±0.02) ^C
WO—Width overall, min ^G	19 (0.75)	19 (0.75)	29 (1.13)	19 (0.75)	...	+ 6.4 (+ 0.25)
WO—Width overall, min ^G	9.53 (0.375)	+ 3.18 (+ 0.125)
LO—Length overall, min ^H	165 (6.5)	183 (7.2)	246 (9.7)	115 (4.5)	63.5 (2.5)	no max (no max)
G—Gage length ^I	50 (2.00)	50 (2.00)	50 (2.00)	...	7.62 (0.300)	±0.25 (±0.010) ^C
G—Gage length ^I	25 (1.00)	...	±0.13 (±0.005)
D—Distance between grips	115 (4.5)	135 (5.3)	115 (4.5)	65 (2.5) ^J	25.4 (1.0)	±5 (±0.2)
R—Radius of fillet	76 (3.00)	76 (3.00)	76 (3.00)	14 (0.56)	12.7 (0.5)	±1 (±0.04) ^C
RO—Outer radius (Type IV)	25 (1.00)	...	±1 (±0.04)

Table 4.1 Specimen Dimensions for Thickness, T, mm (in.)^A

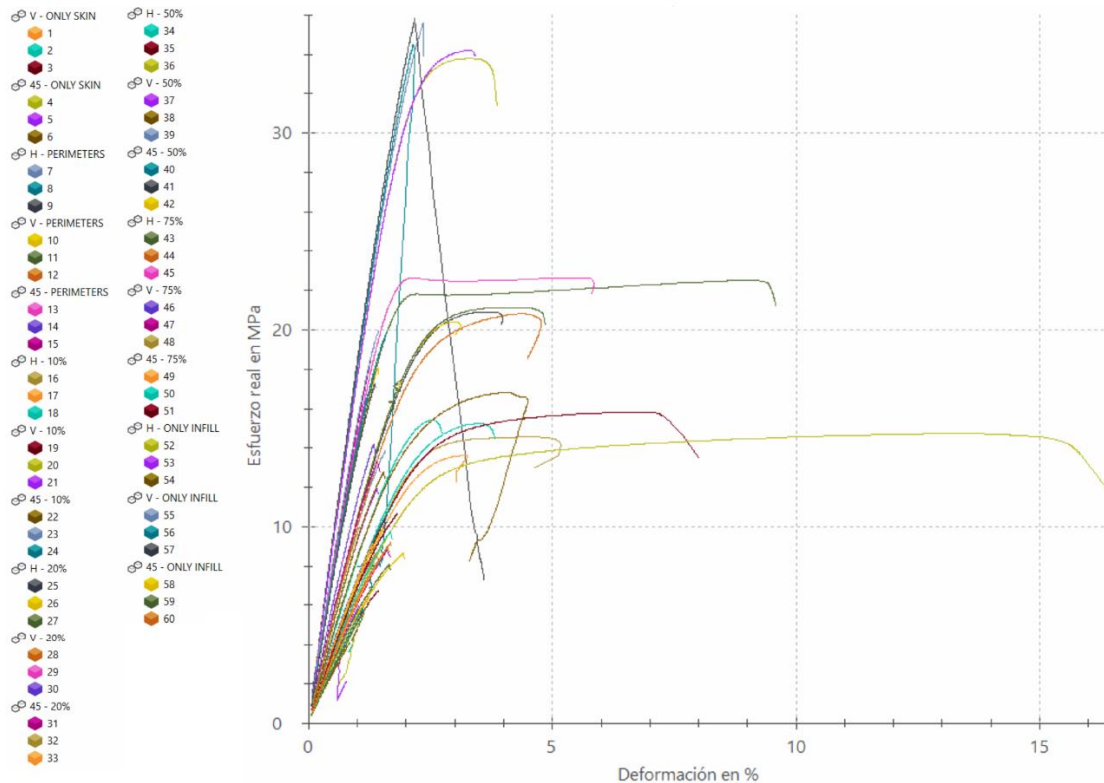


Figure 4.5 Tensile test plot (dog-bone specimens)

4.1.3.1.1.1. Material characterization of the contour and cover

The nomenclature used for the specimens corresponds to contour (P) and cover (I) (Figure 3.4). In the case of contour (P), the filament pattern follows the extrusion machine, parallel to one of the axes of the construction plane. In the case of cover (I), the printing pattern of the filament is crossed with 45° raster angle placed in the construction plane. The printed specimens at different orientations are shown in Table 4.2 and 4.3.

The nomenclature, H, Z, YZ and XZ corresponds to the following

H: The sample is printed in the XY plane and placed horizontally (H).

Z: The sample is printed in the XY plane and placed vertically (Z) on the plane aligned with the Z direction.

YZ: The sample is printed with 45° degrees of inclination in YZ plane.

XZ: The sample is printed with 45° degrees of inclination in XZ plane (similar to the YZ case).

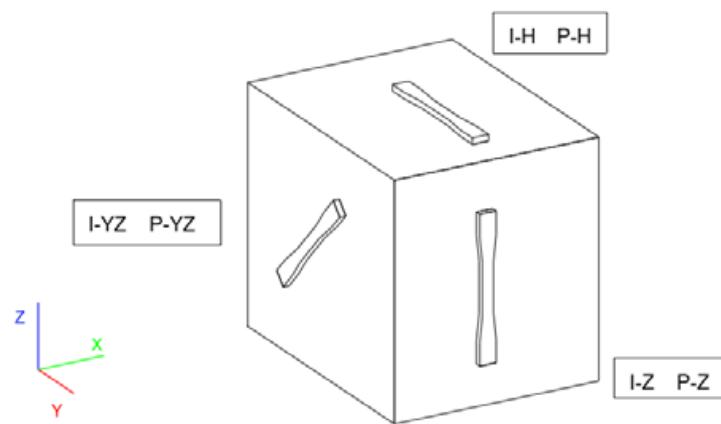


Figure 4.6 Orientations of the dog-bone specimens

Sample	Printing Design
P-H	

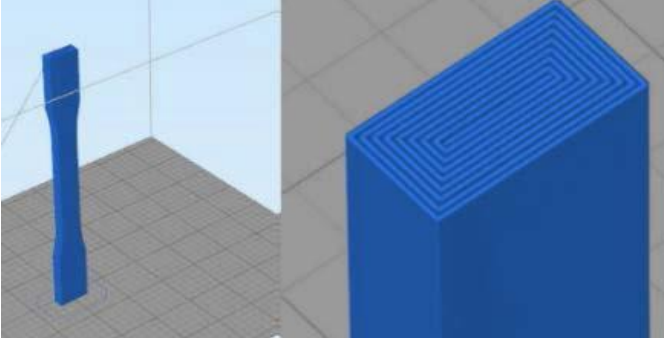
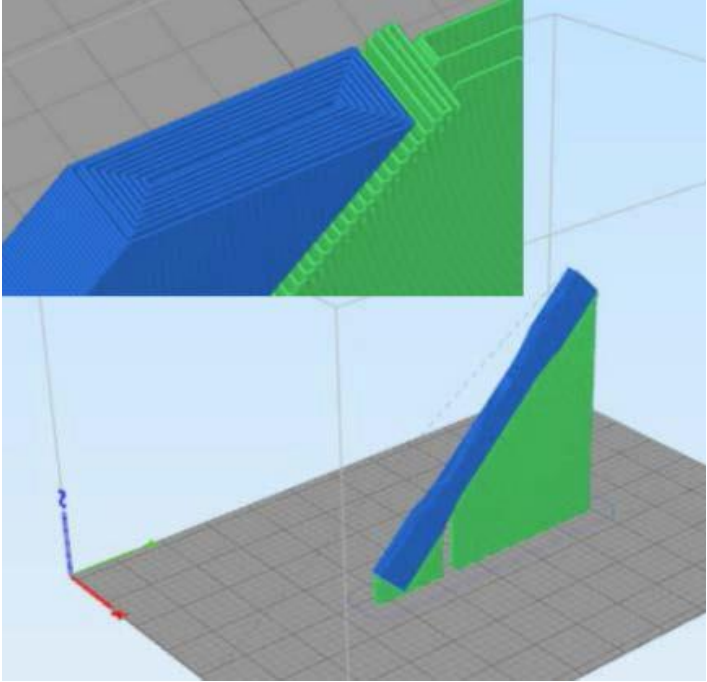

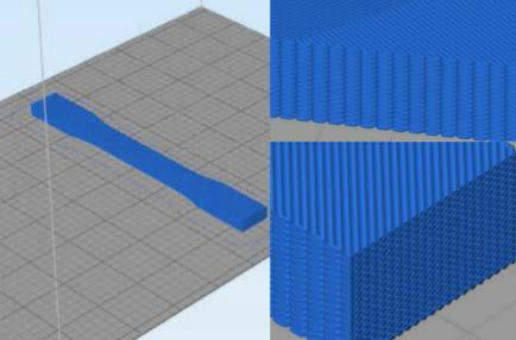
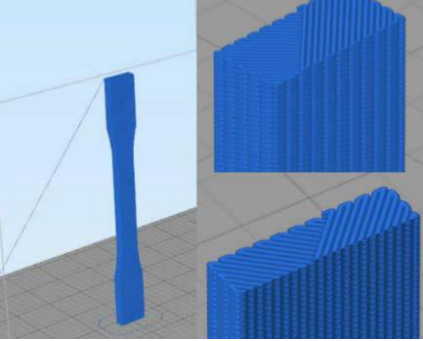
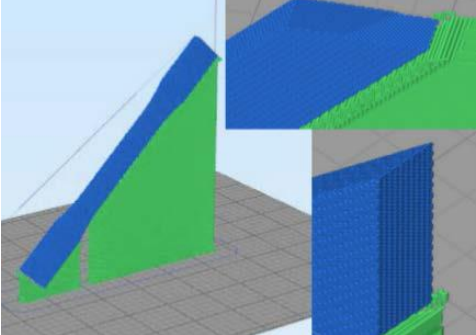
P-Z	
P-YZ	
Experiment	

Table 4.2 P samples (contour)

Sample	Printing Design
I-H	 <p>The image shows two views of a 3D printed part. On the left is a perspective view of a blue rectangular block with a textured surface, resting on a grey grid. On the right is a top-down view showing the internal structure of the block, which consists of a regular grid of small, interconnected rectangular cells.</p>
I-Z	 <p>The image shows two views of a 3D printed part. On the left is a perspective view of a blue rectangular block with a textured surface, resting on a grey grid. On the right is a top-down view showing the internal structure of the block, which consists of a regular grid of small, interconnected rectangular cells.</p>
I-YZ	 <p>The image shows two views of a 3D printed part. On the left is a perspective view of a blue and green rectangular block with a textured surface, resting on a grey grid. On the right is a top-down view showing the internal structure of the block, which consists of a regular grid of small, interconnected rectangular cells.</p>

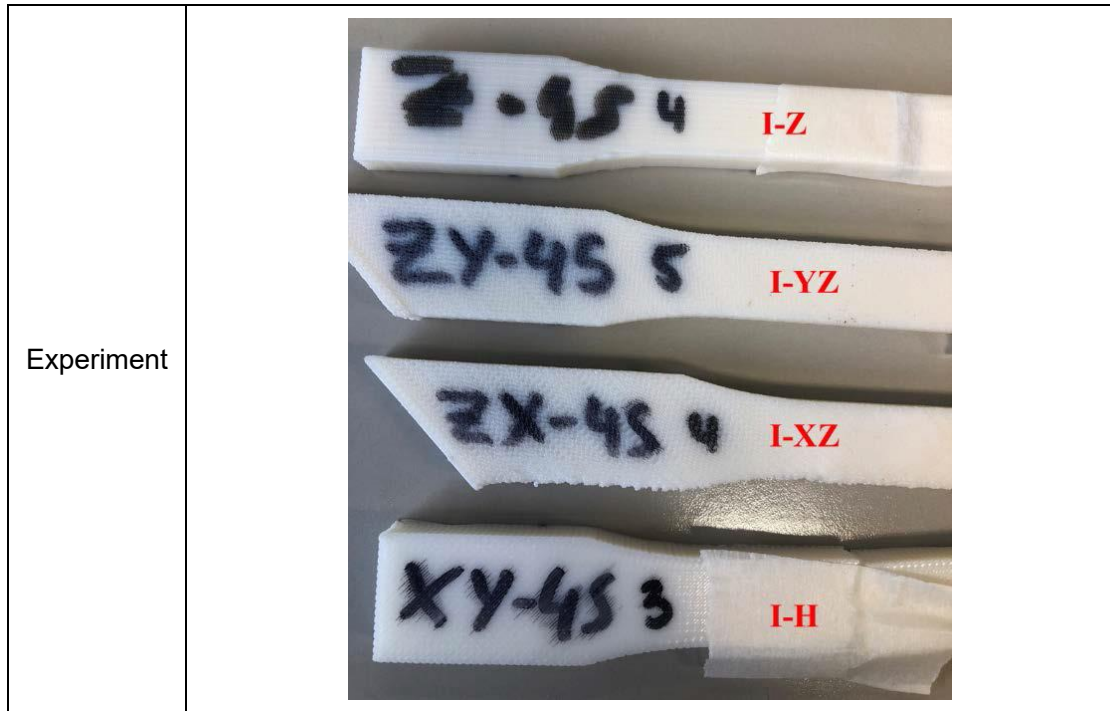


Table 4.3 I samples (contour)

According to the constitutive equation of a linear elastic material, the stiffness tensor \mathbf{C} has to be obtained from the experiment. The inverse of the constitutive tensor is known as the compliance matrix $\mathbf{S} = \mathbf{C}^{-1}$. The experimental tests are defined such that to obtain the transversely isotropic material properties.

Since the model is constructed layer by layer during the FFF process, the material properties can be considered transversely isotropic: the mechanical properties are symmetric in all directions of the transverse plane normal to an anisotropic principal axis along the direction of deposition.

Due to this symmetry presented in 2D, the material properties are reduced from 9 (orthotropic materials) to 5 independent parameters ($E = E_x = E_y, E_z, \nu_{xy}, \nu_{zx}, G = G_{zx} = G_{yz}$). E_i is the Young's modulus on axis i , G_{ij} is the shear modulus in direction j on the plane with normal in direction i , and, ν_{ij} is Poisson's ratio describing the relationship between the transversal deformation in direction j and the axial elongation if the applied loading is in direction i .

In order to obtain the 5 independent material parameters, samples are built with 3 different orientations: horizontal, vertical and 45° inclined.

The cover and the contour material are assumed to be transversely isotropic. If the constructing plane XY is the plane of isotropy, thus an orthotropic compliance matrix is

$$S = \begin{bmatrix} \frac{1}{E} & -\frac{\nu_{xy}}{E} & -\frac{\nu_{zx}}{E_z} & 0 & 0 & 0 \\ -\frac{\nu_{xy}}{E} & \frac{1}{E} & -\frac{\nu_{zx}}{E_z} & 0 & 0 & 0 \\ -\frac{\nu_{zx}}{E_z} & -\frac{\nu_{zx}}{E_z} & \frac{1}{E_z} & 0 & 0 & 0 \\ 0 & 0 & 0 & \frac{2(1+\nu_{xy})}{E} & 0 & 0 \\ 0 & 0 & 0 & 0 & \frac{1}{G} & 0 \\ 0 & 0 & 0 & 0 & 0 & \frac{1}{G} \end{bmatrix} \quad (4.1)$$

According to the reference axes used in the experiment, the following nomenclature is defined for each zone.

Contour:

E_{\parallel} : Young's modulus in the direction parallel to the filament

E_{iso} : Young's modulus in the direction perpendicular to the filament and in the plane of isotropy

ν_{iso} : Poisson's ratio of the plane of isotropy

ν : Poisson's ratio in the direction parallel to the filament

$G_{iso} = \frac{E_{iso}}{2(1+\nu_{iso})}$: Shear modulus of the plane of isotropy

G : Shear modulus in the direction parallel to the filament

Cover:

E_{\perp} : Young's modulus in the direction parallel to the printing direction of the specimen and perpendicular to the plane of isotropy

E_{iso} : Young's modulus in the printing plane (plane of isotropy) with
rectilinear filament pattern

ν_{iso} : Poisson's ratio of the plane of isotropy

ν : Poisson's ratio in the printing direction

$G_{iso} = \frac{E_{iso}}{2(1+\nu_{iso})}$: Shear modulus of the plane of isotropy

G : Shear modulus in the printing direction

According to this nomenclature, the S-tensor for the contour, where its isotropy
plane is YZ as the filament is deposited in the X direction, reads

$$S = \begin{bmatrix} \frac{1}{E_{\parallel}} & -\frac{\nu}{E_{\parallel}} & -\frac{\nu}{E_{\parallel}} & 0 & 0 & 0 \\ -\frac{\nu}{E_{\parallel}} & \frac{1}{E_{iso}} & -\frac{\nu_{iso}}{E_{iso}} & 0 & 0 & 0 \\ -\frac{\nu}{E_{\parallel}} & -\frac{\nu_{iso}}{E_{iso}} & \frac{1}{E_{iso}} & 0 & 0 & 0 \\ 0 & 0 & 0 & \frac{1}{G} & 0 & 0 \\ 0 & 0 & 0 & 0 & \frac{1}{G} & 0 \\ 0 & 0 & 0 & 0 & 0 & \frac{1}{G_{iso}} \end{bmatrix} \quad (4.2)$$

Similarly, the S-tensor for the cover reads

$$S = \begin{bmatrix} \frac{1}{E_{iso}} & -\frac{\nu_{iso}}{E_{iso}} & -\frac{\nu}{E_{\perp}} & 0 & 0 & 0 \\ -\frac{\nu_{iso}}{E_{iso}} & \frac{1}{E_{iso}} & -\frac{\nu}{E_{\perp}} & 0 & 0 & 0 \\ -\frac{\nu}{E_{\perp}} & -\frac{\nu}{E_{\perp}} & \frac{1}{E_{\perp}} & 0 & 0 & 0 \\ 0 & 0 & 0 & \frac{1}{G_{iso}} & 0 & 0 \\ 0 & 0 & 0 & 0 & \frac{1}{G} & 0 \\ 0 & 0 & 0 & 0 & 0 & \frac{1}{G} \end{bmatrix} \quad (4.3)$$

Once the tensors are defined, the parameters are obtained from the
experiments.

4.1.3.1.1.1. Material properties of the contour

Young's modulus in the direction parallel to the filaments ($E_{||}$) is obtained from the horizontally printed P-H specimen. The load is applied in the direction of the filaments. (see Figure 4.7)

$$E_{||} = \frac{\sigma_{xx}}{\varepsilon_{xx}} \quad (4.4)$$

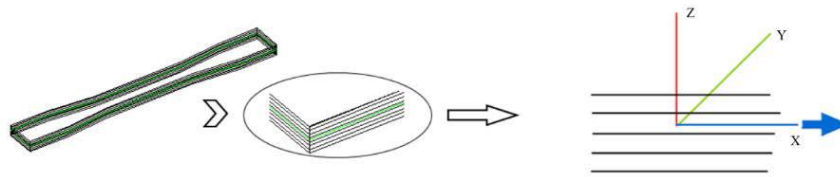


Figure 4.7 Obtaining Young's Modulus Parallel to the deposition of the contour material

Following what we talk in the previous content, Poisson's ratio ν could be obtained by performing a Digital Image Correlation (DIC) test on the P-Z specimens. The force is applied perpendicular to the direction of the filament and the deformation is measured in the direction perpendicular and parallel to the filament. In this work, we did not do this test.

To obtain Poisson's ratio ν_{iso} , a specimen should be tested with the applied force in one of the isotropic axes (Figure 4.8). The deformation is measured in both isotropic axes. In this case, the isotropic Poisson's ratio is equal to the anisotropic Poisson's ratio. Alternatively, $\nu_{iso} = \nu$ can be assumed.

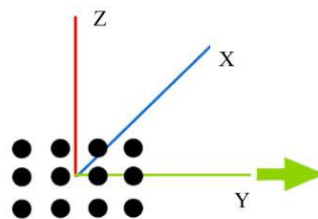


Figure 4.8 Scheme of load application to obtain the Poisson's ratio of the isotropy plane for the contour material

The shear modulus G is obtained from uniaxial tensile test of specimen printed in 45° , in this case P-YZ.

$$G = \frac{E_1}{2(1 + \nu_{12})} \Big|_{YZ} \quad (4.5)$$

Where 1 is the direction of the applied load and 2 is the direction perpendicular to 1.

4.1.3.1.1.2. Material properties of the cover

Young's modulus in the direction parallel to the construction direction (E_\perp) is obtained from the I-Z specimen. The load is applied in the construction direction. (see Figure 4.9)

$$E_\perp = \frac{\sigma_{zz}}{\varepsilon_{zz}} \quad (4.6)$$

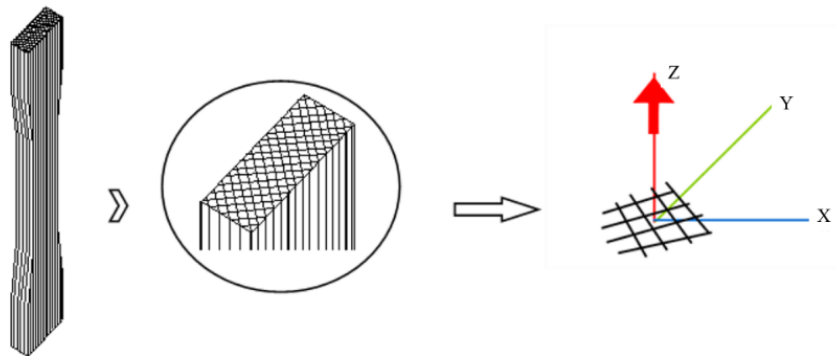


Figure 4.9 Obtaining Young's modulus in the construction direction for the cover material

E_{iso} is the elasticity modulus obtained from carrying out a tensile test in the isotropic plane. The tensile force is applied in one of the isotropic directions and its corresponding modulus is measured. In this case I-H specimens are used (see Figure 4.10)

$$E_{iso} = \frac{\sigma_{xx}}{\varepsilon_{xx}} \quad (4.7)$$

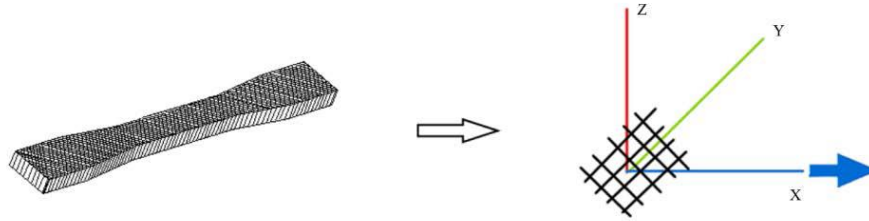


Figure 4.10 Obtaining isotropic Young's Modulus for the cover material

Again, due to we did not do the DIC test, here we only explain why we take the assume $\nu_{iso} = \nu$. The mainly reason is that ν_{iso} , the Poisson's ratio in isotropic plane is hard to obtain from the experimental test. In this report, ν_{iso} and ν are both from reference material but not from DIC experiment.

G_{iso} is known through the relationship with E_{iso} and ν_{iso} . However, the shear modulus G is obtained from a uniaxial tensile test of a specimen printed in 45° , in this case I-YZ.

Figures 4.11 and 4.12 summarize how each parameter is obtained from the dog-bone specimens uniaxial tests to characterize the material properties of contour and cover, respectively.

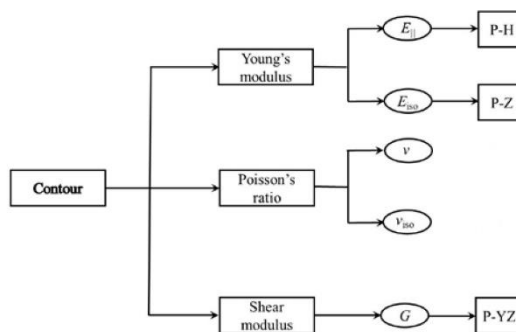


Figure 4.11 Diagram for obtaining the parameters from the tests (contour material)

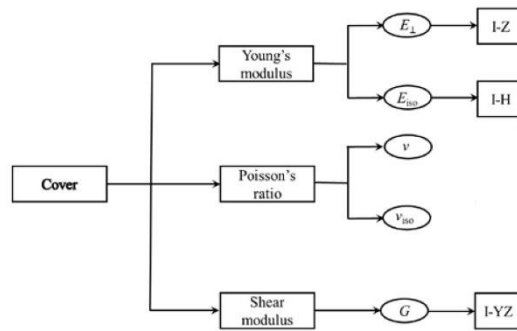


Figure 4.12 Diagram for obtaining the parameters from the tests (cover material)

From the experimental results and the strategy mentioned above, the transversely isotropic properties of the contour and cover are obtained and presented in Table 4.4.

Material Properties		Contour	Cover
E_{\parallel} [GPa]	E_{\perp} [GPa]	1.86	1.53
E_{iso} [GPa]		1.51	1.51
ν_{iso}		0.35	0.35
ν		0.35	0.35
G [GPa]		0.56	0.23
G_{iso} [GPa]		0.56	0.56

Table 4.4 Material properties of contour and cover of PC-ABS 3D in the model

The specimens printed with aligned filaments (contour) show a distinct mechanical response from those made by 100% crossed filaments (cover) and from the raw material. Young's moduli of contour and cover are around 30% ($E_{\parallel,contour}$) to 45% ($E_{iso,contour}$), 45% ($E_{\perp,contour}$) and 45% ($E_{iso,contour}$) lower than that of the raw material, respectively. These differences are due to the effect of the printing pattern as well as the influence of the intra/inter-layer bonds that play a crucial role in FFF components.

Moreover, it can be seen that the fabricated specimens with aligned filaments are stiffer than those made of crossed filaments acting as a reinforcement in the direction of fibers. Therefore, the proposal to distinguish between the material properties of the contour and the cover in order to analyze the performance of FFF components is experimentally justified.

From the experimental results, following relationship between the properties of the isotropic raw material and the printed ones is derived:

$$E_{\parallel,contour} \approx 69\%E_{Raw}(E_{Raw} = 2.7GPa)$$

$$G_{iso,contour} \approx 56\%G_{Raw}(G_{Raw} = \frac{E_{Raw}}{2(1+\nu)} = 1.0GPa)$$

$$E_{iso,contour} \approx 81\%E_{\parallel,contour}$$

$$E_{iso,cover} \approx 81\%E_{\parallel,contour}$$

$$E_{\perp,cover} \approx 101\%E_{iso,contour}$$

These relationships can be considered for the analysis of FFF components when the experimental campaign for the material characterization according to the printing pattern is to be avoided.

4.1.3.1.2. Computational characterization of the in-fill

Representing the shape details of the heterogeneous in-fill structure within the geometrical model would result in an excessive computational cost of the corresponding simulation (Figure 4.1). Therefore, instead of including these details explicitly, a computational homogenization technique is used here. The in-fill structure is modelled as a homogeneous medium with an equivalent constitutive behavior [32]. It is convenient to use RVE-based homogenization [40-42] since the heterogeneities in the in-fill present periodicity over the domain and the structure is characterized by the repetition of a unit cell [43].

4.1.3.2. Validation: test on samples with square cross-section

The proposed model for the performance analysis of FFF components through separating the mechanical behavior of the contour, the cover and the in-fill is now validated.

In this section, the validation procedure includes the experimental determination of the respective material properties of the contour and the cover and the computational characterization of the in-fill material. For this reason, samples with

square cross-section subjected to bending load are designed and printed. Additionally, the effect of the printing orientation and raster to raster air gap on the final structural behavior is studied.

4.1.3.2.1. Experimental validation

These tests are performed in accordance with the ASTM 790 standard test methods for flexural properties of unreinforced and reinforced plastics and electrical insulating materials. The components are built with a cross-section of 20 mm in width and 20 mm in depth (Figure 4.13). The total length of the specimens is 150 mm, with a span between supports of 120 mm. The contour and the cover have 1 mm thickness (Figure 4.13). The in-fill indicated with green colour is printed with a 45° rectilinear pattern and the specified density

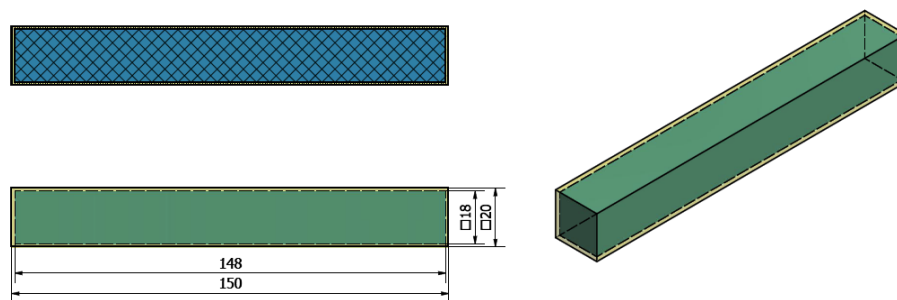


Figure 4.13 Geometry of square cross-section demonstrator (dimensions in mm)

Twenty-seven FFF samples of PC-ABS 3D material are produced with different infill densities (10%, 20% and 50%) and printing orientations:

H samples are manufactured horizontally and supported in the building face.

V samples are manufactured vertically.

The following figure shows the printed samples at different orientations. A cross section of the V sample with 10%, 20% and 50% in-fill densities are shown in Figure 3.15.

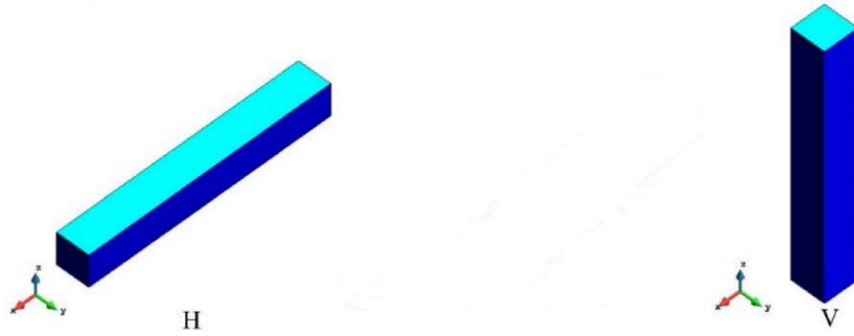


Figure 4.14 Samples with square cross-section printed at different orientations: H and V

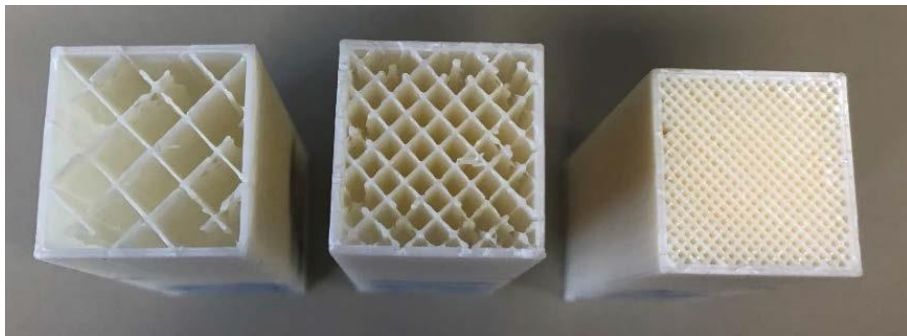


Figure 4.15 Cross-section of the V sample with 10%, 20% and 50% in-fill density (left to right)

A displacement rate of 1.2 mm/min for load application is selected. The yield point is evaluated following the offset method for determining yield strength with an offset value of 0.1%. The experimental setup is shown in Figure 4.16 for sample H with 10% in-fill density.

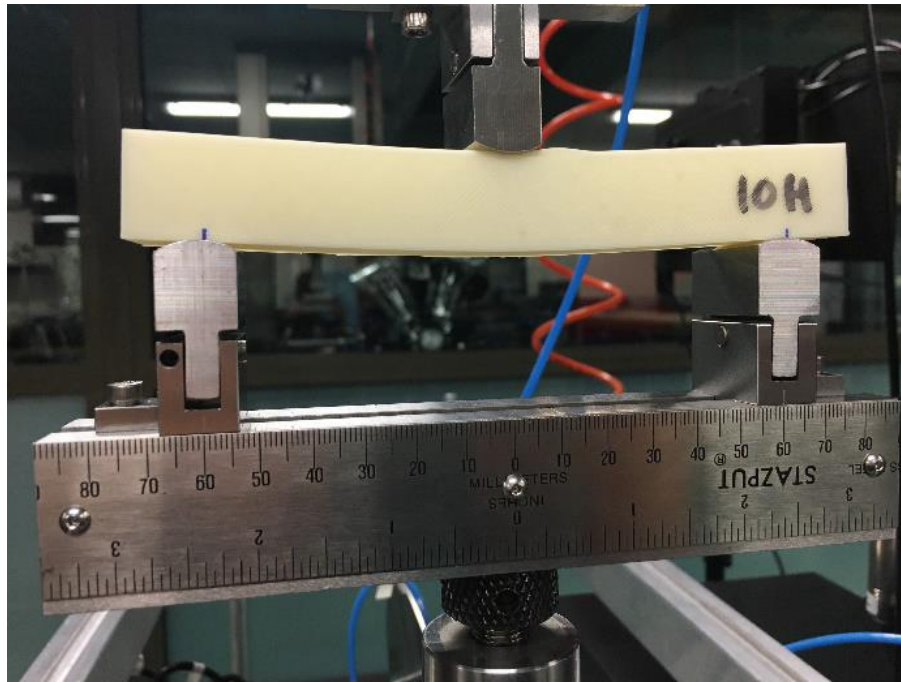


Figure 4.16 Experimental setting and the load position (square cross-section demonstrator)

The corresponding stress-strain curve for each specimen obtained from the test is shown in Figure 4.17. The curves alter in stiffness, maximum load and material failure depending on the printing and testing direction.

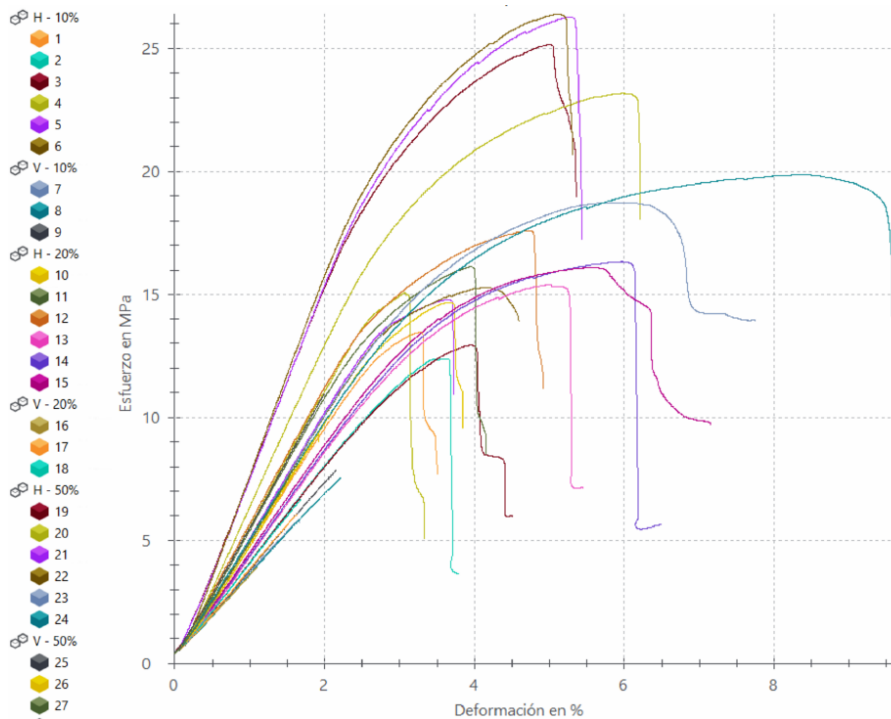


Figure 4.17 Flexural test plot (square cross-section samples)

4.1.3.2.2. Computational modeling

In the computational modelling, the geometry manufactured in a 3D printer with FFF technique is split into four regions corresponding to each printing pattern.

The simulation is performed under the same condition as the experiment (Figure 4.18). The numerical model combines the use of the several software modules. Kratos [44], an in-house multi-physics software, characterizes the in-fill structures by homogenization techniques via RVE with application of PBC. The RVE of the inner structure is shown in Figure 4.19. Comet [45], an in-house software, analyses the overall structural behavior of FFF built components.

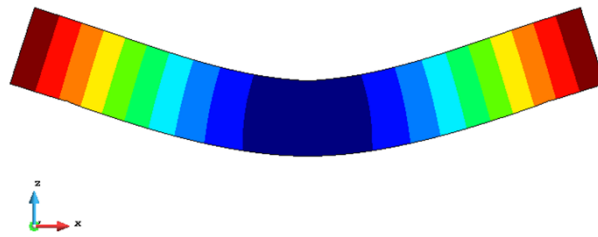


Figure 4.18 Simulated deformation of the square cross-section sample

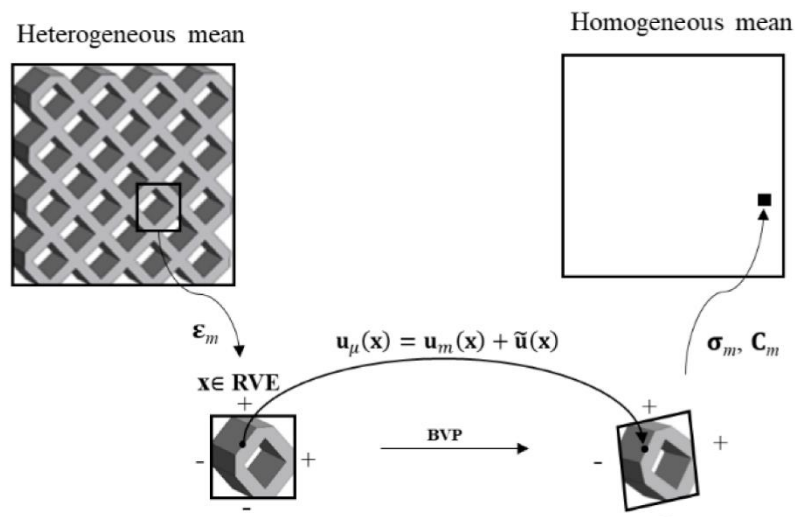


Figure 4.19 Homogenization strategy and PBC on the boundary of RVE

The material properties of cover and contour characterized in the previous section are assigned to the corresponding volumes. The material properties of the in-fill obtained by the computational homogenization technique is shown in Table 4.5.

The mechanical properties of the in-fill reflect the percentage of air gap between the filaments as well as their orientations. Specially, for the numerical simulation, 60% density infill is introduced to compare with the result of 50% density infill.

Properties	infill 10%	infill 20%	infill 50%	infill 60%	Units
E_x	0.607548183	5.472167657	129.9935317	260.1812763	MPa
E_y	0.607608885	5.472243205	130.0220057	260.2707503	MPa
E_z	186.0001815	371.9999586	930.0001891	1116.000821	MPa
G_{xy}	53.32628983	106.9813997	274.1080691	333.8328218	MPa
G_{yz}	35.84035319	74.82683741	219.4334908	281.7042376	MPa
G_{xz}	35.84039644	74.8273647	219.4265821	281.6973128	MPa
ν_{xy}	0.993790877	0.973891764	0.802237645	0.700766773	
ν_{zy}	0.352825349	0.352997409	0.353010983	0.35300044	
ν_{zx}	0.353174254	0.353002712	0.352989986	0.35299967	

Table 4.5 In-fill material properties (square cross-section sample)

For each configuration, defined according to the printing design parameters, Table 4.6 presents the relative error between the stiffness obtained from the experimental tests $K_{experimental}$ and the one obtained from the mechanical simulation $K_{simulation}$. The experimental stiffness is obtained through the linear relationship between the applied displacement and the resulting force. The computational stiffness is obtained through the same linear relationship between the applied force and the resulting displacement. Remarkable agreements are seen between the experimental and numerical results. The simulation results are compared with respect to an average value as the experimental data are very dispersed in horizontal cases. The simulation result is within the experimental results domain which is shown in grey color area in figure 4.20. The experimental results of the vertical specimens are concentrated and the simulation results present accurate behavior.

Figure 4.20 compares the numerical and the experimental force vs. displacement graphs for all the combination of infill densities. The agreement between the numerical and experimental results for all the cases is noteworthy.

In-fill density	Specimen type	Displacement_ experimental	Displacement_ simulation	K_ experimental	K_ simulation	Relative error
(%)		(mm)	(mm)	(N/mm)	(N/mm)	(%)
10	H	3.28236	3.35036	164.5157752	161.1767094	2.029632636
	V	1.8876	1.856078	133.5028608	135.7701562	1.669951261
20	H	4.24452	3.658302	152.6674394	177.1313577	13.81117299
	V	1.18788	1.116335	141.4284271	150.4924597	6.022914773
50	H	4.34004	3.752219	190.7816518	220.6694225	13.54413784
	V	1.83672	1.90728	189.4681824	182.4587895	3.699509249
60	H	4.34004	3.315861	190.7816518	249.7088991	23.59837697
	V	1.83672	1.828144	189.4681824	190.3569959	0.466919291

Table 4.6 Mechanical response of the square cross-section sample and the relative error according to each orientation and printing parameters

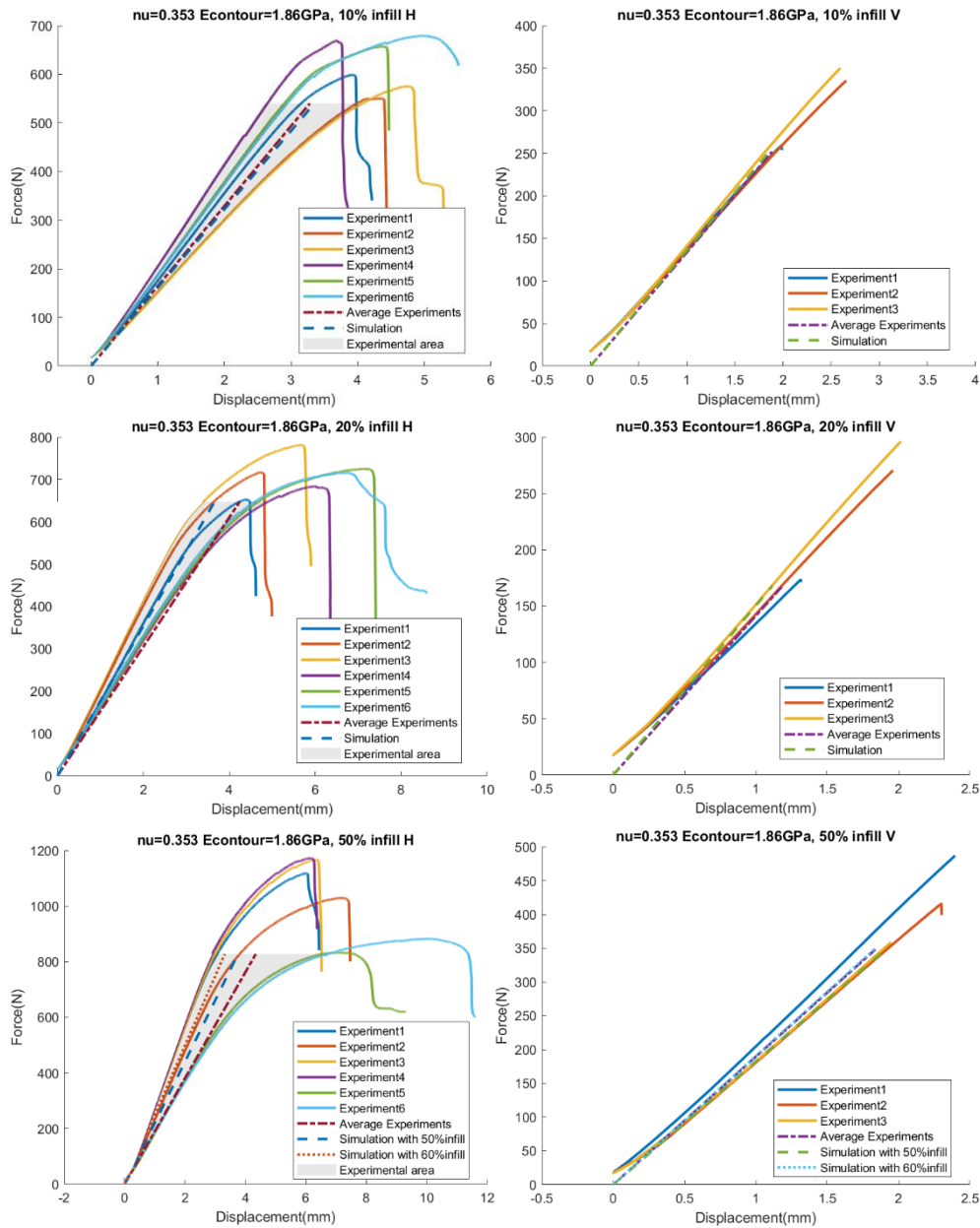


Figure 4.20 Force [N] vs. displacement [mm] curves comparing the simulation results with the experimental measurements

4.1.4. Conclusion

From this, it is concluded that characterizing the material behavior of the component according to the printing pattern is necessary for the correct prediction of the mechanical performance. Moreover, the transversely isotropic description of the contour and the cover materials plus the use of homogenization technique

for characterization of the in-fill material represent accurately the behavior of the samples.

Moreover, the mechanical performance of these samples is affected by the in-fill density and orientation.

Increasing the in-fill density increases the stiffness of the structure. In particular, the vertically printed samples (V specimens) are the most influenced by the increment of the in-fill density.

4.2. Case2 Electric box

4.2.1. Introduction

This case mainly discusses an electric box manufactured by FFF. PC-ABS are considered as the material of the box. Analyzing the mechanical performance under the load given is the major goal in this case. Due to “warping” (thermal expansion), it was only possible to print with ELIX PC-ABS 3D at a scale of 50%. (See Figure 4.21).



Figure 4.21 The 50% fabricated electric box with PC-ABS

4.2.2. Methodology

Using Comet to analyze this case, the Von-mises stress and displacements in six load cases are evaluated to access the performance of the structure. Specially,

there is no infill or lattice in the geometry. The top and bottom material are considered as transverse isotropic material by the $\pm 45^\circ$ filament while the four walls material are considered as transverse isotropic material by aligned filament. In the other words, the cover is assigned in the top and bottom surfaces while the contour is assigned in the four vertical surfaces (walls) of the box. All the left contours of the assembly geometry are simplified as isotropic material due to the printing orientation of these geometries are variable (See the yellow color of Figure 4.22).

4.2.3. Result

4.2.3.1. Data

Input properties of PC-ABS is given on the Table 4.4. XY plane is the printing bed, the construction path of AM product is from bottom to top along Z direction.

4.2.3.1.1. Top and Bottom surface property

Properties	Results	Units	Equal to Table 4.4
E_z	1.53	GPa	E_{\perp}
E	1.51	GPa	E_{iso}
ν_{yx}	0.353		ν_{iso}
ν	0.353		ν
G	0.23	GPa	G
G_{xy}	0.56	GPa	G_{iso}

Table 4.7 Properties of Top and Bottom, Printing direction in Z

The compliance tensor of cover

$$S = \begin{bmatrix} \frac{1}{E_x} & -\frac{\nu_{yx}}{E_y} & -\frac{\nu_{zx}}{E_z} & 0 & 0 & 0 \\ -\frac{\nu_{xy}}{E_x} & \frac{1}{E_y} & -\frac{\nu_{zy}}{E_z} & 0 & 0 & 0 \\ -\frac{\nu_{xz}}{E_x} & -\frac{\nu_{yz}}{E_y} & \frac{1}{E_z} & 0 & 0 & 0 \\ 0 & 0 & 0 & \frac{1}{G_{xy}} & 0 & 0 \\ 0 & 0 & 0 & 0 & \frac{1}{G_{zx}} & 0 \\ 0 & 0 & 0 & 0 & 0 & \frac{1}{G_{yz}} \end{bmatrix} = C^{-1} \quad (4.8)$$

Where $E_x = E_y = E$, $G_{zx} = G_{yz} = G$, $\nu_{zx} = \nu_{zy} = \nu$, $\nu_{yx} = \nu_{xy} = \nu_{iso}$.

Then, yield

$$S = \begin{bmatrix} \frac{1}{E} & -\frac{\nu_{yx}}{E} & -\frac{\nu}{E_z} & 0 & 0 & 0 \\ -\frac{\nu_{yx}}{E} & \frac{1}{E} & -\frac{\nu}{E_z} & 0 & 0 & 0 \\ -\frac{\nu}{E_z} & -\frac{\nu}{E_z} & \frac{1}{E_z} & 0 & 0 & 0 \\ 0 & 0 & 0 & \frac{1}{G_{xy}} & 0 & 0 \\ 0 & 0 & 0 & 0 & \frac{1}{G} & 0 \\ 0 & 0 & 0 & 0 & 0 & \frac{1}{G} \end{bmatrix} = C^{-1} \quad (4.9)$$

The constitutive tensor

$$C = S^{-1} = \begin{bmatrix} 2,440,625,609 & 1,324,587,176 & 1,329,120,113 & 0 & 0 & 0 \\ 1,324,587,176 & 2,440,625,609 & 1,329,120,113 & 0 & 0 & 0 \\ 1,329,120,113 & 1,329,120,113 & 2,468,358,800 & 0 & 0 & 0 \\ 0 & 0 & 0 & 558,019,217 & 0 & 0 \\ 0 & 0 & 0 & 0 & 232,815,965 & 0 \\ 0 & 0 & 0 & 0 & 0 & 232,815,965 \end{bmatrix} \quad (4.10)$$

4.2.3.1.2. Irregular contour property

Properties	Results	Units	Equal to Table 4.4
E	1.86	GPa	$E_{ }$
ν	0.353		ν

Table 4.8 Properties of Irregular contour

Due to the variable printing direction of the irregular contour, the property is simplified as isotropy.

4.2.3.1.3. Wall in YZ plane property

Properties	Results	Units	Equal to Table 4.4
E_y	1.86	GPa	E_{\parallel}
E	1.51	GPa	E_{iso}
ν_{zx}	0.353		ν_{iso}
ν	0.353		ν
G	0.56	GPa	G
G_{zx}	0.56	GPa	G_{iso}

Table 4.9 Properties of wall in YZ plane, filament direction in Y

Wall in YZ plane, Compliance tensor according Eq.4.8:

$$S = \begin{bmatrix} \frac{1}{E} & -\frac{\nu}{E_y} & -\frac{\nu_{zx}}{E} & 0 & 0 & 0 \\ -\frac{\nu}{E_y} & \frac{1}{E_y} & -\frac{\nu}{E_y} & 0 & 0 & 0 \\ -\frac{\nu_{zx}}{E} & -\frac{\nu}{E_y} & \frac{1}{E} & 0 & 0 & 0 \\ 0 & 0 & 0 & \frac{1}{G} & 0 & 0 \\ 0 & 0 & 0 & 0 & \frac{1}{G_{zx}} & 0 \\ 0 & 0 & 0 & 0 & 0 & \frac{1}{G} \end{bmatrix} = C^{-1} \quad (4.11)$$

Where take the substitution,

$$E_x = E_z = E, G_{xy} = G_{yz} = G, \nu_{yx} = \nu_{yz} = \nu, \nu_{zx} = \nu_{xz} = \nu_{iso}.$$

Wall in YZ plane, constitutive tensor:

$$C = S^{-1} = \begin{bmatrix} 2,255,877,526 & 1,198,687,966 & 1,139,839,093 & 0 & 0 & 0 \\ 1,198,687,966 & 2,706,273,704 & 1,198,687,966 & 0 & 0 & 0 \\ 1,139,839,093 & 1,198,687,966 & 2,255,877,526 & 0 & 0 & 0 \\ 0 & 0 & 0 & 561,714,708 & 0 & 0 \\ 0 & 0 & 0 & 0 & 558,019,217 & 0 \\ 0 & 0 & 0 & 0 & 0 & 561,714,708 \end{bmatrix} \quad (4.12)$$

4.2.3.1.4. Wall in XZ plane property

Properties	Results	Units	Equal to Table 4.4
E_x	1.86	GPa	E_{\parallel}
E	1.51	GPa	E_{iso}
ν_{yz}	0.353		ν_{iso}
ν	0.353		ν
G	0.56	GPa	G
G_{yz}	0.56	GPa	G_{iso}

Table 4.10 Properties of wall in XZ plane, filament direction in X

Wall in XZ plane, Compliance tensor according Eq.4.8:

$$S = \begin{bmatrix} \frac{1}{E_x} & -\frac{\nu}{E_x} & -\frac{\nu}{E_x} & 0 & 0 & 0 \\ -\frac{\nu}{E_x} & \frac{1}{E} & -\frac{\nu_{yz}}{E} & 0 & 0 & 0 \\ -\frac{\nu}{E_x} & -\frac{\nu_{yz}}{E} & \frac{1}{E} & 0 & 0 & 0 \\ 0 & 0 & 0 & \frac{1}{G} & 0 & 0 \\ 0 & 0 & 0 & 0 & \frac{1}{G} & 0 \\ 0 & 0 & 0 & 0 & 0 & \frac{1}{G_{yz}} \end{bmatrix} = C^{-1} \quad (4.13)$$

Where take the substitution,

$$E_y = E_z = E, G_{xy} = G_{zx} = G, \nu_{xy} = \nu_{xz} = \nu, \nu_{yz} = \nu_{zy} = \nu_{iso}$$

Wall in XZ plane, constitutive tensor:

$$= \begin{bmatrix} 2,706,273,704 & 1,198,687,966 & 1,198,687,966 & 0 & 0 & 0 \\ 1,198,687,966 & 2,255,877,526 & 1,139,839,093 & 0 & 0 & 0 \\ 1,198,687,966 & 1,139,839,093 & 2,255,877,526 & 0 & 0 & 0 \\ 0 & 0 & 0 & 561714708 & 0 & 0 \\ 0 & 0 & 0 & 0 & 561714708 & 0 \\ 0 & 0 & 0 & 0 & 0 & 558,019,217 \end{bmatrix} \quad C = S^{-1} \quad (4.14)$$

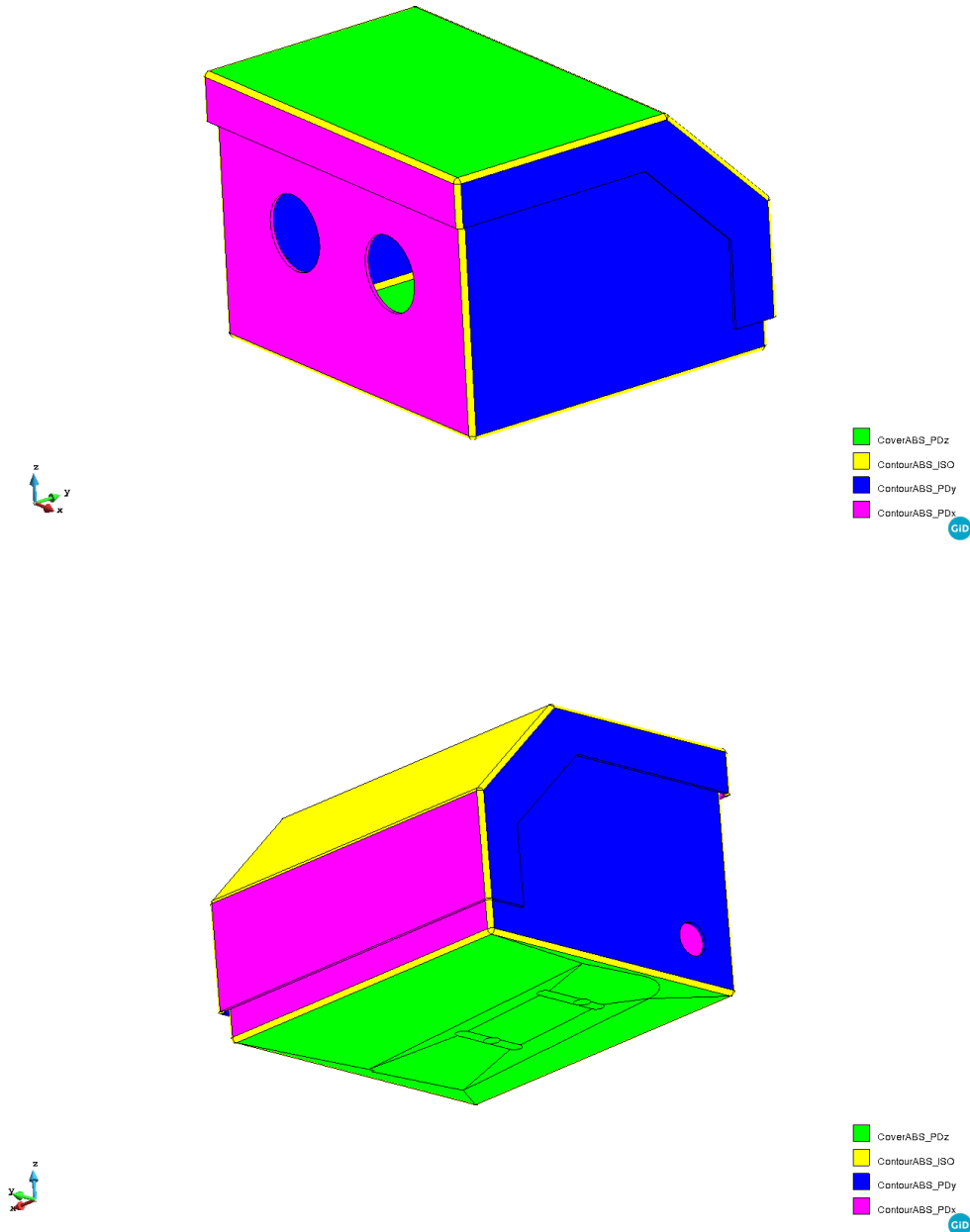


Figure 4.22 Properties of PC-ABS distribution

4.2.3.2. Geometry

This model is simplified as the following. The top cover and the box body constitutes an assembly geometry. The details of the support are neglected.

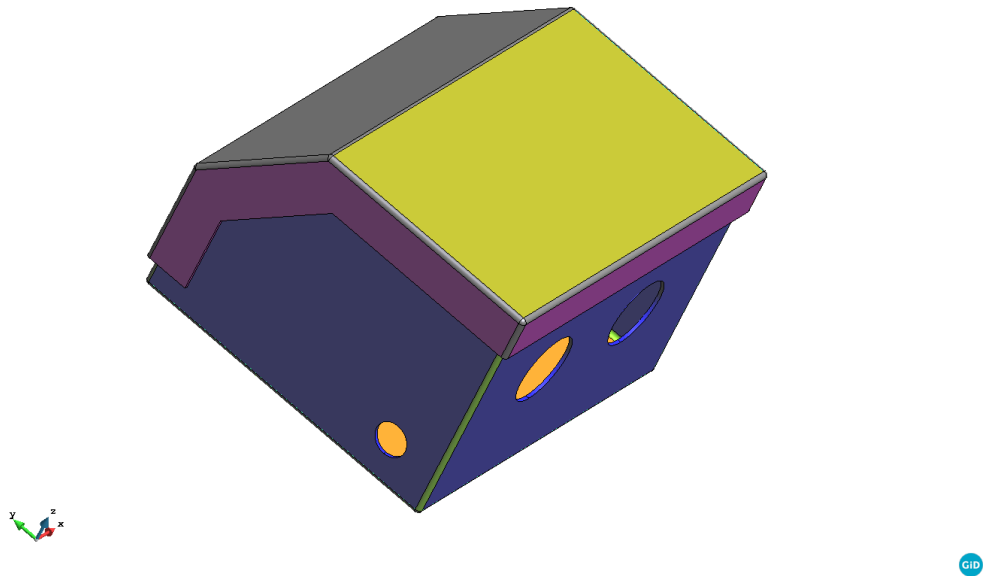


Figure 4.23 Full geometry

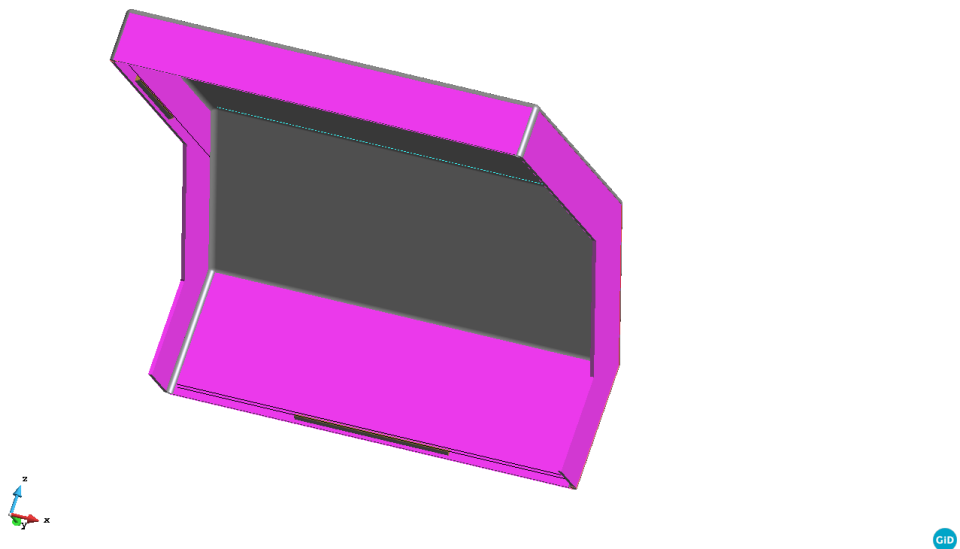


Figure 4.24 Cover geometry

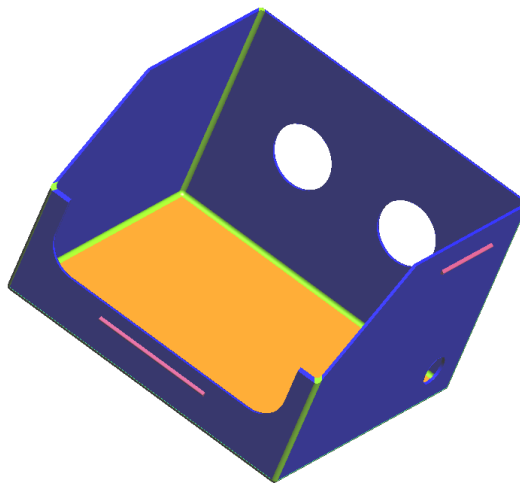


Figure 4.25 Box body geometry

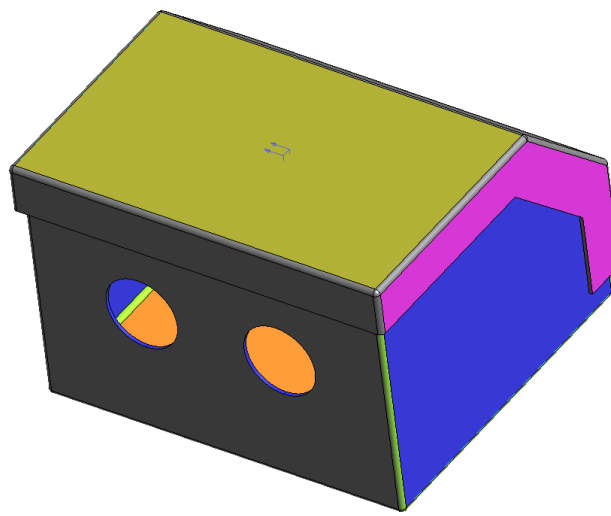
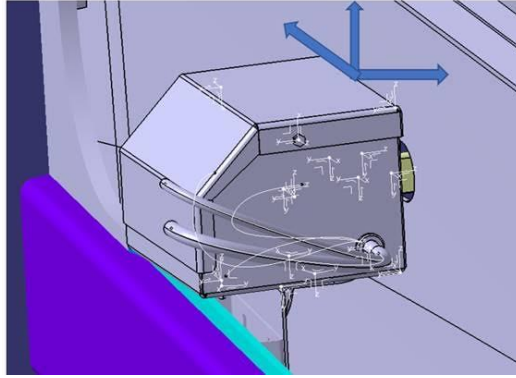
4.2.3.3. Loads and boundary conditions

4.2.3.3.1. Loads

Six loading cases work on the box which are $\pm 15\text{kg}$ forces in X, Y, and Z coordinate applied on the top surface of the cover. Then, the uniform force work on the 15248mm^2 surface. The pressure value is 9641Pa . In this work, the six case are defined as:

Case No.	Load direction
1	+X
2	+Y
3	+Z
4	-X
5	-Y
6	-Z

Table 4.11 Loads direction on the six cases



GID

Figure 4.26 Loads on Cases

4.2.3.3.2. Constrains

This assembly is supported by a support and fixed by screws. Therefore, we fix all displacements on the screws surfaces and limit the vertical displacement on the support surface.

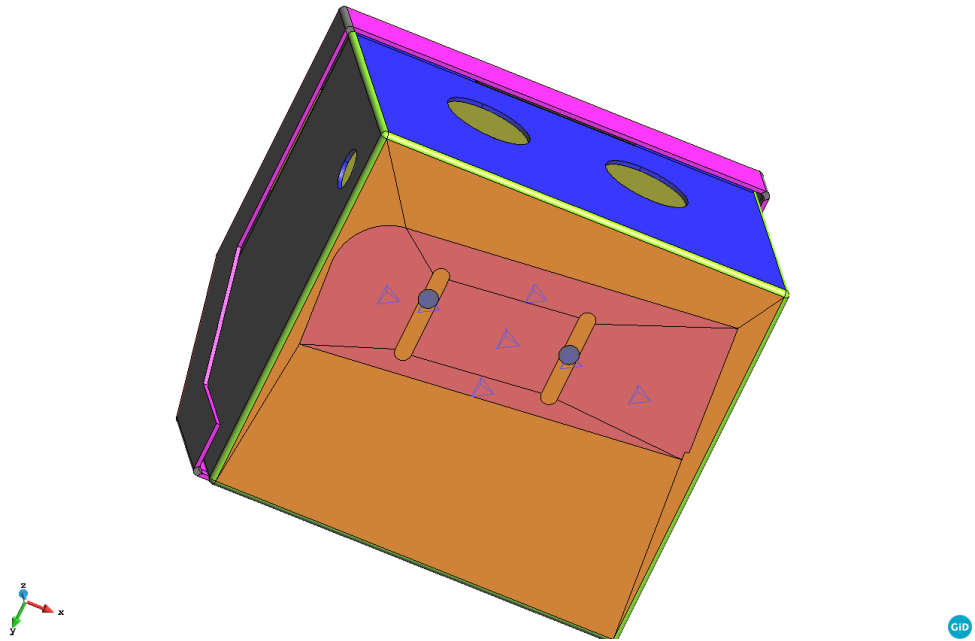


Figure 4.27 Constrains

4.2.3.4. Mesh

This geometry is discretized by 1,700,000 elements. The maximum meshing size is 1mm.

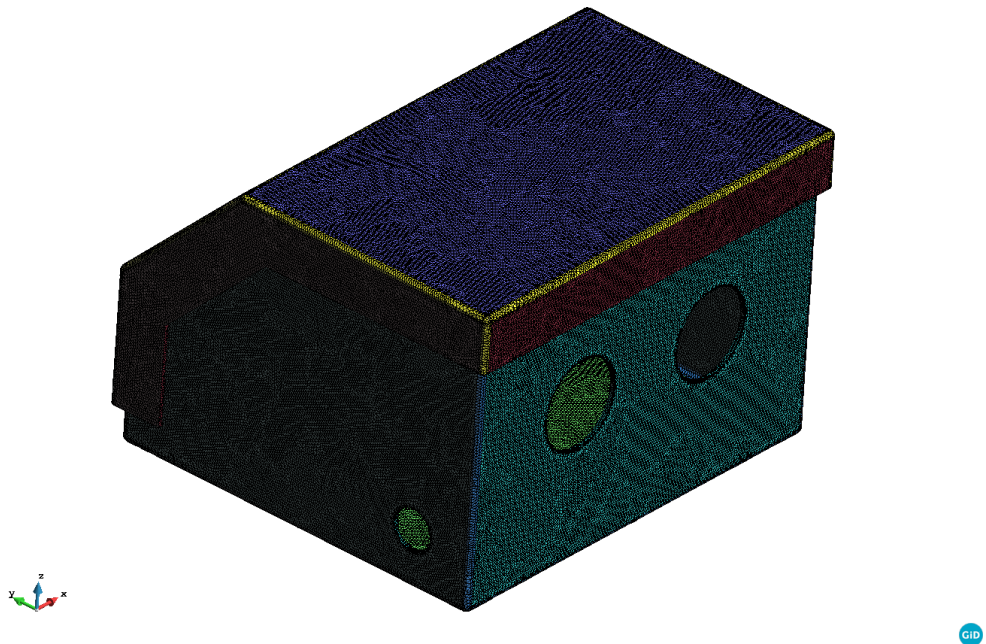
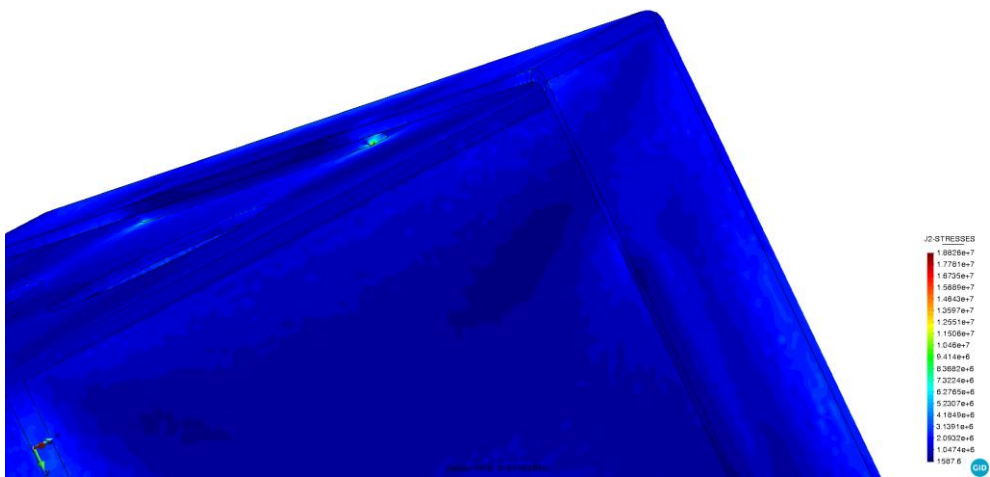
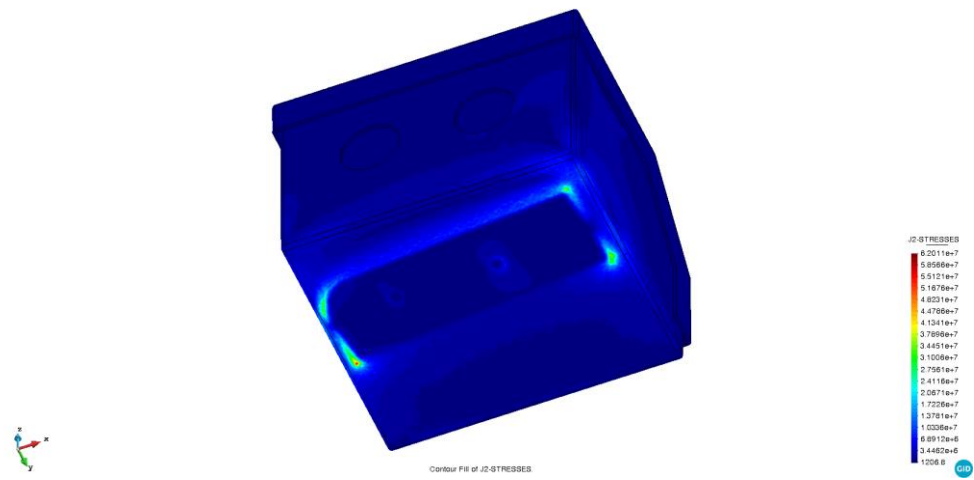
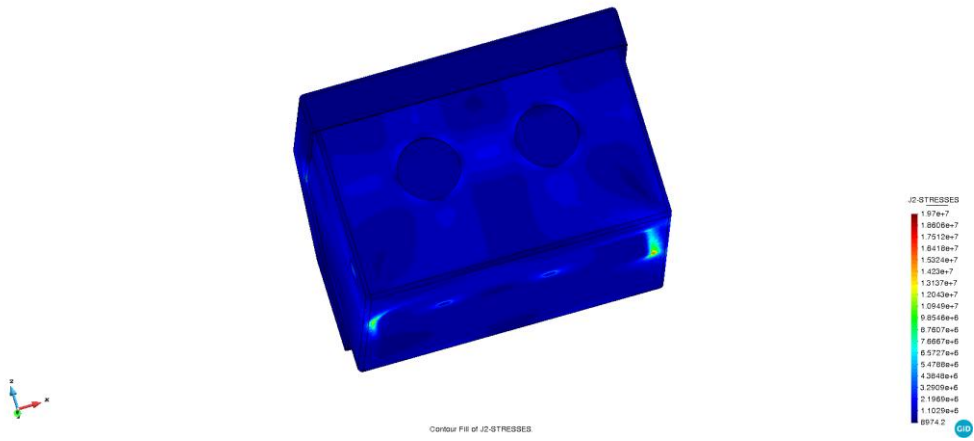


Figure 4.28 Full Mesh

4.2.3.5. Results and conclusion



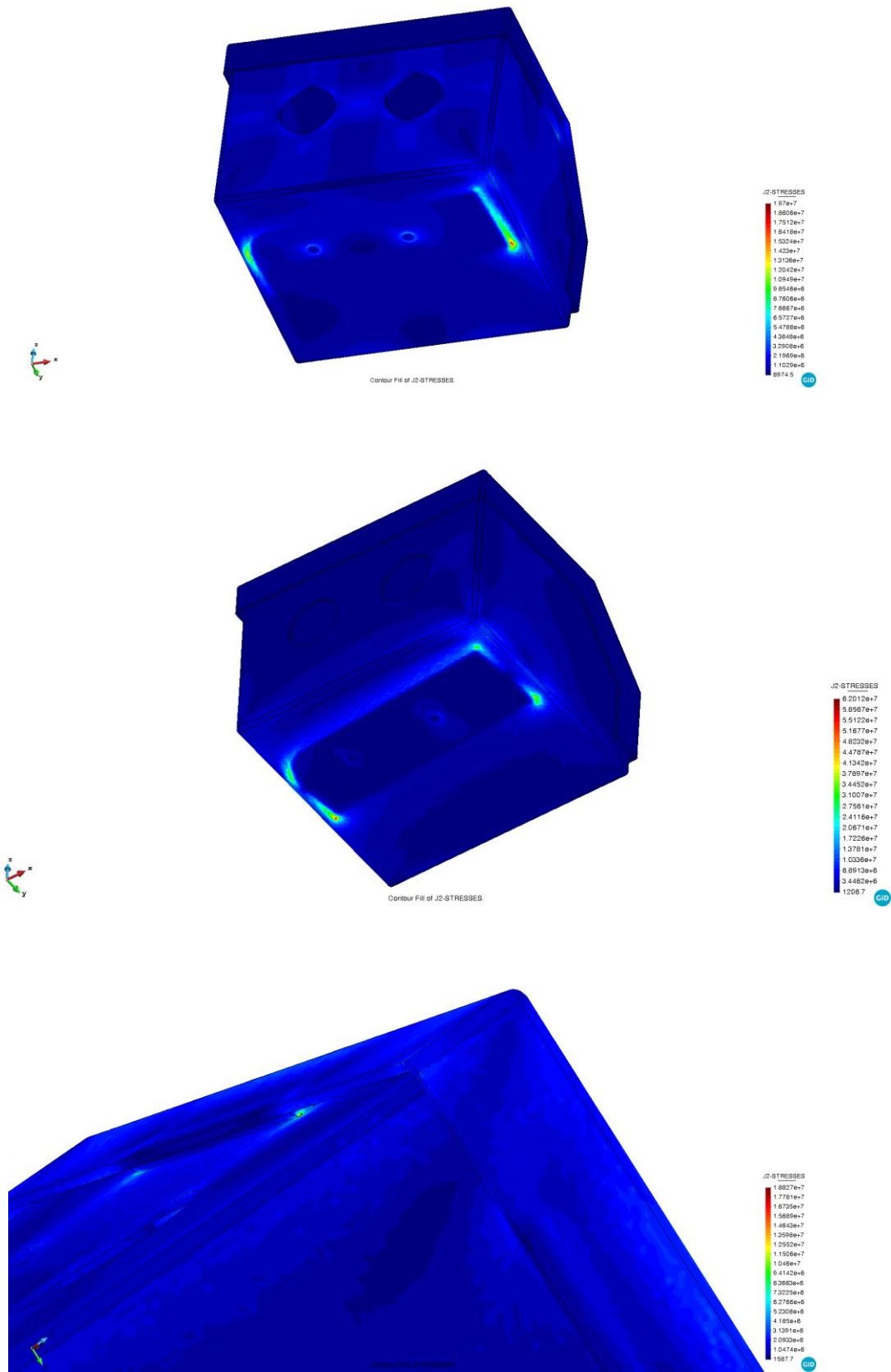
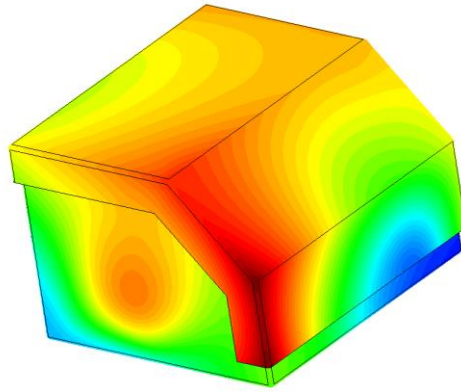
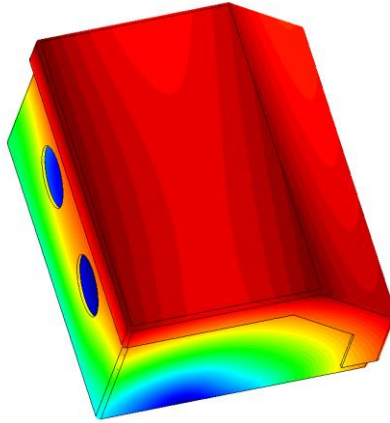
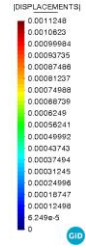


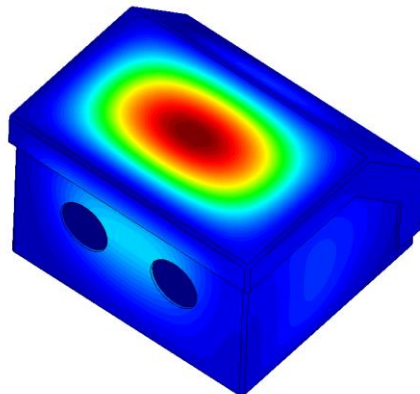
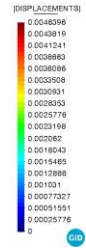
Figure 4.29 Von-mises stress in 6 cases from No.1-6



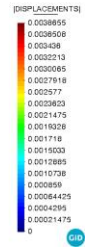
Contour Fill of DISPLACEMENTS, [DISPLACEMENTS]



Contour Fill of DISPLACEMENTS, [DISPLACEMENTS]



Contour Fill of DISPLACEMENTS, [DISPLACEMENTS]



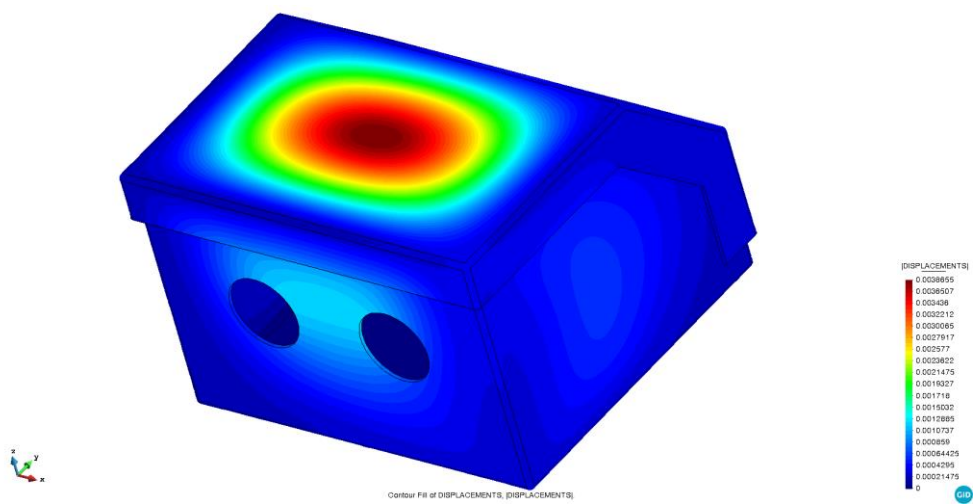
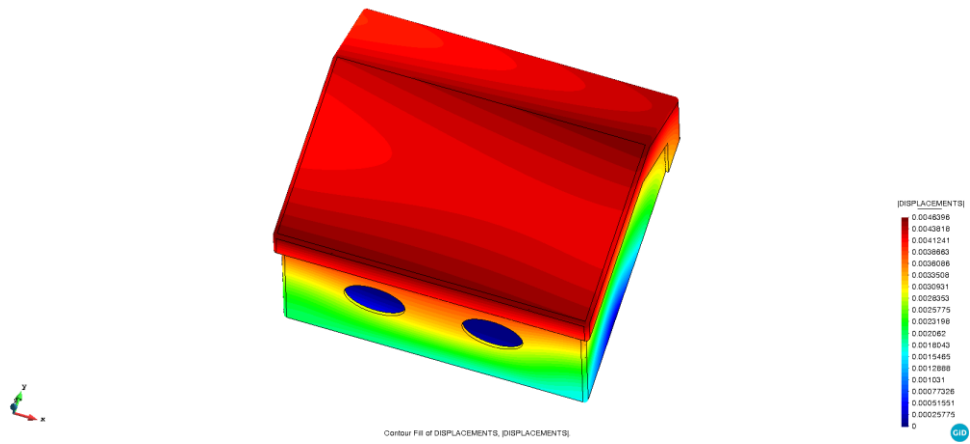
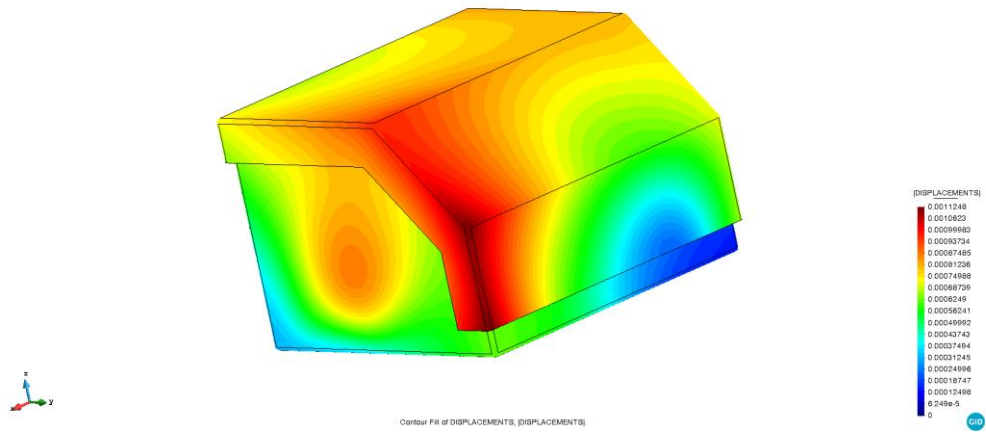


Figure 4.30 Displacement in 6 cases from No.1-6

According to the results above, both of the maximum Von-mises stress and displacement appear in case 2 and 5. It shows that the load in Y direction create maximum stress and displacement. Meanwhile, the maximum stress and displacement appear in different locations according to the load working on XY plane and Z direction. The maximum displacement would appear in the cover and the maximum stress would appear around the edge of the constrains when the load working on XY plane (in X direction or Y direction). Meanwhile, the maximum stress would appear between the two clips of cover and box body and the maximum displacement would appear on the center of the cover when the load working on Z direction. For Von-Mises stress, Case 2 and 5 are both over the yield stress. The left four cases can satisfy the limit in stress. One of the common methods to improve the mechanical performance of the electric box is increasing the wall thickness. Another economic one is adding some ribs on the inside surfaces of the electric box.

Case No.	Max. VM stress (MPa)	Max. Displacement (mm)	Yield stress (MPa)	Results
1	21.1	1.24	42	OK
2	60.3	5.29	42	Failure
3	18.4	4.19	42	OK
4	21.1	1.24	42	OK
5	60.3	5.29	42	Failure
6	18.4	4.19	42	OK

Table 4.12 Summary of results

4.3. Case3 Armrest

4.3.1. Introduction

In this case, an armrest of a train seat is printed by FFF technique. Elix ABS-GP is considered as the material of the armrests. Meanwhile, ULTEM™9085 is considered as the comparing material.



Figure 4.31 Armrest in 3D image

A single right armrest is shown in the Figure 4.32.



Figure 4.32 Armrest printed by FFF

4.3.2. Methodology

The inner structure is made of lattice with octet geometry. To reduce the computational cost in the simulation, RVE technique is used in this case. The Von-mises stresses and displacements in five load cases are evaluated to check the performance of structure. The irregular surfaces are isotropic while the rest are anisotropic.

4.3.3. Result

4.3.3.1. Data

The properties of ABS can be located in the Table 4.13. The data comes from the same approach as PC-ABS, which is the tensile test on dog bones. Meanwhile, the model with square cross section samples is validated.

Material Properties		Contour	Cover
E_{\parallel} [GPa]	E_{\perp} [GPa]	1.94	0.9
E_{iso} [GPa]		1.59	1.54
ν_{iso}		0.3	0.33
ν		0.3	0.33
G [GPa]		0.6	0.45
G_{iso} [GPa]		0.6	0.58

Table 4.13 Properties of ABS in the model

Meanwhile, the properties of ULTEMTM9085 are given according to Albert Forés-Garriga [46] in the Table4.14.

ULTEMTM9085 is a pioneering thermoplastic that is strong, lightweight and flame-retardant. With its superior mechanical performance and strength-to-weight ratio, ULTEMTM9085 is suitable for end-use production-grade components, particularly in the aerospace and automotive industries.

Material Properties	Contour
E_{\parallel} [GPa]	2.24
ν_{iso}	0.35
ν	0.35

Table 4.14 Basic Properties of ULTEM9085 in the model

To carry out the RVE simulation, the properties of E_{\parallel} and ν_{iso} are assigned as the input properties of material in Kratos Calculation.

4.3.3.1.1. Property of octet RVE lattice

Properties	Results	Units	
E	33.3	MPa	Calculated by Kratos
G	12.8	MPa	Calculated by Kratos
ν	0.33		Calculated by Kratos

Table 4.15 Properties of Octet RVE lattice with the material ABS

Properties	Results	Units	
E	38.5	MPa	Calculated by Kratos
G	14.7	MPa	Calculated by Kratos
ν	0.33		Calculated by Kratos

Table 4.16 Properties of Octet RVE lattice with the material ULTEMTM9085

Octet RVE lattice Compliance tensor substitute $E_x = E_y = E_z = E, G_{xy} = G_{xz} = G_{yz} = G, \nu_{yx} = \nu_{zx} = \nu_{zy} = \nu$ in table 4.16 and 4.17 from Eq.4.8, yield

$$S = \begin{bmatrix} \frac{1}{E} & -\frac{\nu}{E} & -\frac{\nu}{E} & 0 & 0 & 0 \\ -\frac{\nu}{E} & \frac{1}{E} & -\frac{\nu}{E} & 0 & 0 & 0 \\ -\frac{\nu}{E} & -\frac{\nu}{E} & \frac{1}{E} & 0 & 0 & 0 \\ 0 & 0 & 0 & \frac{1}{G} & 0 & 0 \\ 0 & 0 & 0 & 0 & \frac{1}{G} & 0 \\ 0 & 0 & 0 & 0 & 0 & \frac{1}{G} \end{bmatrix} = C^{-1} \quad (4.15)$$

The constitutive tensor of Octet RVE with material ABS

$$C = S^{-1} = \begin{bmatrix} 49,338,788 & 24,301,194 & 24,301,194 & 0 & 0 & 0 \\ 24,301,194 & 49,338,788 & 24,301,194 & 0 & 0 & 0 \\ 24,301,194 & 24,301,194 & 49,338,788 & 0 & 0 & 0 \\ 0 & 0 & 0 & 12,800,000 & 0 & 0 \\ 0 & 0 & 0 & 0 & 12,800,000 & 0 \\ 0 & 0 & 0 & 0 & 0 & 12,800,000 \end{bmatrix} \quad (4.16)$$

The constitutive tensor of Octet RVE with material ULTEM

$$C = S^{-1} = \begin{bmatrix} 57043344 & 28095975 & 28095975 & 0 & 0 & 0 \\ 28095975 & 57043344 & 28095975 & 0 & 0 & 0 \\ 28095975 & 28095975 & 57043344 & 0 & 0 & 0 \\ 0 & 0 & 0 & 14700000 & 0 & 0 \\ 0 & 0 & 0 & 0 & 14700000 & 0 \\ 0 & 0 & 0 & 0 & 0 & 14700000 \end{bmatrix} \quad (4.17)$$

4.3.3.1.2. Property of contour

As this paper talked before, the property of contour is simplified as isotropic material in the following table.

Properties	Results	Units
E_{\parallel}	1.94	GPa
$\nu_{iso_contour}$	0.3	

Table 4.17 Properties of Contour with material ABS

Properties	Results	Units
E_{\parallel}	2.24	GPa
$\nu_{iso_contour}$	0.35	

Table 4.18 Properties of Contour with material ULTEMTM9085

4.3.3.1.3. Property of cover

Compliance tensor of cover substitute $E_x = E_z = E, G_{xy} = G_{zy} = G, \nu_{yx} = \nu_{yz} = \nu$ in table 4.12 from Eq.4.8, yield

$$S = \begin{bmatrix} \frac{1}{E} & -\frac{\nu}{E_y} & -\frac{\nu_{zx}}{E} & 0 & 0 & 0 \\ -\frac{\nu}{E} & \frac{1}{E_y} & -\frac{\nu}{E_y} & 0 & 0 & 0 \\ -\frac{\nu_{zx}}{E} & -\frac{\nu}{E_y} & \frac{1}{E} & 0 & 0 & 0 \\ 0 & 0 & 0 & \frac{1}{G} & 0 & 0 \\ 0 & 0 & 0 & 0 & \frac{1}{G_{zx}} & 0 \\ 0 & 0 & 0 & 0 & 0 & \frac{1}{G} \end{bmatrix} = C^{-1} \quad (4.18)$$

The constitutive tensor of cover with the material ABS

$$C = S^{-1} = \begin{bmatrix} 3,168,749,602 & 1,709,269,474 & 2,010,854,865 & 0 & 0 & 0 \\ 1,709,269,474 & 2,028,117,853 & 1,709,269,474 & 0 & 0 & 0 \\ 2,010,854,865 & 1,709,269,474 & 3,168,749,602 & 0 & 0 & 0 \\ 0 & 0 & 0 & 450000000 & 0 & 0 \\ 0 & 0 & 0 & 0 & 578,947,368 & 0 \\ 0 & 0 & 0 & 0 & 0 & 450000000 \end{bmatrix} \quad (4.19)$$

The compliance tensor of cover from [46] with the material ULTEMTM9085. Specially, this tensor is from the results of experiments. It is not coincided with the theoretical one 100%.

$$S = \begin{bmatrix} 4.78e-10 & -1.75e-10 & -1.64e-10 & 0 & 0 & 0 \\ -1.75e-10 & 4.7e-10 & -1.75e-10 & 0 & 0 & 0 \\ -1.64e-10 & -1.75e-10 & 4.65e-10 & 0 & 0 & 0 \\ 0 & 0 & 0 & 1.36e-9 & 0 & 0 \\ 0 & 0 & 0 & 0 & 1.59e-9 & 0 \\ 0 & 0 & 0 & 0 & 0 & 1.34e-9 \end{bmatrix} \quad (4.20)$$

The constitutive tensor of cover with the material ULTEM™9085

$$C = S^{-1} = \begin{bmatrix} 3552363118 & 2080757590 & 2035957268 & 0 & 0 & 0 \\ 2080757590 & 3693172232 & 2123762119 & 0 & 0 & 0 \\ 2035957268 & 2123762119 & 3,168,749,602 & 0 & 0 & 0 \\ 0 & 0 & 0 & 737463127 & 0 & 0 \\ 0 & 0 & 0 & 0 & 630119723 & 0 \\ 0 & 0 & 0 & 0 & 0 & 745156483 \end{bmatrix} \quad (4.21)$$

4.3.3.2. Geometry

4.3.3.2.1. Full geometry

The model was simplified as following.

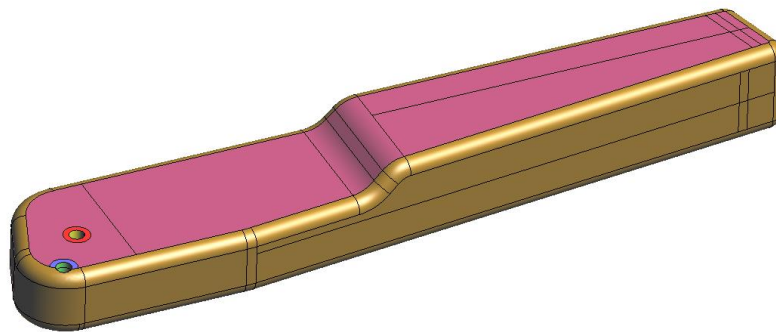


Figure 4.33 Full geometry

4.3.3.2.2. Octet RVE geometry

The Octet RVE geometry is created from a cubic whose side length is 40mm. The thickness of the cubic is 3mm. Meanwhile, the diameter of each cylinder is 5mm. Finally, we got an Octet RVE geometry as $34 \times 34 \times 34mm$.

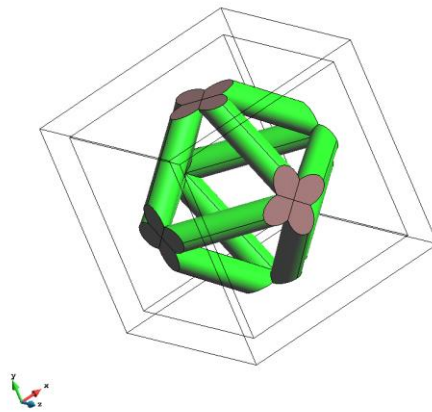


Figure 4.34 Octet RVE geometry

4.3.3.3. Loads and boundary conditions

4.3.3.3.1. Loads

4.3.3.3.1.1. Loads of full geometry

Five Loading cases working on the armrest are considered. They are H_1, H_2, H_3 and $H_3 + H_1, H_3 + H_2$. Where, $H_1 = H_2 = H_3 = 1000N$ and H_3 applied on point 1, H_1 applied on point 2, H_1 applied on point 3.

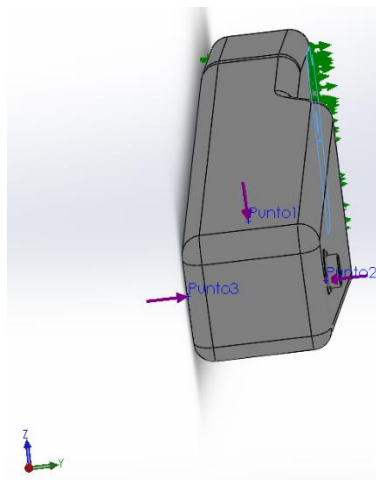


Figure 4.35 Loading on the three points

Case No.	Load direction
1	H_1
2	H_2
3	H_3
4	H_3+H_1
5	H_3+H_2

Table 4.19 Loads combination on the five cases

4.3.3.3.1.2. Loads of Octet RVE geometry

The following figure only shows the geometry of the octet. The results are obtained from the simulation.

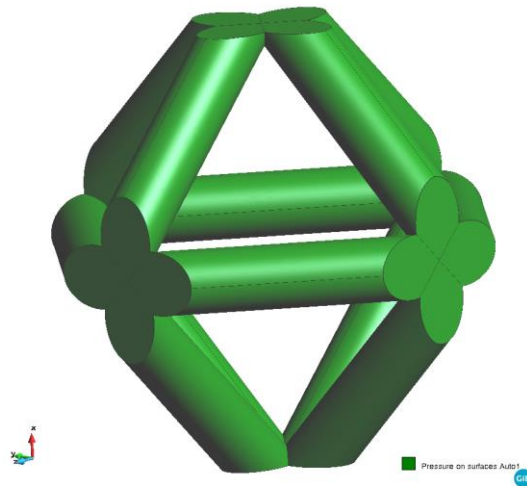


Figure 4.36 Loads on Octet RVE geometry

4.3.3.3.2. Constrains

4.3.3.3.2.1. Constrains of full geometry

All the inside surfaces of two holes were fixed. Meanwhile, one part of the surface was fixed on the test frame.

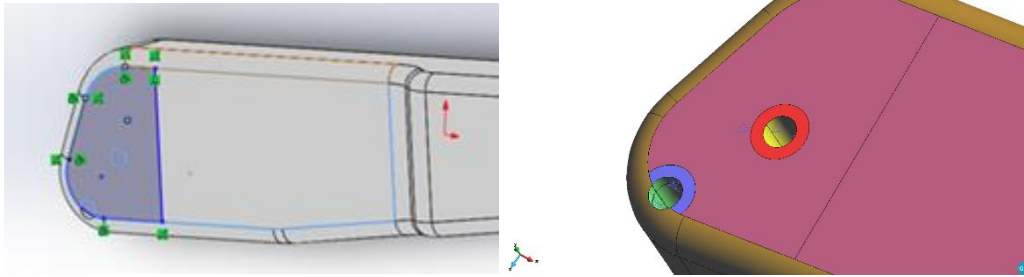


Figure 4.37 Constrains

4.3.3.3.3. Mesh

4.3.3.3.3.1. Mesh on full geometry

2,300,000 elements were divided into two parts which are Critical part and Sub-Critical part according to coarse mesh calculation result. Generally, the location around two holes and three load points constitute the Critical parts.

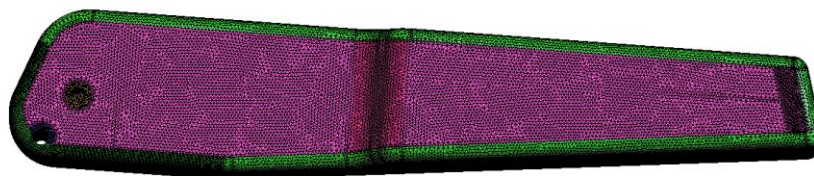


Figure 4.38 Full Mesh

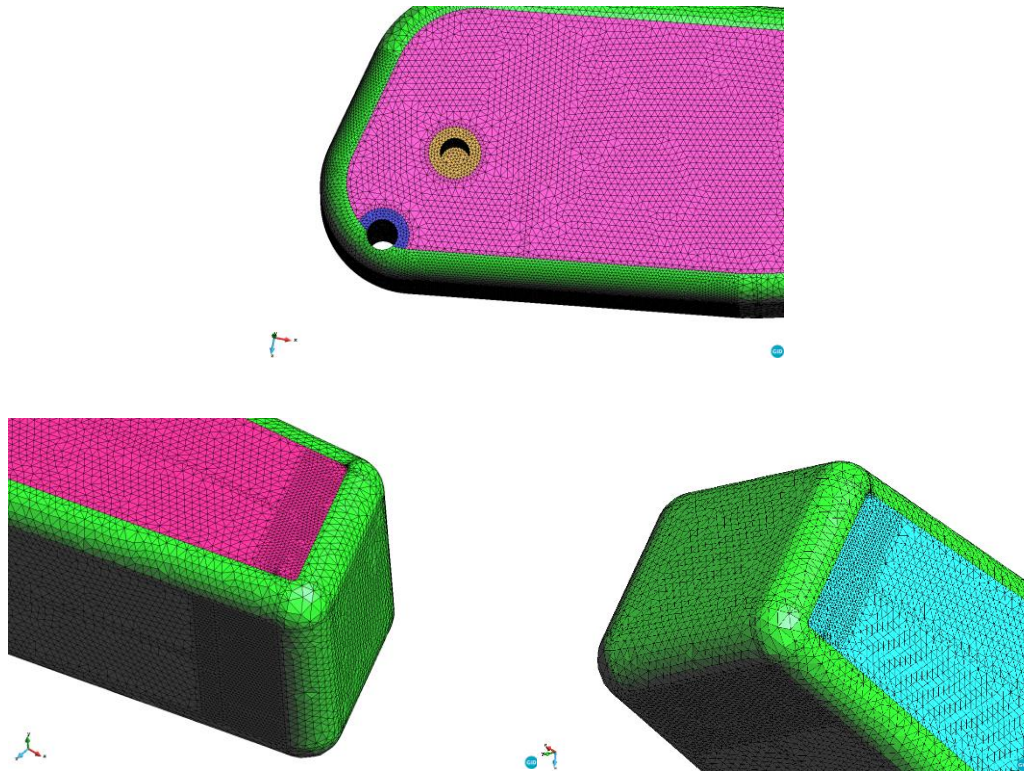


Figure 4.39 Mesh on critical part

4.3.3.3.2. Mesh on Octet RVE geometry

There are 8,800,000 elements in this mesh. The maximum element size of mesh is 0.2mm.

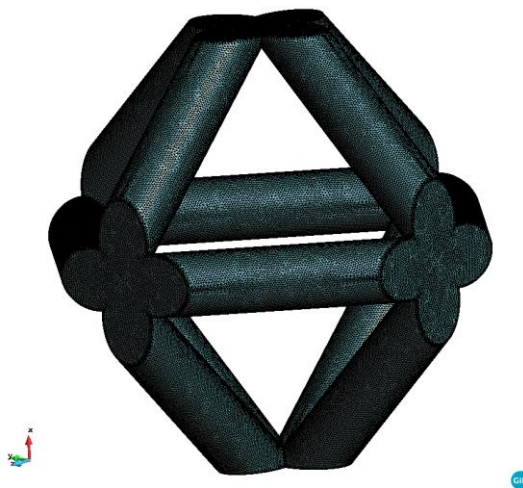


Figure 4.40 Octet RVE Mesh

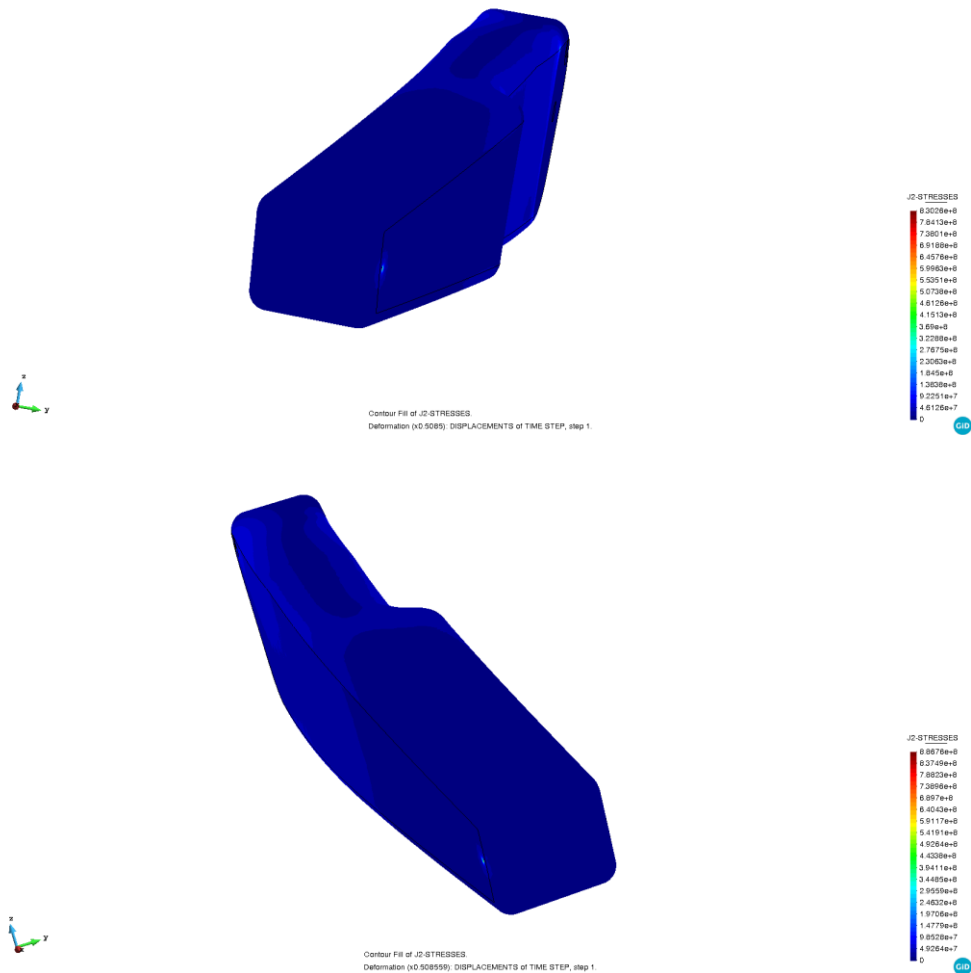
4.3.3.4. Results

4.3.3.4.1. Results of Octet RVE geometry with the material of ABS

According to the Kratos' calculation with the material of ABS, constitutive tensor C is obtained.

$$C = \begin{bmatrix} 49304866 & 24246556 & 24244535 & -211 & -398 & -447 \\ 24246570 & 49305420 & 24244564 & -494 & -396 & -404 \\ 24244523 & 24244568 & 49304980 & 340 & -286 & -470 \\ -239 & -486 & 339 & 12830419 & -324 & -521 \\ -406 & -393 & -288 & -324 & 12829538 & 133 \\ -421 & -414 & -483 & -525 & 136 & 12829593 \end{bmatrix} \quad (4.22)$$

4.3.3.4.2. Results of 5 cases with the material of ABS



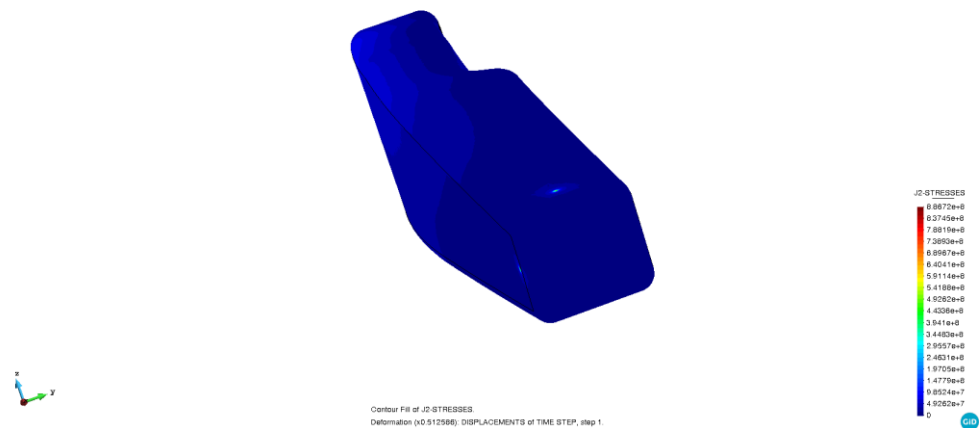
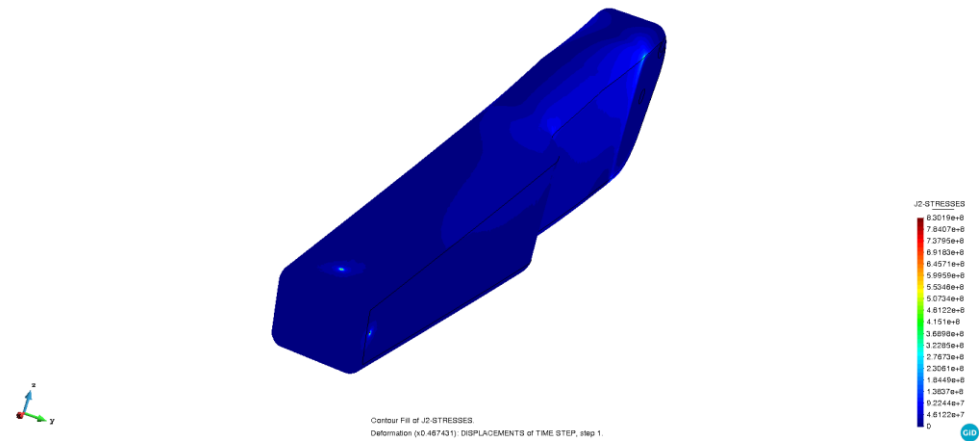
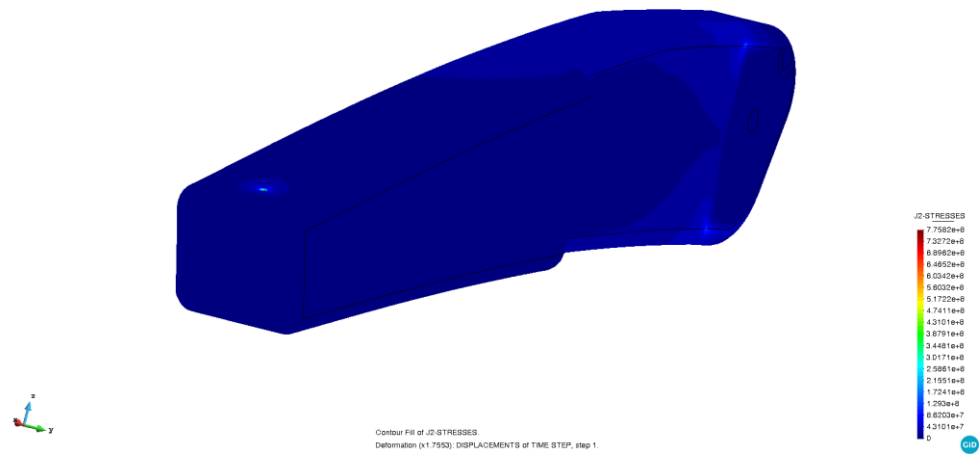
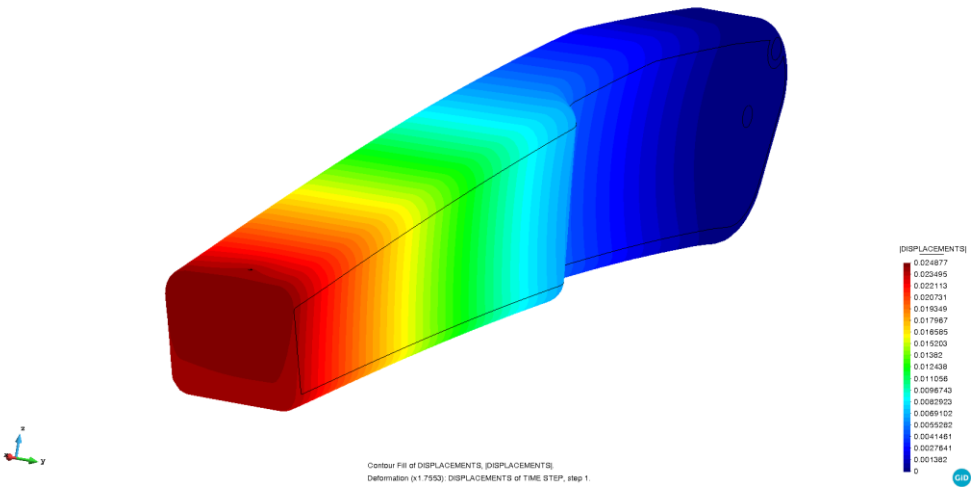
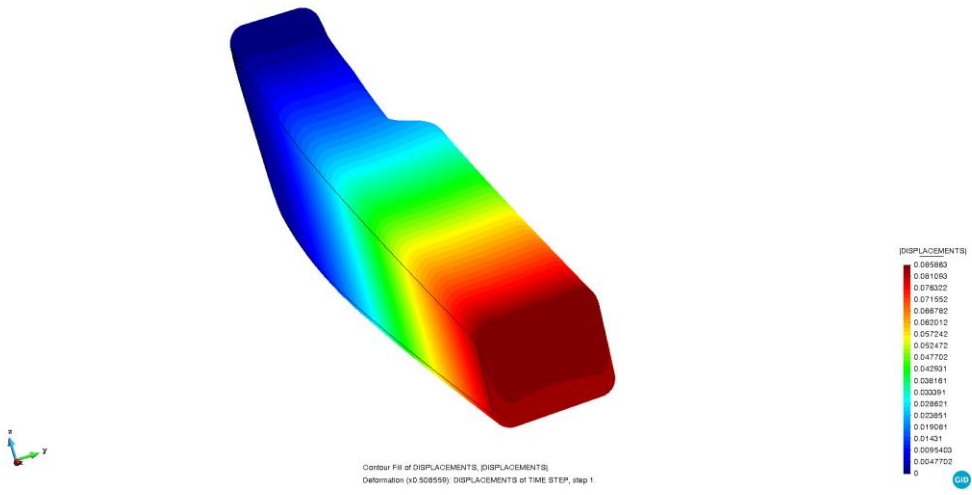
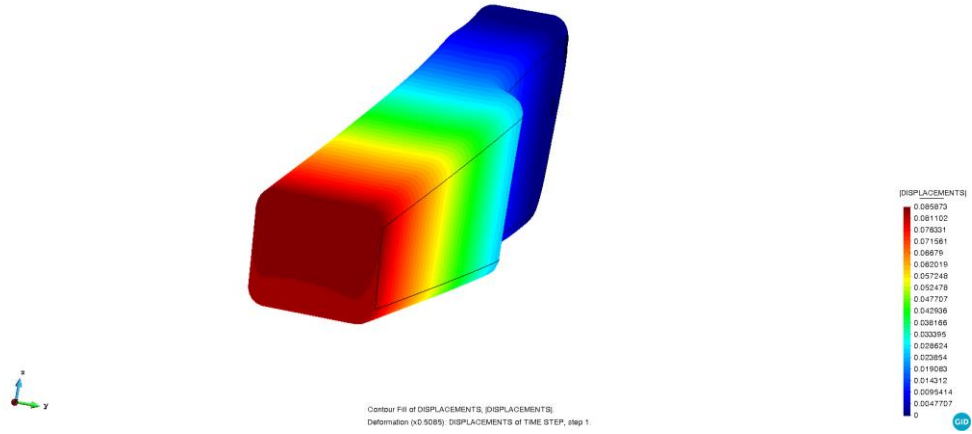


Figure 4.41 Von-mises stresses in the 5 cases in order with the material of ABS



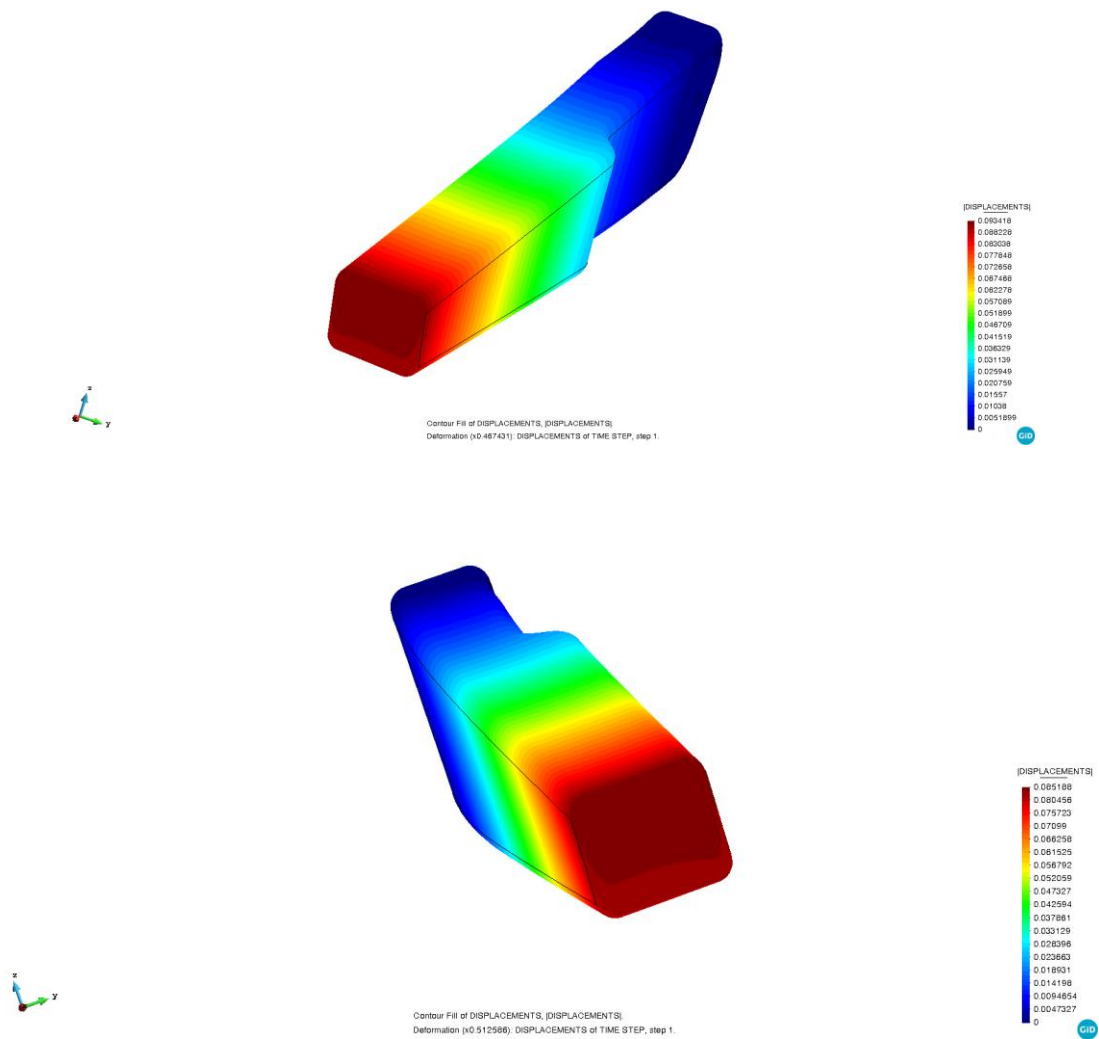


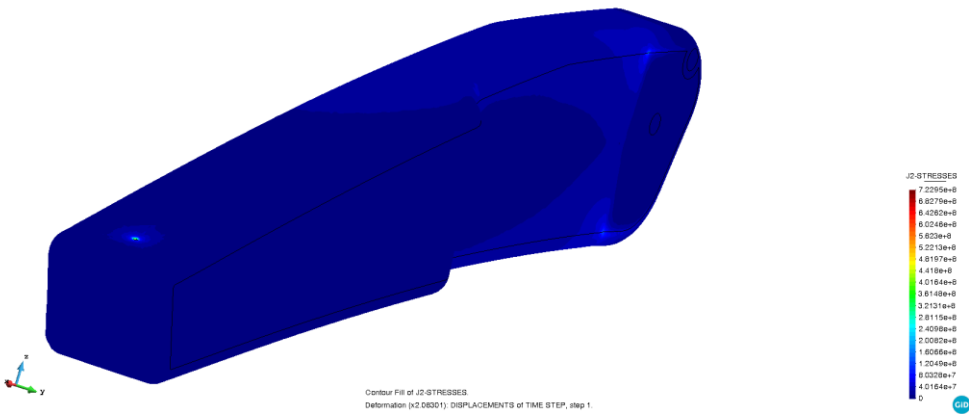
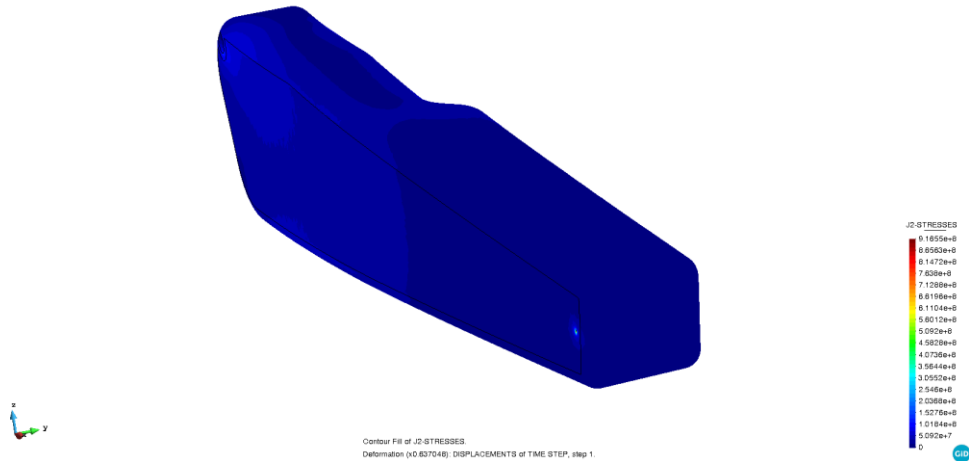
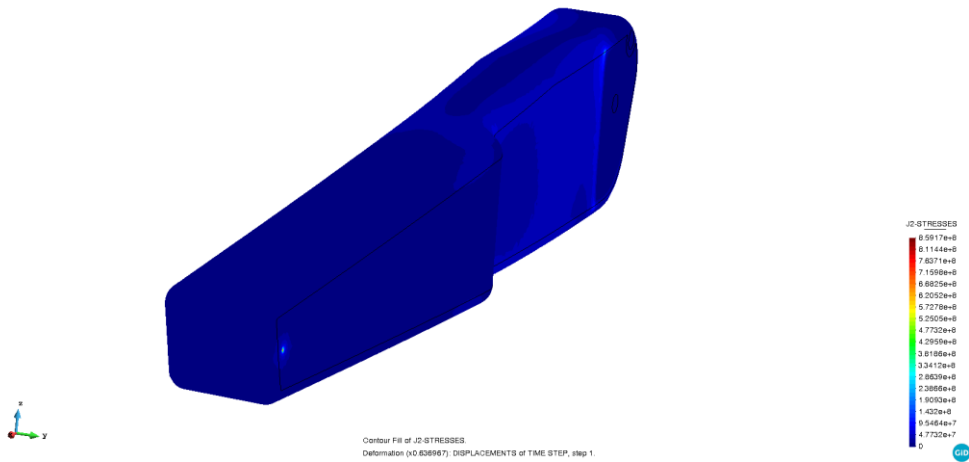
Figure 4.42 Displacements in the 5 cases in order with the material of ABS

4.3.3.4.3. Results of Octet RVE geometry with the material of ULTEM™9085

According to the Kratos' calculation with the material of ULTEM™9085, constitutive tensor C is obtained.

$$C = \begin{bmatrix} 57915600 & 29054177 & 29051716 & -297 & -499 & -615 \\ 29054158 & 57916349 & 29051809 & -695 & -540 & -536 \\ 29051718 & 29051800 & 57915957 & 400 & -369 & -678 \\ -325 & -689 & 401 & 14736142 & -427 & -623 \\ -503 & -531 & -369 & -425 & 14734966 & 111 \\ -591 & -552 & -690 & -624 & 115 & 14734959 \end{bmatrix} \quad (4.23)$$

4.3.3.4.4. Results of 5 cases with the material of ULTEM™9085



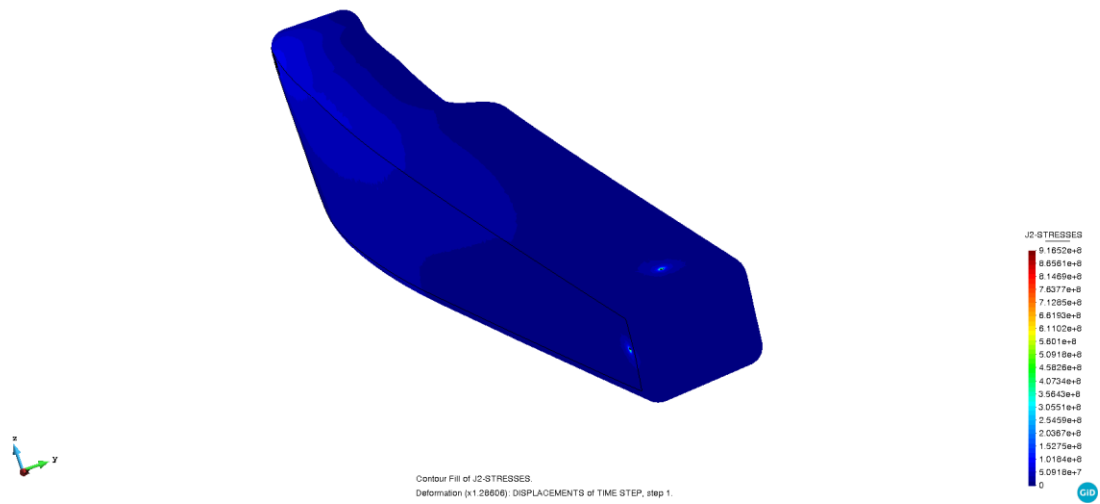
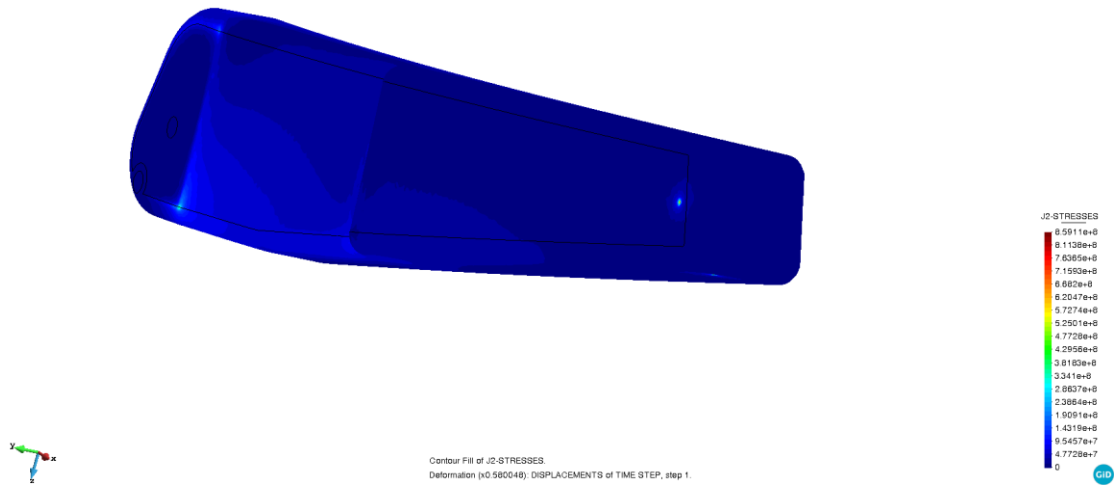
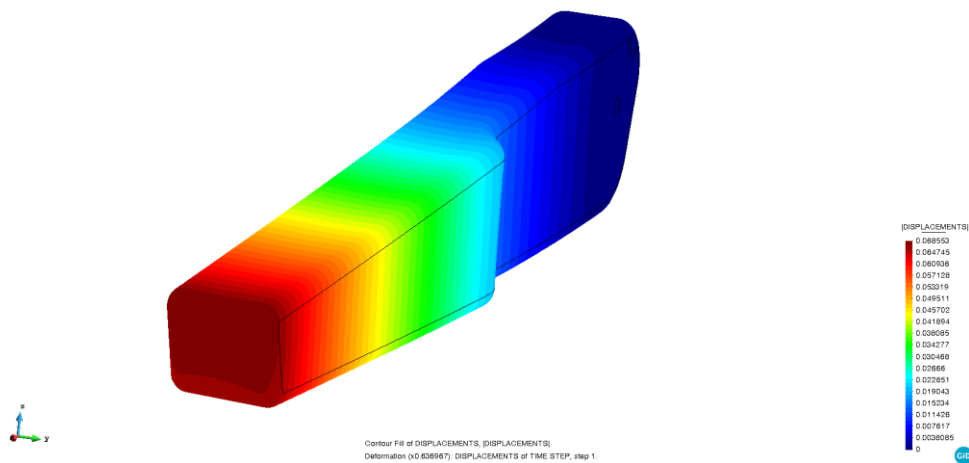
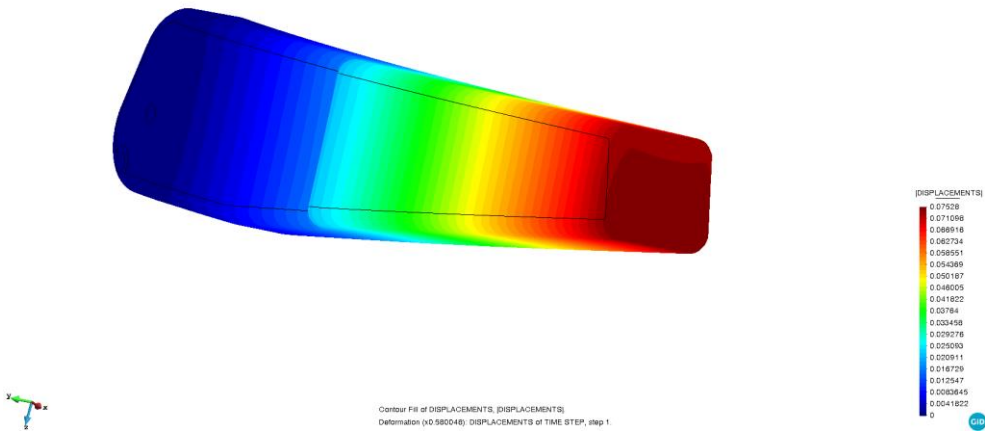
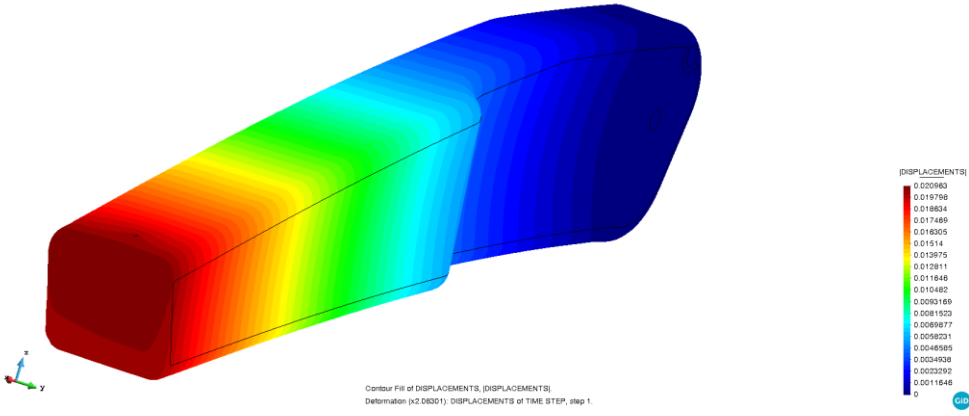
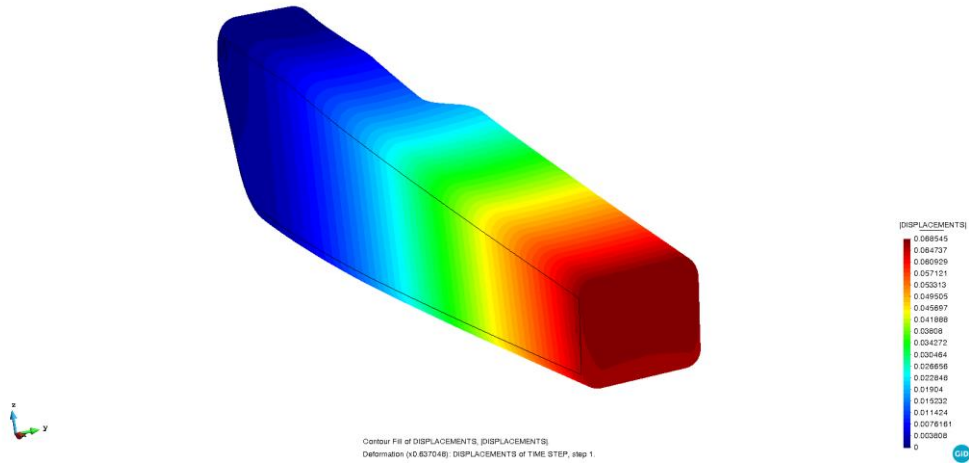


Figure 4.43 Von-mises stresses in the 5 cases in order with the material of ULTEM™9085





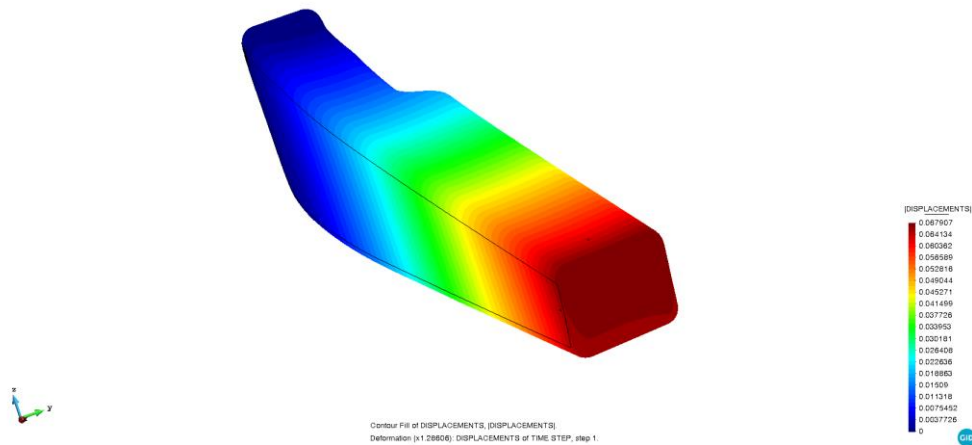


Figure 4.44 Displacements in the 5 cases in order with the material of ULTEM™9085

4.3.3.5. Conclusion

According to the results in the above, all the maximum Von-mises stress appear in the load point. The locations are in H_1 , H_2 and H_3 loading point. Meanwhile, large displacement appears in the end of Armrest. The maximum displacement in the five case is 93mm in ABS, while 75mm in ULTEM™9085

Comparing the results of different material, the ABS and ULTEM™9085, ULTEM™9085 perform better than ABS. If the stress concentration at the singular points is not considered, ULTEM™9085 has the lower stress than ABS GP. ULTEM™9085 present smaller displacement than ABS. That is as expected because ULTEM is known as presenting higher strength than ABS. The maximum stresses in the places that are not singular mainly located in the transition hillside of top surface.

Case No.	Max. VM stress (MPa) of ABS	Yield Stress of ABS (MPa)	Results of ABS	Max. VM stress (MPa) of ULTEM™9085
1	60.7	39	Failure	57.3
2	60.7	39	Failure	57.3
3	30.4	39	OK	30.2
4	90.7	39	Failure	87.1
5	90.0	39	Failure	84.9

Case No.	Max. Displacement (mm) of ABS			Max. Displacement (mm) ULTEM™9085
1	86			69
2	86			69
3	25			21
4	93			75
5	85			68

Table 4.20 Summary of maximum stresses in the places that are not singular and maximum displacements

4.4. Case4 Handle

4.4.1. Introduction

The current modern equipment in the engineering could be designed to satisfy practical and beautiful requirements. ALSTOM is working on the project of Dubai Metro. One of an interesting design in this subject is the seat handle. Meanwhile, you could recognize it as an artwork. The beautiful geometry increases the application difficulty in engineering. Here, in this case, it is evaluated that the mechanical performance under static loads of the Dubai Metro seat handle with the material Aluminum (Alsi10Mg). This job has been optimized according the original simulation results. Within the following sections, two model (the original one and the optimized one) with different geometries will be introduced.



Figure 4.45 Seat handle in Dubai Metro

4.4.2. Methodology

The numerical simulation instead of practical experiment by FEM is carried out using Comet. The Von-mises stresses in two load case are evaluated to check the strength of the material. According the simulation of the original geometry, the optimized geometry is designed and tested. This is done by increasing the mechanical performance (the geometry modification in the critical parts).

4.4.3. Result

4.4.3.1. Data

Isotropic property of material is considered for this simulation.

Material	(ρ): Density (t/mm ³)	(ν): Poisson's ratio	(E): Modulus of Elasticity (MPa)	(σ_e): Tensile yield strength (MPa)
Aluminum (AlSi10Mg)	2.68E-09	0.3	70000	245

Table 4.21 Aluminum Property

$$\text{Aluminum(AlSi10Mg)} \left\{ \begin{array}{l} E = 7e10 \text{ Pa} \\ \nu = 0.3 \\ \rho = 2680 \frac{\text{kg}}{\text{m}^3} \\ t = 0.0001 \text{ m (for surface)} \\ \sigma_e = 245 \text{ Mpa} \end{array} \right.$$

Criteria

$$\sigma_c \leq \sigma_e / 1.15$$

Then, allowable stress is computed as

$$\sigma = 213 \text{ Mpa}$$

4.4.3.2. Original Geometry

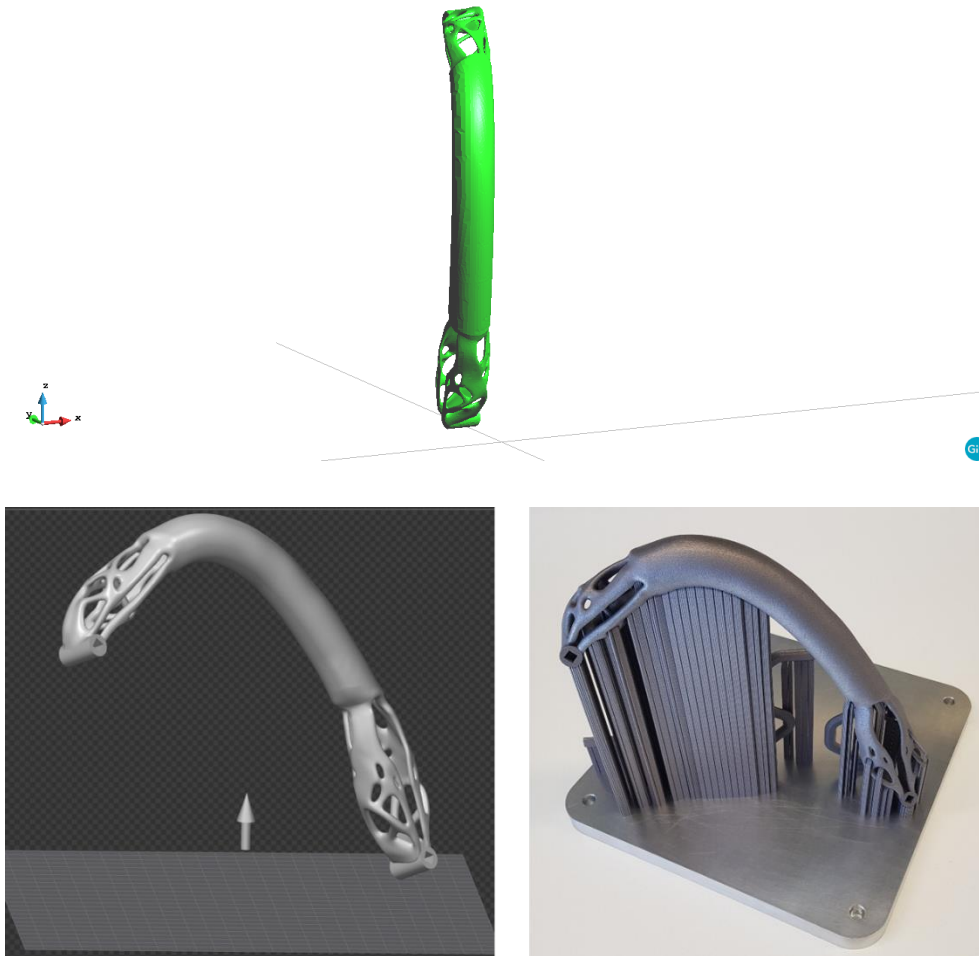


Figure 4.46 Original geometry

4.4.3.3. Loads and boundary conditions on the original geometry

4.4.3.3.1. Loads on the original geometry

There are two cases applying on the original handle. One is uniform pressure assigned on the left side of handle where the force is 900 N working on the surface area 0.006178 m^2 . Another one is uniform pressure assigned on the right side of handle where the force is 900 N working on the surface area 0.006572 m^2 .

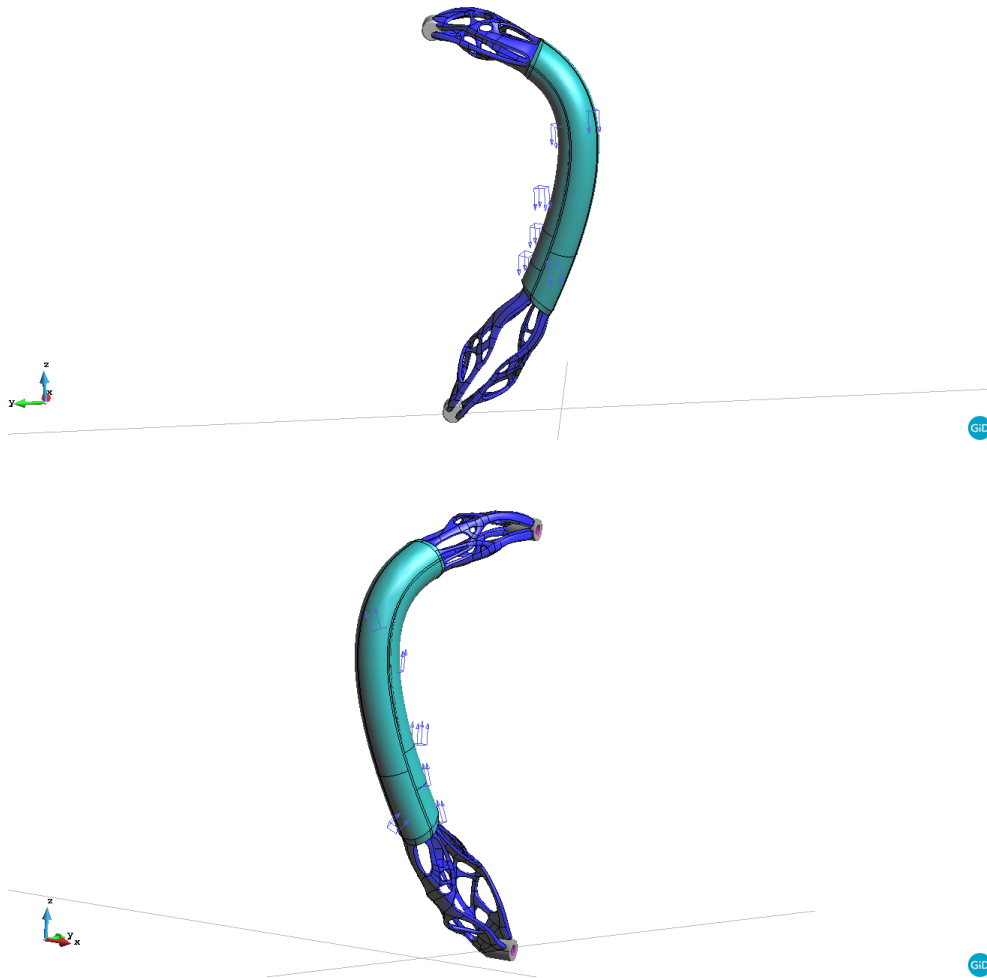


Figure 4.47 Loads on the original geometry, case1 (1st), case2 (2nd)

Case No.	Original model (Pa)
1	145,678
2	136,944

Table 4.22 Loading cases in the original model

4.4.3.3.2. Constrains on the original geometry

The inside surfaces of the holes in the top and bottom support are connected with the seat. Therefore, they are fixed.

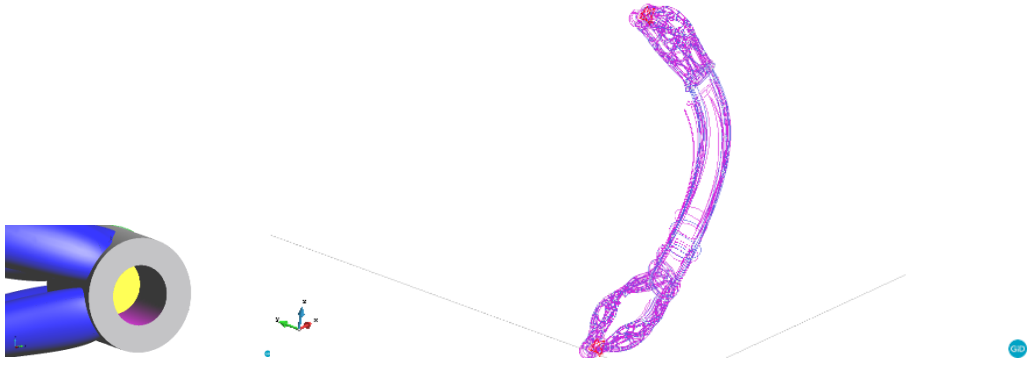


Figure 4.48 Constrains on the original geometry

4.4.3.4. Mesh on the original model

2,225,550 tetrahedra elements are assigned on this geometry. As the critical parts, the mesh on the supports and the transition parts are refined.

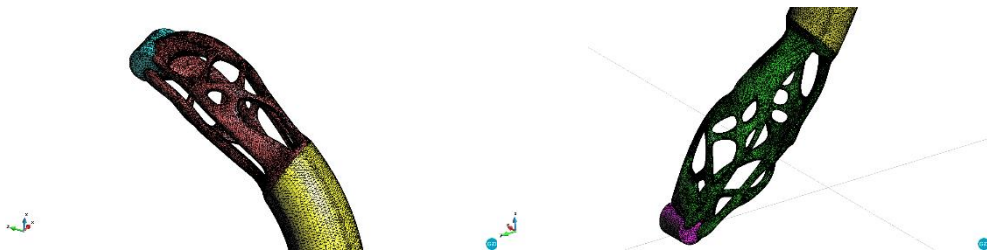


Figure 4.49 Mesh on the original model

4.4.3.5. Result in the original model

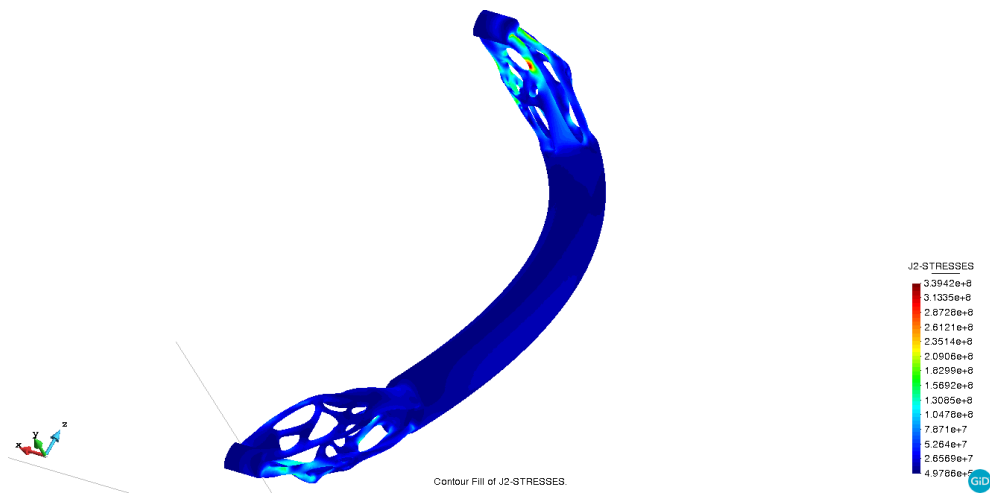
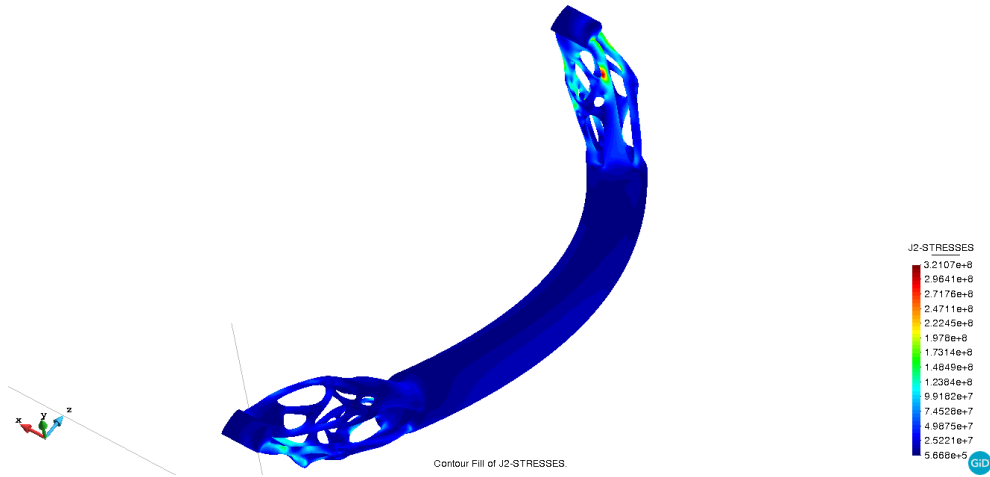
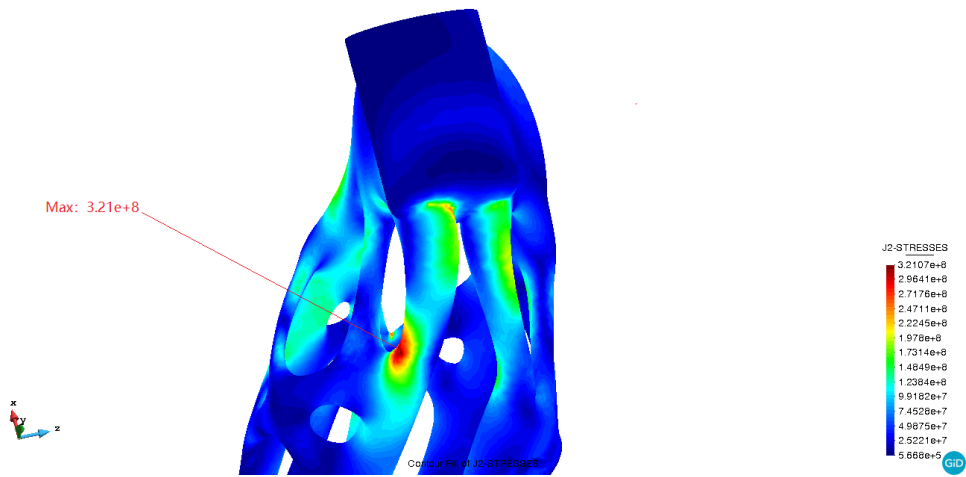


Figure 4.50 Von-mises stress in original model, case1 (1st), case2 (2nd)



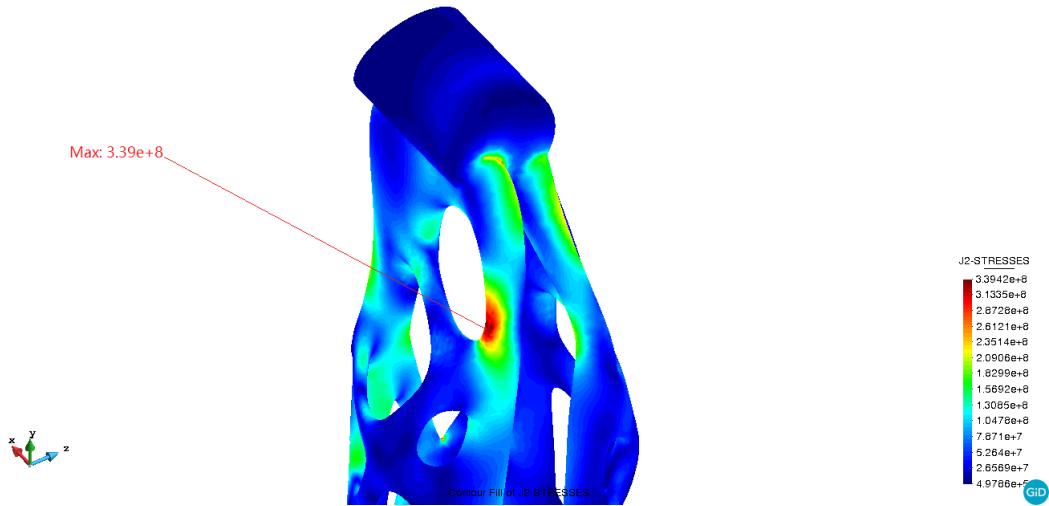


Figure 4.51 MaxVon-mises stress in original model, case1 (1st), case2 (2nd)

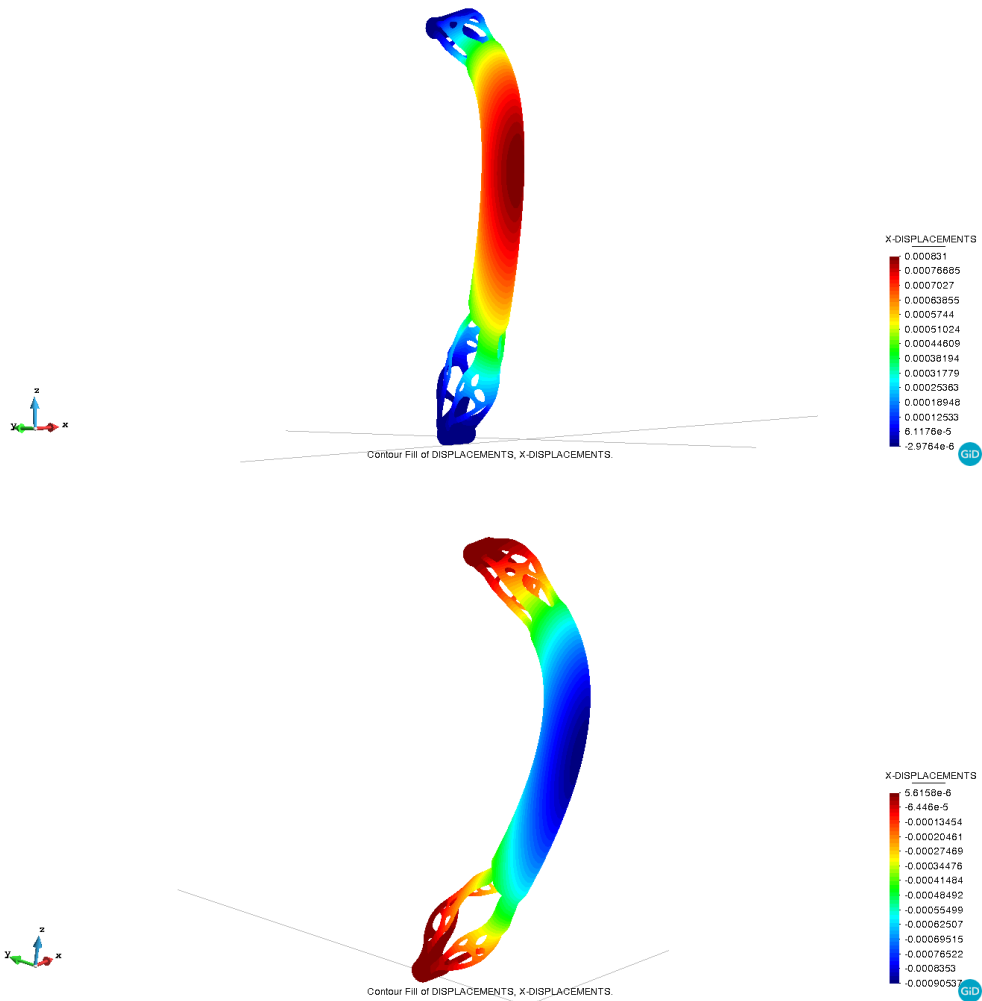


Figure 4.52 Displacement in X direction in original model, case1 (1st), case2 (2nd)

4.4.3.6. Conclusion of original geometry

For the original model, Aluminum (AlSi10Mg) exceeds the limit in the connection and cannot satisfy the requirement in strength. Both of the maximum stresses in these two cases are over then the allowable stress. The maximum stresses mainly expose on the transition part and the connecting parts between support and transition part. The stress on the body is lower. According the result, in order to get the lower stress to satisfy the allowable stress in critical part. The optimized job should be carried out, especially in the weak part of the original model.

Case No.	Max. VM stress (MPa)	Allowable stress (MPa)	Results
1	321	213	Failure
2	339	213	Failure

Table 4.23 Summary of Maximum stress in original model

4.4.3.7. Optimized geometry

The mainly modification between the optimized geometry and the original one is the support and the complicated transition parts connecting the handle body and the support. See Figure 4.53.

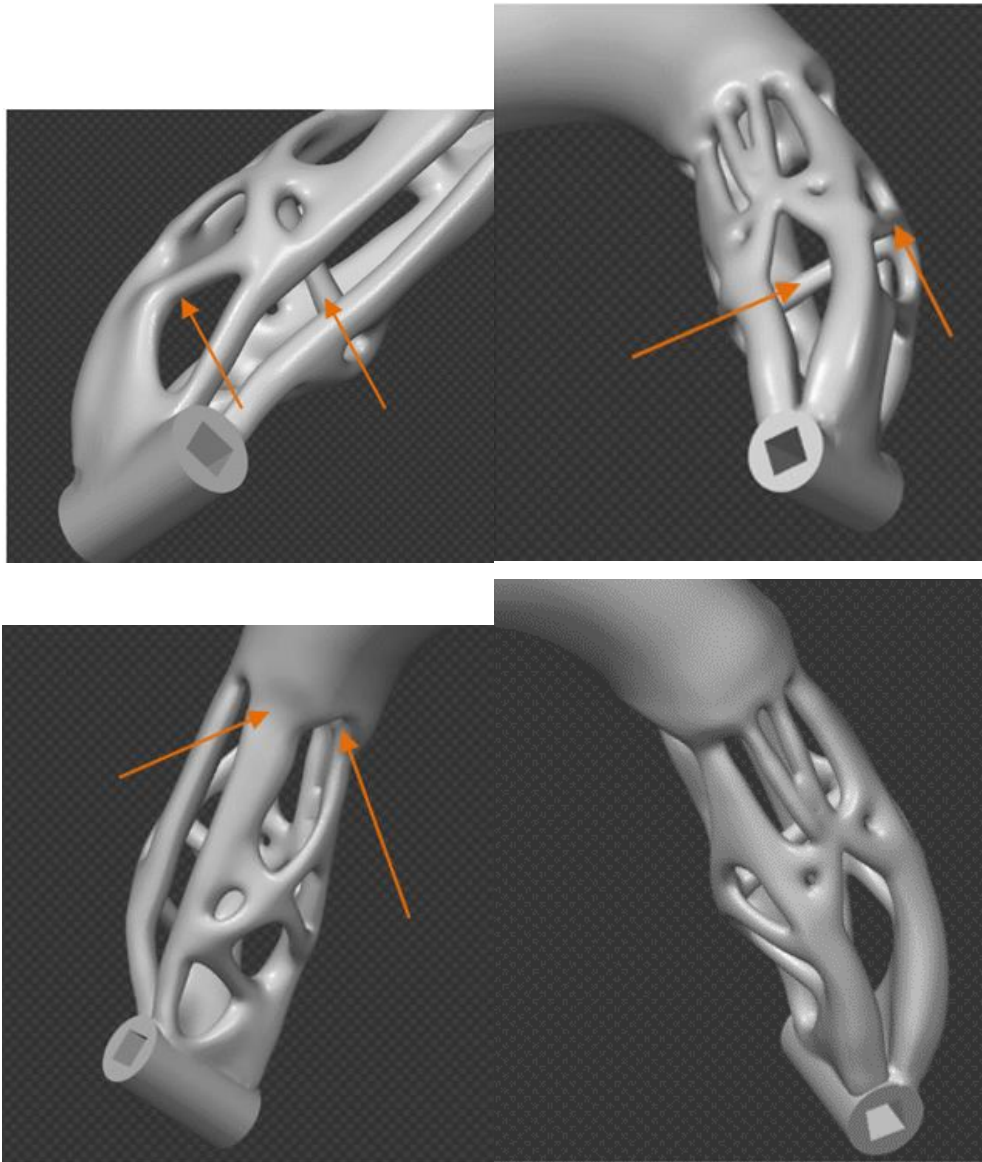


Figure 4.53 The parts to be optimized

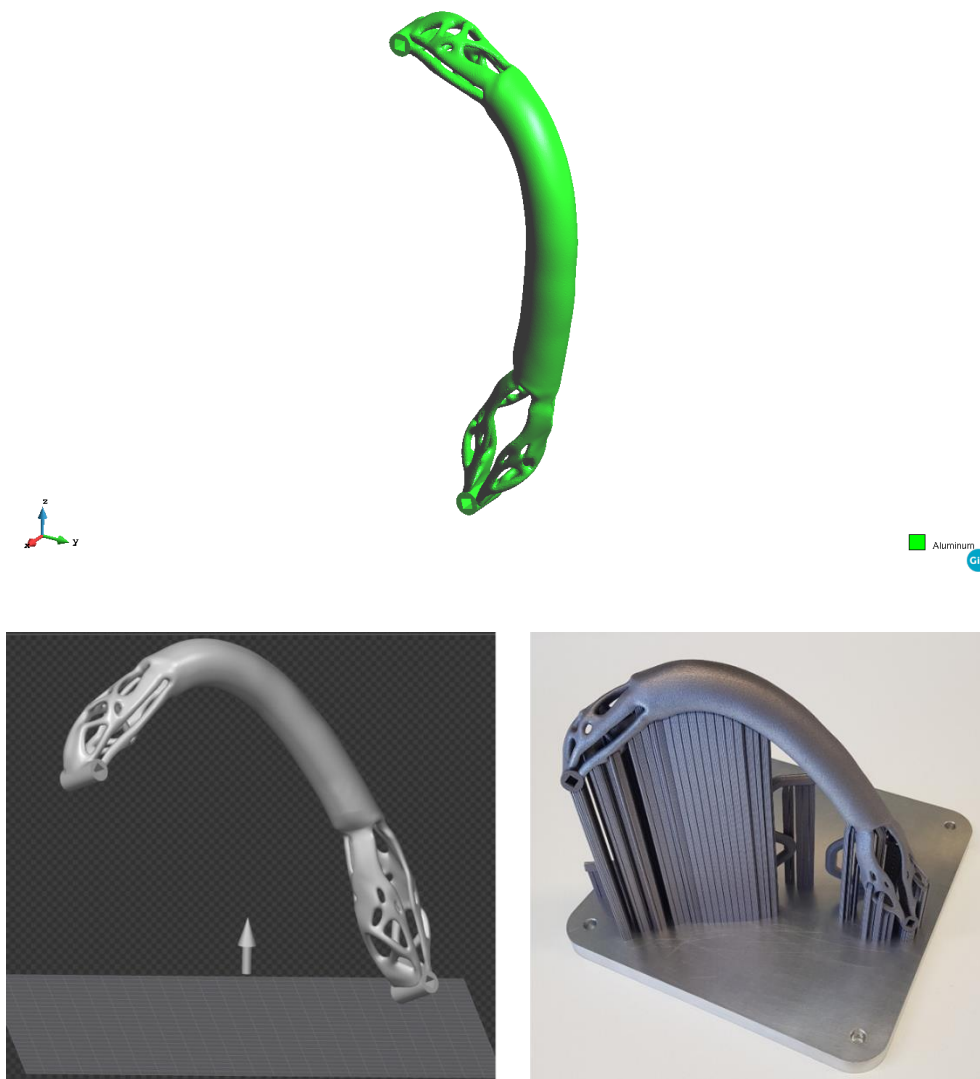


Figure 4.54 Optimized geometry

4.4.3.8. Loads and boundary conditions on the optimized geometry

4.4.3.8.1. Loads on the optimized geometry

There are two cases applying on the optimized handle. One is uniform pressure assigned on the left side of handle where the force is 900 N working on the surface area 0.006834 m^2 . Another one is uniform pressure assigned on the right side of handle where the force is 900 N working on the surface area 0.006405 m^2 .



Figure 4.55 Loads on the optimized geometry, case1 (1st), case2(2nd)

Case No.	Optimized model (Pa)
1	131,694
2	140,515

Table 4.24 Loading cases in optimized model

4.4.3.8.2. Constrains on the optimized geometry

The inter-surfaces of top and bottom plug are fixed.

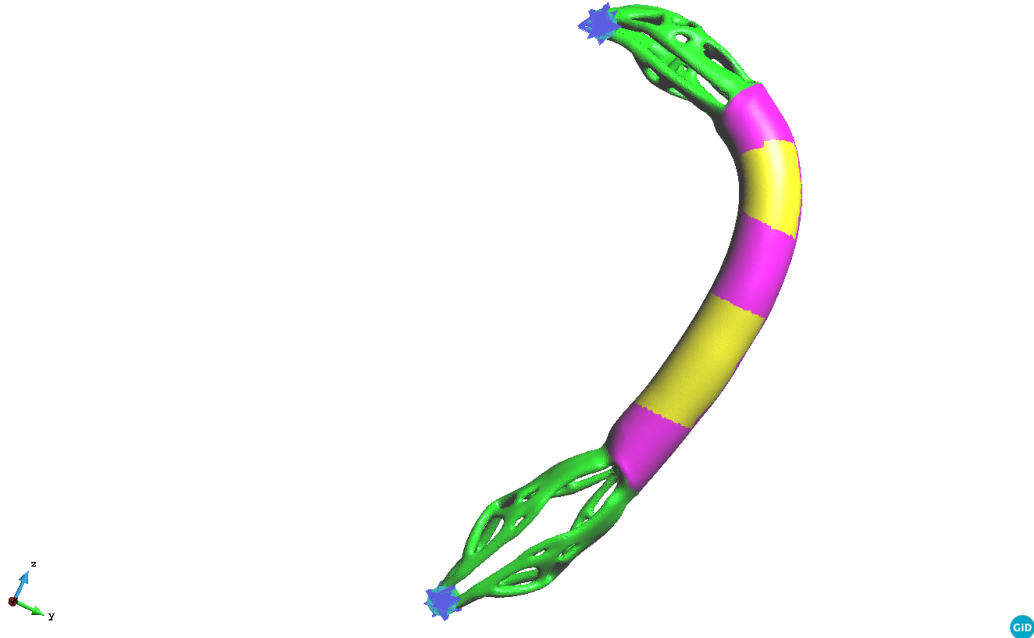


Figure 4.56 Constrains on the optimized geometry

4.4.3.9. Mesh on the optimized model

7,400,000 tetrahedra elements are assigned on this optimized geometry.

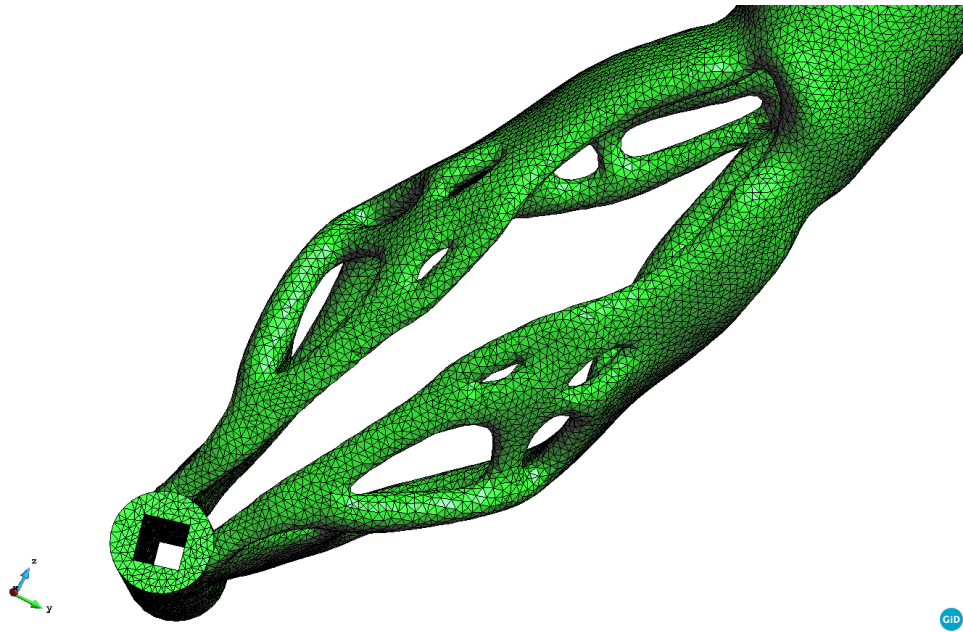
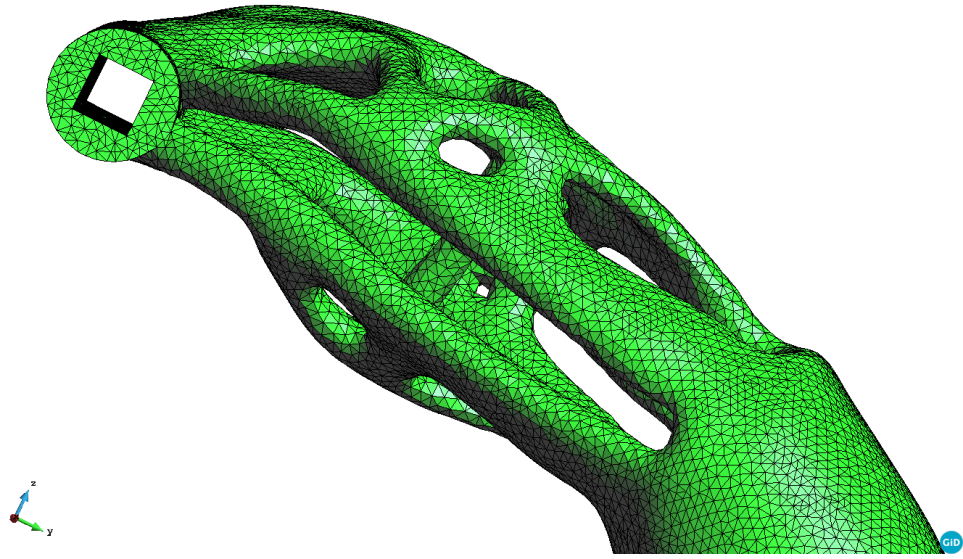


Figure 4.57 Mesh on the optimized model

4.4.3.10. Result in the optimized model

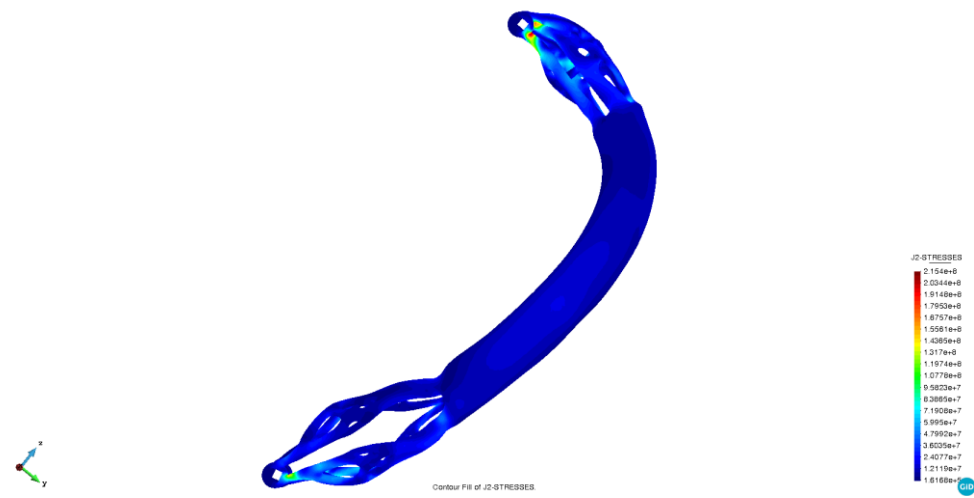
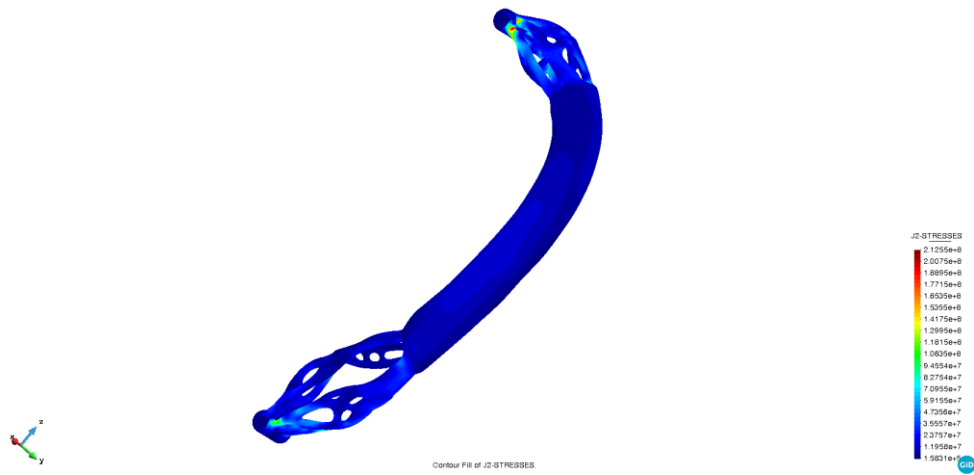
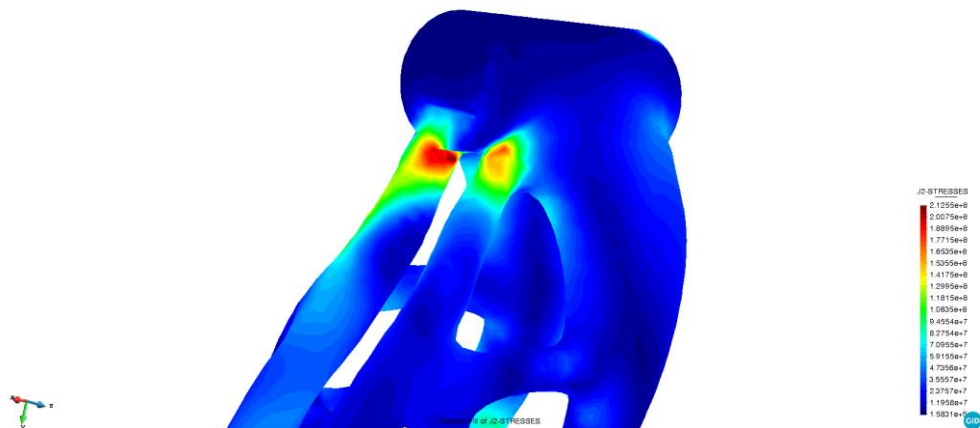


Figure 4.58 Von-mises stress in optimized model, case1 (1st), case2 (2nd)



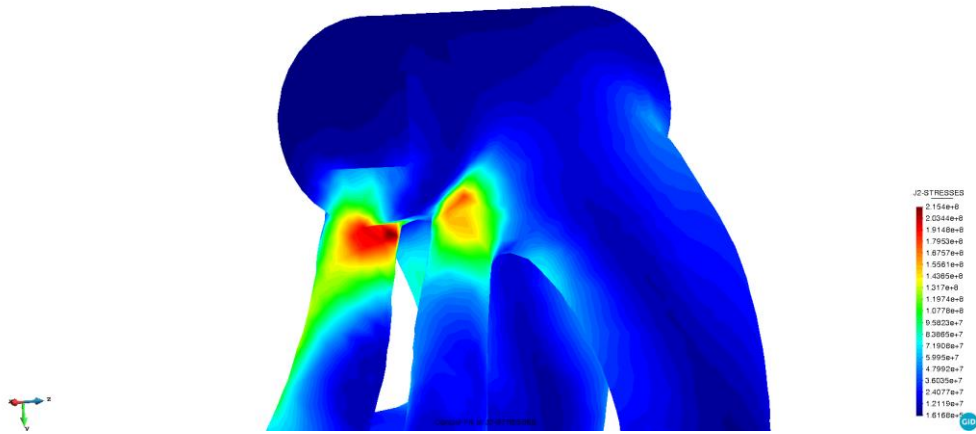


Figure 4.59 Max Von-mises stress in optimized model, case1 (1st), case2 (2nd)

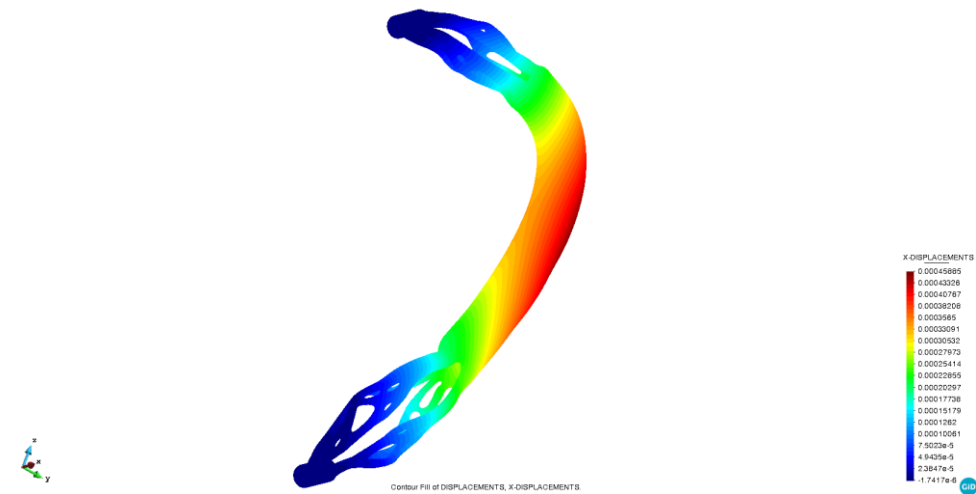
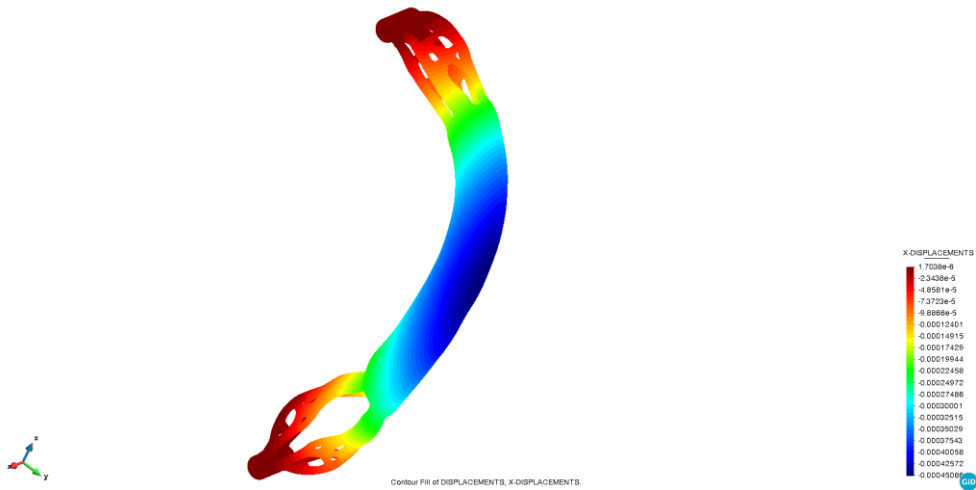


Figure 4.60 Displacement in X direction in optimized model, case1 (1st), case2(2nd)

4.4.3.11. Conclusion of optimized geometry

For the optimized model, the maximum stress exposes on the transition parts close to the top support. Most of stress distribution can satisfy the criteria about the allowable stress except only one point which can be neglected due to the mesh. The entire part does not fail.

Case No.	Max. VM stress (MPa)	Allowable stress (MPa)	Results
1	208.6	213	OK
2	211.4	213	OK

Table 4.25 Summary of Maximum stress in optimized model

5. Conclusions and future work

5.1. Conclusions

In this work, the material characterization and mechanical performance of FFF components is examined experimentally and computationally. The mechanical response of the 3D printed structure depends on the printing pattern used for the manufacturing. Accordingly, three regions are distinguished in the FFF component: the contour, the cover and the in-fill structure. The constitutive material characteristic varies depending on the region and exhibit anisotropic behavior, even though the raw material is isotropic.

The transversely isotropic material properties of the contour and the cover are characterized through extensive experimental tests performed on the dog-bone FFF specimens. The material characterization is carried out for PC-ABS 3D. It is found that the values of material parameters of contour and cover are different and lower than that of the raw material. To characterize the in-fill material properties, a computational homogenization technique is used with the application of PBC on the chosen RVE.

Square cross-section demonstrators made of PC-ABS 3D are printed at different orientations with a selection of in-fill densities. They are tested experimentally under bending in order to validate the proposal of distinguishing between the mechanical behavior of the contour, the cover and the in-fill, and the experimental determination of their respective mechanical properties. The mechanical performance of AM objects with in-fill structure is affected by the in-fill density and orientation. Increasing the in-fill density increases the stiffness of the structure. The vertically printed samples are the most influenced by the increment of the in-fill density.

Electric box can satisfy the stress limit when the loads apply in X and Z direction. However, the loads in Y direction would result in the demonstrator's failure. Increasing the thickness or adding some ribs on the inside surfaces of electric box are the optimized directions.

The armrest fabricated with the material Elix ABS-GP and ULTEM™9085 leads to the failure in the zones close to the transition hillside of top surface. ULTEM™9085 perform better mechanical performance than Elix ABS-GP both in stress and displacement.

The original geometry of handle cannot satisfy the allowable stress of Aluminum. After optimizing the critical parts (the top and bottom support and the complicated transition parts), the new geometry can satisfy the allowable stress.

5.2. Future work

5.2.1. Large deformations formulation

This TFM worked in the small deformation field. In future, large deformation theory can be taken into account.

As the Figure 5.1, one micro element $d\bar{r}(\overline{PQ})$ deform to $d\bar{r}'(\overline{P'Q'})$.

Yield, $\bar{u} = \bar{r}' - \bar{r}$, then, $u_i = x'_i - x_i$

The length of PQ is dl , and the length of $P'Q'$ is dl'

Obtain, $(dl)^2 = dx_i dx_i$, $(dl')^2 = dx'_i dx'_i$

$$\left\{ \begin{array}{l} (dl')^2 = d(u_i + x_i)d(u_i + x_i) \\ (dl')^2 = \left(dx_i + \frac{\partial u_i}{\partial x_j} dx_j\right) \left(dx_i + \frac{\partial u_i}{\partial x_k} dx_k\right) \\ (dl')^2 = dx_i dx_i + \frac{\partial u_i}{\partial x_j} \frac{\partial u_i}{\partial x_k} dx_j dx_k + \frac{\partial u_i}{\partial x_j} dx_i dx_j + \frac{\partial u_i}{\partial x_k} dx_k dx_i \\ (dl')^2 = (dl)^2 + \left[\frac{\partial u_i}{\partial x_j} \frac{\partial u_i}{\partial x_k} \delta_{jm} \delta_{kn} + \frac{\partial u_i}{\partial x_j} \delta_{im} \delta_{jn} + \frac{\partial u_i}{\partial x_k} \delta_{km} \delta_{in}\right] dx_m dx_n \\ (dl')^2 = (dl)^2 + \left[\frac{\partial u_i}{\partial x_m} \frac{\partial u_i}{\partial x_n} + \frac{\partial u_m}{\partial x_n} + \frac{\partial u_n}{\partial x_m}\right] dx_m dx_n \end{array} \right.$$

Take the Green-Largrange strain E_{mn} , which is the strain under large deformation

$$E_{mn} = \frac{(dl')^2 - (dl)^2}{2dx_m dx_n} \quad (5.1)$$

Then the strain of large deformation is

$$E_{mn} = \frac{1}{2} \left[\frac{\partial u_i}{\partial x_m} \frac{\partial u_i}{\partial x_n} + \frac{\partial u_m}{\partial x_n} + \frac{\partial u_n}{\partial x_m} \right] \quad (5.2)$$

While, the strain of small deformation is

$$\epsilon_{mn} = \frac{1}{2} \left[\frac{\partial u_m}{\partial x_n} + \frac{\partial u_n}{\partial x_m} \right] \quad (5.3)$$

The small term $\frac{\partial u_i}{\partial x_m} \frac{\partial u_i}{\partial x_n}$ is the difference between theory. In future, this large deformation field could be researched.

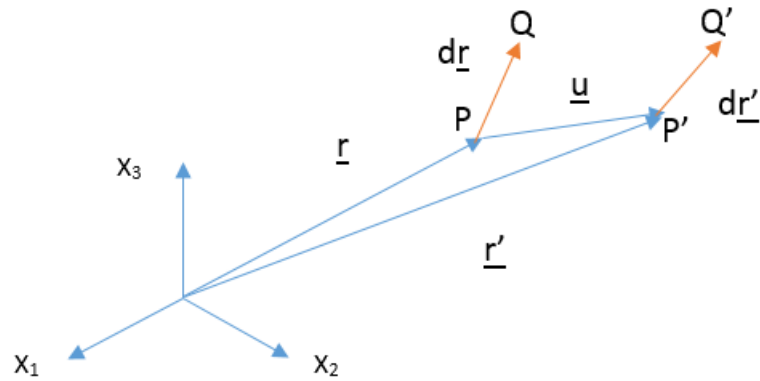


Figure 5.1 Micro element deformation scheme

5.2.2. Orthotropic failure criteria

Tsai-Wu failure criterion can be used for the criterion for orthotropic material.

The Tsai-Wu failure criterion

$$F_i \sigma_i + F_{ij} \sigma_i \sigma_j \leq 1 \quad (5.4)$$

Where $ij = 1 \dots 6$ and repeated indices indicate summation, and F_i, F_{ij} are experimentally determined material strength parameters. The stresses σ_i are expressed in Voigt notation. If the failure surface is to be closed and convex, the interaction terms F_{ij} must satisfy

$$F_{ii} F_{jj} - F_{ij}^2 \geq 0 \quad (5.5)$$

Which implies that all the F_{ii} term must be positive.

For orthotropic materials with three planes of symmetry oriented with the coordinate directions, if we assume that $F_{ij} = F_{ji}$ and that there is no coupling between the normal and shear stress terms (and between the shear terms), the general form of the Tsai–Wu failure criterion reduces to

$$F_1\sigma_1 + F_2\sigma_2 + F_3\sigma_3 + F_4\sigma_4 + F_5\sigma_5 + F_6\sigma_6 + F_{11}\sigma_1^2 + F_{11}\sigma_1^2 + F_{22}\sigma_2^2 + F_{33}\sigma_3^2 \\ + F_{44}\sigma_4^2 + F_{55}\sigma_5^2 + F_{66}\sigma_6^2 + 2F_{12}\sigma_1\sigma_2 + 2F_{13}\sigma_1\sigma_3 + 2F_{22}\sigma_2\sigma_3 \leq 1$$

Let the failure strength in uniaxial tension and compression in the three directions of anisotropy be $\sigma_{1t}, \sigma_{1c}, \sigma_{2t}, \sigma_{1c}, \sigma_{3t}, \sigma_{3c}$. Also, let us assume that the shear strengths in the three planes of symmetry are $\tau_{23}, \tau_{12}, \tau_{31}$. Then the coefficients of the orthotropic Tsai–Wu failure criterion are

$$F_1 = \frac{1}{\sigma_{1t}} - \frac{1}{\sigma_{1c}}, \quad F_2 = \frac{1}{\sigma_{2t}} - \frac{1}{\sigma_{2c}}, \quad F_3 = \frac{1}{\sigma_{3t}} - \frac{1}{\sigma_{3c}}, \quad F_4 = F_5 = F_6 = 0 \\ F_{11} = \frac{1}{\sigma_{1c}\sigma_{1t}}, \quad F_{22} = \frac{1}{\sigma_{2c}\sigma_{2t}}, \quad F_{33} = \frac{1}{\sigma_{3c}\sigma_{3t}}, \\ F_{44} = \frac{1}{\tau_{23}^2}, \quad F_{55} = \frac{1}{\tau_{31}^2}, \quad F_{66} = \frac{1}{\tau_{12}^2}$$

The coefficients F_{12}, F_{13}, F_{23} can be determined using equibiaxial tests. If the failure strengths in equibiaxial tension are

$$\sigma_1 = \sigma_2 = \sigma_{b12}, \quad \sigma_1 = \sigma_3 = \sigma_{b13}, \quad \sigma_2 = \sigma_3 = \sigma_{b23},$$

then

$$\begin{cases} F_{12} = \frac{1}{2\sigma_{b12}^2} [1 - \sigma_{b12}(F_1 + F_2) - \sigma_{b12}^2(F_{11} + F_{22})] \\ F_{13} = \frac{1}{2\sigma_{b13}^2} [1 - \sigma_{b13}(F_1 + F_3) - \sigma_{b13}^2(F_{11} + F_{33})] \\ F_{23} = \frac{1}{2\sigma_{b23}^2} [1 - \sigma_{b23}(F_2 + F_3) - \sigma_{b23}^2(F_{22} + F_{33})] \end{cases} \quad (5.6)$$

The near impossibility of performing these equibiaxial tests has led to there being a severe lack of experimental data on the parameters F_{12}, F_{13}, F_{23} . Using numerical simulation instead of equibiaxial test is a research direction in future.

5.2.3. Selecting the best printing orientation

In order to get the best printing direction, we can analyze performance as this paper mentioned. Then, we test different orientations and find the best one. However, if we can take the Machine Learning (ML) into account, maybe the work on the selecting the best print orientation would be more efficient.

ML is the study of computer algorithms that improve automatically through experience and by the use of data [48]. It is seen as a part of artificial intelligence. Machine learning algorithms build a model based on sample data, known as "training data", in order to make predictions or decisions without being explicitly programmed to do so. Machine learning algorithms are used in a wide variety of applications, such as in medicine, email filtering, and computer vision, where it is difficult or unfeasible to develop conventional algorithms to perform the needed tasks.

In the future, if we can model our work on selecting the best orientation manually as the "training data", the selecting would no longer be complicated and inefficient. Therefore, it is an interesting investigate direction.

Reference

- [1] "3D printing scales up". *The Economist*. 5 September 2013.
- [2] Excell, Jon. "The rise of additive manufacturing". *The Engineer*. 30 October 2013.
- [3] Jane Bird. "Exploring the 3D printing opportunity". *Financial Times*. 30 August 2012.
- [4] Techcrunch.com, "How expiring patents are ushering in the next generation of 3D printing", <https://techcrunch.com/2016/05/15/how-expiring-patents-are-usher-ing-in-the-next-generation-of-3d-printing/?guccounter=1&guce_referrer=aHR0cHM6Ly9lbi53aWtpcGVkaWEub3JnLw&guce_referrer_sig=AQAAABcWGLn75WBLVtW1emnPrLdhHRG5C8dybtT0_rdEZO2D70ZeZ-ipNZ8egL01o3wKgqx Cz1O5UVm3M2XpDFVtp36-9QsQs4tFDhftcj_1xjFqxqAR5rSOOjUyYxdDJWDqN0ROqbTLRuQZpHnuYBWddtp76HJzJYd3IsU6vXFU9I8c>
- [5] all3dp.com, "FDM:Basics", <<https://all3dp.com/1/sla-vs-fdm-resin-vs-filament-3d-printer-the-differences/>>
- [6] N. Guo and M. C. Leu, "Additive manufacturing: Technology, applications and research needs." *Frontiers of Mechanical Engineering*, 8(3): 215–243,2013.
- [7] Tuan D. Ngo, Alireza Kashani, Gabriele Imbalzano, Kate T.Q. Nguyen, David Hui, "Additive manufacturing (3D printing): A review of materials, methods, applications and challenges", *Composite Part: Engineering*, volume 143, Pages 172-196, 15 June 2018.
- [8] Mohsen Attaran, "The rise of 3-D printing: The advantages of additive manufacturing over traditional manufacturing", *Business Horizons*, Vol.6, No.5, Pages 677-688, 2017.
- [9] S. Singh, C. Prakash, and S. Ramakrishna, "3D printing of polyether-ether-ketone for biomedical applications", *European Polymer Journal*, vol. 114, no. February, pp. 234–248, 2019.
- [10] National Aeronautics and Space Administration George C. Marshall Space Flight Center Huntsville, AL 35812. www.nasa.gov/marshall. NP-2016-06-61-MSFC G-156057
- [11] S. Singh, S. Ramakrishna, and R. Singh, "Material issues in additive manufacturing: A review," *Journal of Manufacturing Processes*, vol. 25, no. January 2017, pp. 185–200, 2017.

- [12] C. Koch, L. Van Hulle, and N. Rudolph, "Investigation of mechanical anisotropy of the fused filament fabrication process via customized tool path generation," *Additive Manufacturing*, vol. 16, pp. 138–145, 2017.
- [13] T. Stankovic, J. Mueller, and K. Shea, "The effect of anisotropy on the optimization of additively manufactured lattice structures," *Additive Manufacturing*, vol. 17, pp. 67–76, 2017.
- [14] I. Gibson, D. W. Rosen, and B. Stucker, *Additive Manufacturing Technologies: Rapid Prototyping to Direct Digital Manufacturing*. Springer-Verlag New York, 2010.
- [15] J. P. Kruth, P. Mercelis, J. Van Vaerenbergh, L. Froyen, and M. Rombouts, "Binding mechanisms in selective laser sintering and selective laser melting", *Rapid Prototyping Journal*, vol. 11, no. 1, pp. 26–36, 2005.
- [16] M. Chiumenti, E. Neiva, E. Salsi, M. Cervera, S. Badia, J. Moya, Z. Chen, C. Lee, and C. Davies, "Numerical modelling and experimental validation in Selective Laser Melting", *Additive Manufacturing*, vol. 18, pp. 171–185, 2017.
- [17] H. Kim, Y. Zhao, and L. Zhao, "Process-level modeling and simulation for HP's Multi Jet Fusion 3D printing technology", *2016 1st International Workshop on Cyber-Physical Production Systems, CPPS 2016*, 2016.
- [18] H. J. O'Connor, A. N. Dickson, and D. P. Dowling, "Evaluation of the mechanical performance of polymer parts fabricated using a production scale multi jet fusion printing process," *Additive Manufacturing*, vol. 22, no. June, pp. 381–387, 2018.
- [19] F. N. Habib, P. Iovenitti, S. H. Masood, and M. Nikzad, "Fabrication of polymeric lattice structures for optimum energy absorption using Multi Jet Fusion technology", *Materials and Design*, vol. 155, pp. 86–98, 2018.
- [20] A. W. Gebisa and H. G. Lemu, "Investigating effects of Fused-deposition-modeling (FDM) processing parameters on flexural properties of ULTEM 9085 using designed experiment", *Materials*, vol. 11, no. 4, pp. 1–23, 2018.
- [21] A. Bellini and S. Güçeri, "Mechanical characterization of parts fabricated using fused deposition modeling", *Rapid Prototyping Journal*, vol. 9, no. 4, pp. 252–264, 2003.
- [22] M. Domingo Espín, "Aportaciones al conocimiento sobre la fabricación aditiva con la tecnología Fused Deposition Modeling," IQS School of Engineering, 2016.
- [23] M. N. F. Saniman, M. H. M Hashim, K. A. Mohammad, K. A. Abd Wahid, W. M. Wan Muhamad and N. H. Noor Mohamed "Tensile Characteristics of Low Density Infill Patterns for Mass Reduction of 3D Printed Polylactic Parts", *INTERNATIONAL JOURNAL OF AUTOMOTIVE AND MECHANICAL ENGINEERING (IJAME)*, VOL. 17, ISSUE 2, 7927 – 7934, 2020

-
- [24] Y. Liu and H. Hu, "A review on auxetic structures and polymeric materials," *Scientific Research and Essays - Academic Journals*, vol. 5, no. 10, pp. 1052–1063, 2010.
- [25] R. W. Gray, D. G. Baird, and J. Helge Bøhn, "Effects of processing conditions on short TLCP fiber reinforced FDM parts", *Rapid Prototyping Journal*, vol. 4, no. 1, pp. 14–25, 2002.
- [26] Q. Sun, G. M. Rizvi, C. T. Bellehumeur, and P. Gu, "Effect of processing conditions on the bonding quality of FDM polymer filaments", *Rapid Prototyping Journal*, vol. 14, no. 2, pp. 72–80, 2008.
- [27] A. K. Sood, R. K. Ohdar, and S. S. Mahapatra, "Parametric appraisal of mechanical property of fused deposition modelling processed parts", *Materials and Design*, vol. 31, no. 1, pp. 287–295, 2010.
- [28] A. K. Sood, R. K. Ohdar, and S. S. Mahapatra, "Experimental investigation and empirical modelling of FDM process for compressive strength improvement", *Journal of Advanced Research*, vol. 3, no. 1, pp. 81–90, 2012.
- [29] S. H. Ahn, M. Montero, D. Odell, S. Roundy, and P. K. Wright, "Anisotropic material properties of fused deposition modeling ABS", *Rapid Prototyping Journal*, vol. 8, no. 4, pp. 248–257, 2002.
- [30] G. Cwikła, C. Grabowik, K. Kalinowski, I. Paprocka, and P. Ociepka, "The influence of printing parameters on selected mechanical properties of FDM/FFF 3D-printed parts", *IOP Conference Series: Materials Science and Engineering*, vol. 227, no. 1, 2017.
- [31] L. J. A. A. Gibson and M. F. Ashby, *Cellular Solids: Structure and Properties*, vol. 9. Cambridge University Press, 01 1988.
- [32] R. Hill, "Elastic properties of reinforced solids: some theoretical principles", *Journal of the Mechanics and Physics of Solids*, vol. 11, issue 05, pp. 357–372, 1963.
- [33] P. Suquet, "Local and global aspects in the mathematical theory of plasticity", *Plasticity today*, pp. 279–309, 1985.
- [34] M. G. Geers, V. G. Kouznetsova, and W. A. Brekelmans, "Multi-scale computational homogenization: Trends and challenges", *Journal of Computational and Applied Mathematics*, vol. 234, no. 7, pp. 2175–2182, 2010.
- [35] D. Pasini and S. Arabnejad, "Elastostatics of Lattice Materials" in A. Srikantha Phani and Mahmoud I. Hussein (ed.) *Dynamics of Lattice Materials*, pp. 19 – 51. Wiley, 2017.
- [36] Z. Xia, C. Zhou, Q. Yong, and X. Wang, "On selection of repeated unit cell model and application of unified periodic boundary conditions in micromechanical

analysis of composites”, *International Journal of Solids and Structures*, vol. 43, no. 2, pp. 266–278, 2006.

[37] J. Yan, G. Cheng, S. Liu, and L. Liu, “Comparison of prediction on effective elastic property and shape optimization of truss material with periodic microstructure”, *International Journal of Mechanical Sciences*, vol. 48, no. 4, pp. 400–413, 2006.

[38] matweb.com, “Overview of materials for Polycarbonate/ABS Alloy, Unreinforced”,

<http://www.matweb.com/search/DataSheet.aspx?MatGUID=d16a64a389df424f8e53ed481e77477b&ckck=1>

[39] A. Forés-Garriga, M. A. Pérez, G. Gómez-Gras, G. Reyes-Pozo, “Role of infill parameters on the mechanical performance and weight reduction of PEI Ultem processed by FFF”, *Materials & Design*, 193,108810, 2020

[40] S. Oller, J. Miquel Canet, and F. Zalamea, “Composite material behavior using a homogenization double scale method”, *Journal of Engineering mechanics*, 131(1):65–79, 2005.

[41] F. Otero, X. Martínez, S. Oller, and O. Salomón, “Study and prediction of the mechanical performance of a nanotube-reinforced composite”, *Composite Structures*, 94:2920–2930, 2012.

[42] F. Otero, S. Oller, X. Martinez, and O. Salomón, “Numerical homogenization for composite materials analysis. comparison with other micro mechanical formulations”. *Composite Structures*, 122:405–416, 2015.

[43] Dialami, M. Chiumenti, M. Cervera, R. Rossi, U. Chasco and M. Domingo, “Numerical and experimental analysis of the structural performance of AM components built by fused filament fabrication”, *International journal of mechanics and materials in design*, in press, DOI :10.1007/s10999-020-09524-8.

[44] P. Dadvand, R. Rossi, E. Oñate, “An object-oriented environment for developing finite element codes for multi-disciplinary applications”, *Archives of computational methods in engineering*, 17 (3): 253-297, 201

[45] M. Cervera, C. Agelet de Saracibar, M. Chiumenti, COMET: Coupled Mechanical and Thermal Analysis, Data Input Manual, Version 5. 0, Technical Report IT-308, 2002. <http://www.cimne.upc.es>.

[46] A. Forés-Garriga, M. A. Pérez, G. Gómez-Gras, G. Reyes-Pozo, “Role of infill parameters on the mechanical performance and weight reduction of PEI Ultem processed by FFF”, *Materials and Design* 193 (2020) 108810.

[47] H. Li, T.Wang, J. Sun and Z. Yu, “The effect of process parameters in fused deposition modelling on bonding degree and mechanical properties”, *Rapid Prototyping Journal*, 24 (1): 80-92, 2018.

[48] Mitchell Tom. *Machine Learning*. New York: McGraw Hill. ISBN 0-07-042807-7. OCLC 36417892,1997.

[49] A. Khudiakova, F. Arbeiter, M. Spoerk, M. Wolfahrt, D. Godec, G. Pinter, “Inter-layer bonding characterisation between materials with different degrees of stiffness processed by fused filament fabrication”, *Additive Manufacturing*, 28: 184-193, 2019.

[50] B. A. Aloyaydi , S. Sivasankaran , H. R. Ammar, “Influence of infill density on microstructure and flexural behavior of 3D printed PLA thermoplastic parts processed by fusion deposition modeling” , *AIMS Mater. Sci.* 6: 1033–1048, 2019.